UNDERSTANDING THE ROLE OF ANGULAR MOMENTUM AND SUPERMASSIVE BLACK HOLES IN SHAPING PRESENT-DAY GALAXIES

By

Antonio Jose Porras

Dissertation

Submitted to the Faculty of the

Graduate School of Vanderbilt University

in partial fulfillment of the requirements

for the degree of

DOCTOR OF PHILOSOPHY

in

Astrophysics

May 12, 2023

Nashville, Tennessee

Approved:

Kelly Holley-Bockelmann, Ph.D.

Andreas A. Berlind, Ph.D.

Adam R. H. Stevens, Ph.D.

Amber N. Straughn, Ph.D.

Jessie C. Runnoe, Ph.D.

Jonathan C. Bird, Ph.D.

To my ancestors, those who channel in me the energy to find my purpose. To the strong women in my life: my partner Daniela Wilches Suarez, mother Gladys Valverde Ceciliano, sister Bianchi Suarez Valverde, grandmother Rosa Ceciliano Mena.

ACKNOWLEDGMENTS

It takes a village with caring and supportive community members to raise a Costa Rican Doctor in Astrophysics. First, I am deeply thankful to my advisors Andreas Berlind and Kelly Holley-Bockelmann for the constant support through out my academic journey. They gave me the freedom to design my research project, had the patience when it came to difficult times, and listened. I am thankful to my PhD committee for the constant support, especially Dr. Amber Straughn who never lost sight of me to create NASA opportunities, and Dr. Adam Stevens who patiently guided me throughout the use of the simulations.

I am grateful to the Fisk-Vanderbilt Master's-to-PhD Bridge Program for creating the Universe, where I can be a Master in Physics and a Doctor. Especial thanks to Fisk University for providing the best academic preparation to face my Ph.D., more specifically Dr. Michael Watson, Dr. Akira Ueda, and Constantine Coca. I could not be more proud to be an HBCU alum. I am grateful to Alyce Dobyns, Dr. Dina Stroud, and Dr. Lauren Campbell for the amazing constant support. I am thankful to the Fisk-Vanderbilt Bridge community. In particular, my bridge cohort Dr. Dax Feliz, Dr. Sam Dunham, Dr. Natasha McMann, Dr. Jenna Moore, Dr. KeShawn Ivory, Dr. John Hood, Dr. Karl Jaehnig, Dr. Amber Young, Dr. Victor Calderon.

I am thankful to the National Radio Astronomy Observatory (NRAO) - National Astronomy Consortium (NAC) program for the constant support attending conferences, providing remuneration for my work, and creating opportunities. Within this institution, five outstanding individuals made a big difference in my PhD journey: Lyndele Von Schill, Dr. Aaron Evans, Dr. Betsy Mills, Jessica Harris, and Faye Giles. Their support was never for granted. I got so much support from the NAC community. In particular, I thank Dr. Sinclaire Manning, Dr. Qiana Hunt, Elizabeth Gutierrez, Dr. Alia Wofford, Dr. Moiya McTier, Dr. Peter Doze, and Dr. Tierra Candelaria. Hanging out with them, their phone calls, and everything we did together meant so much during this PhD journey.

I am grateful for the support of Dr. Gloria Fonseca Alvarez and Valeria Urrutia Hurtado, who stood by hearing complains, encouraging me, and being a dream support system. I am happy to be part of the Central American-Caribbean Bridge in Astrophysics, a big part of why I was able to complete my Ph.D. This community is the main reason why doing astronomy matters.

I am honored for the encouragement and support of senior members of the astronomy community, that is: Prof. Jorge Moreno, Prof. Keivan Stassun, Dr. John Forbes, Dr. Nicole Cabrera Salazar, Dr. JoEllen McBridge, and Prof. Jedidah Isler. Their contributions along the way gave me strength.

I thank my friends outside of the astronomy community: Josh Davis, Hieu Nguyen, Kevin Araya Vargas; friends from Costa Rica Renan Villalobos Tenorio, Coqui Vargas, Tomas Segura, Renata Ochoa who were there throughout this whole process every year I visited.

I thank my family of nine uncles and aunts: Tia Analive, Tio William, Tio Martin, my cousins, my siblings Farith and Bianchi for their continuous wisdom and support. I thank Jamie Tabb for his support and guidance since day one when I moved to the U.S. to embark on this journey. I thank Dr. Charlie Tabb for conversations about quantum physics, bosons, neutrinos, as well as differential equations and integrals. His conversations were reminders of how much I enjoyed this. I thank Jamie's family for their constant support.

I thank my mom and dad for always looking at the bright side of things for me. I thank my mother for not leaving me alone, always being there for me with her theories of the Universe, positive energies, and spiritual believes. I thank my grandparents for contributing to shaping who I am. I also thank my partner Daniela Wilches Suarez for giving me this last push towards completing this degree. Her hard work and ambitions motivated me to continue this journey.

This dissertation would not have been possible without this community. This caring village is fruitful. I only ask all of you to continue with me towards the next steps.

TABLE OF CONTENTS

LIST OF TABLES

LIST OF FIGURES

CHAPTER 1

Introduction

I first learned about the Universe in a philosophical context during my last year of high school. Why do we exist? What is beyond our planet Earth? I began reading about the Geocentric model, which placed the Earth at the center of our Universe, while the Sun and the neighboring planets from our Solar System orbited around it. I learned how the model evolved to being a bit closer in accuracy to the observed Universe when the Heliocentric model was proposed, a model that puts the Sun in the center of the Universe, having the Earth and planets in our Solar System orbiting it. During that time, I did not think theories could be refuted or changed. I thought what I read was set in stone, but historically, several theories of galaxy formation, the origin of our Universe, stellar evolution, and other astronomy sub-fields evolved throughout time to become more representative of what the community agrees to how the Universe and its properties actually behave.

As I was introduced into this new field of astronomy in my hometown in Costa Rica, I did not realize that every contribution and perspective that I was learning was from Eurocentric point of view. Moreover, I did not realize that the contribution of women in scientific discoveries were opaque. I heard about Kepler for the planetary motion equations, not Maria Cunitz, Maria Margaretha Kirch, or Caroline Herschel (Bernardi, 2016). Because community agreement is essential in refuting or approving scientific discoveries, a pool of diverse mindsets is necessary to tackle scientific problems from different perspectives.

1.1 Outline

My PhD thesis broadly focuses on galaxy formation and evolution. In this Chapter, I present a succinct summary of our current understanding of the creation of the Universe and how galaxies work. It is intentionally written to provide a global and simplified view of how galaxies work to the general public. Because this is a broad sub-field of astronomy to cover, this chapter provides an incomplete view, but attempts to put the work in a larger context. In Chapter 2, I cover the technique I employ, semi-analytic modeling, to conduct my work.

Chapters 3 and 4 discuss the bulk of my scientific work, which centers on what drives galaxy structure. Although angular momentum is a fundamental quantity that describes the orbits of planets, gaseous disks and galaxies, it is not completely clear how critical a role it plays in shaping present-day galaxies. Chapter 3 is a reprint of my first-author paper in the Astrophysical Journal showing that angular momentum is less important than dark matter halo mass in determining the shape of the galaxy. More recently, I am exploring the role that black hole physics plays in setting the stellar mass of a galaxy; Chapter 4 describes the near-final

state of that unpublished work.

As a scientist, I am driven by curiosity, questioning theories, and exploring new physics behind galaxy formation. My identity as a scientist also pushes me to create tools to increase participation of underrepresented astronomers and their contributions to the global scientific community. In Chapter 5, I provide a summary of my contributions towards making astronomy more accessible to specifically Central American and Caribbean undergraduate students. Chapter 6 is a summary and a look forward.

1.2 The start of our Universe

Between the 1940s until the 1960s, the two leading theories of how the Universe began were the Steady State Theory (Bondi & Gold, 1948) and the Big Bang Theory (Peebles et al., 1991). While the Steady State Theory described an expanding Universe with no beginning nor end and matter constantly created through the formation of stars and galaxies, the Big Bang theory proposed that the Universe was born from a singularity, a super dense and hot point that exploded between 14-12.7 billion years ago. Estimates of the age of the Universe have recently sparked major debates due to the uncertainty in the measurement of the Hubble constant, which range between $H_0 = 67.9 \pm 1.5$ to 75.1 ± 2.3 km s^{-1}Mpc^{-1} (Choi et al., 2020; Schombert et al., 2020). Nonetheless, the Big Bang theory became generally accepted due to the detection of the Cosmic Microwave Background (CMB) (Penzias & Wilson, 1965), radiation that is found in every direction and is ascribed to the imprint of this long-ago explosion. The CMB is a near perfect Planck spectrum at 2.72 Kelvin, implying that it was generated by a dense, opaque source in thermal equilibrium. CMB radiation provides detailed information about the matter density as well as its distribution through minute fluctuations in the temperature across the sky. It is important to note that most of the matter in the Universe is in a yet-to-be-directly-detected form called *dark matter*, and its presence can be inferred by the distribution of the CMB temperature fluctuations on a map of the sky; this distribution can by measured by an *angular power spectrum* technique.

Right after the Big Bang, the Universe began expanding. With the expansion, the hot and dense photon-baryon plasma began cooling. About 300,000 years later, electrons began to combine with protons to form neutral hydrogen among other elements. As the expansion continued, dark matter particles form into a filamentary scaffold as a result of gravity pulling them together. Baryons, as a minor character in the mass budget of the Universe, simply fall into the denser parts of this scaffold, and where filaments intersect, a spheroidal and clumpy *dark matter halo* forms – we discuss dark matter halos more in the next section. Gas collapses within the deep gravitational potential from these dark matter halos, forming first population of stars, also known as Population III stars. Although the details of Pop III star formation is still under debate, they are thought to form $\sim$ 200 Myr after the Big Bang from H_2-cooled metal-free gas (Klapp, 1983; El Eid

et al., 1983). As these stars evolved, they fused hydrogen into heavier elements. When these stars reached the end of their lifetime, they underwent supernova (SNe) explosions, enriching the local gas with these heavier elements processed in the Pop III interior. As this process takes place, protogalactic clouds give birth to the first galaxies in the Universe. Fast-forward in time, the large-scale structure of the Universe continues to condense, resulting in densely populated regions where galaxies are highly interactive with one another throughout their lifetime. As matter clumps, it leaves behind voids of empty space, where few galaxies live. Figure 1.1 shows an illustration of how the Universe evolved from the Big Bang to the present day.

1.3 A brief history of dark matter halos

Dark matter makes up most of the matter in the Universe. There is a wealth of evidence regarding the existence of dark matter from observations of the Bullet cluster or Abell 2029, which shows two clusters merging in which the dark matter halos pass by one another, as evidenced by gravitational lensing, while the gas from each cluster collides, shock heats, and shines in the Xray (Clowe et al., 2006) as well as from simulations (Moore, 1994; Navarro et al., 1996; Binney & Tremaine, 2008; Bullock & Boylan-Kolchin, 2017). An indirect detection of dark matter can be found though patterns of anisotropies in the CMB (Maity & Saha, 2018). A more relevant case, the existence of dark matter is strongly linked to the rotational curves of galaxies. When looking at a typical spiral galaxy edge-on, we see that as we move farther away from the center of the galaxy, where the galaxy runs out of light, the rotation speed should decrease as $r^{-1/2}$. Surprisingly, observations have shown that the velocity does not drop. Figure 1.2 shows the rotational velocity as a function of radius for a galaxy like the Milky Way. Because most galaxies have baryonic matter concentrated at their center, they show an exponential increase in velocity up to some radius, where the velocity becomes constant or slowly rises. Since there is so little baryonic matter in the outer parts of the galaxy, we believe that dark matter is what drives the constant velocities (Rubin & Ford, 1970; Rubin et al., 1978). Thus, the difference between the expected light coming from the stellar disk and what is observed is the amount of dark matter contributing to the overall galaxy mass.

Inside a dark matter halo, we can also find subhalos; we think the main, or "central" galaxy is hosted by the main dark matter halo, while the subhalos host satellite galaxies. Together, the halos and subhalos are characterized by a *halo mass function*, which describes the number density of halos as a function of their mass. The halo mass function has a characteristic power-law slope at low halo mass, meaning that low-mass halos are increasingly more common, and an exponential cut-off at high halo mass, which is related to the maximum halo mass that could have collapsed in the age of the Universe. From the halo mass function, we know that there is is roughly one Milky Way mass halo for every 100 Mpc^3. The halo mass function can be obtained numerically using N-body simulations (described in Chapter 2) or derived using extended Press-

Figure 1.1: Illustration of our view of the observable Universe from Earth's perspective. The image shows layers of an epoch in the Universe from top to bottom. The first layer shows the Big Bang, followed by the CMB, and then the farthest visible objects detected such as the J0313-1896 (the most distant known quasar), GRB 090429B (most distant known gamma ray burst), HD1 (most distant galaxy), and Tonantzintia 618 (most massive black hole). The following layer shows the cosmic web, where galaxies clump with one another to form filaments. There, we observe massive clusters of galaxies, and some empty places named voids. The next layer shows the local group of galaxies followed by a picture of our own Milky Way galaxy. Within the spiral arm, we see many nebulae and nearby stars. The second-to-last layer shows the Oort cloud which is the belt of objects at the edge of our Solar System. Lastly, we see our Solar System with our Sun. Everything is viewed from our planet Earth's perspective. Image credit: Pablo Carlos Budassi (2023).

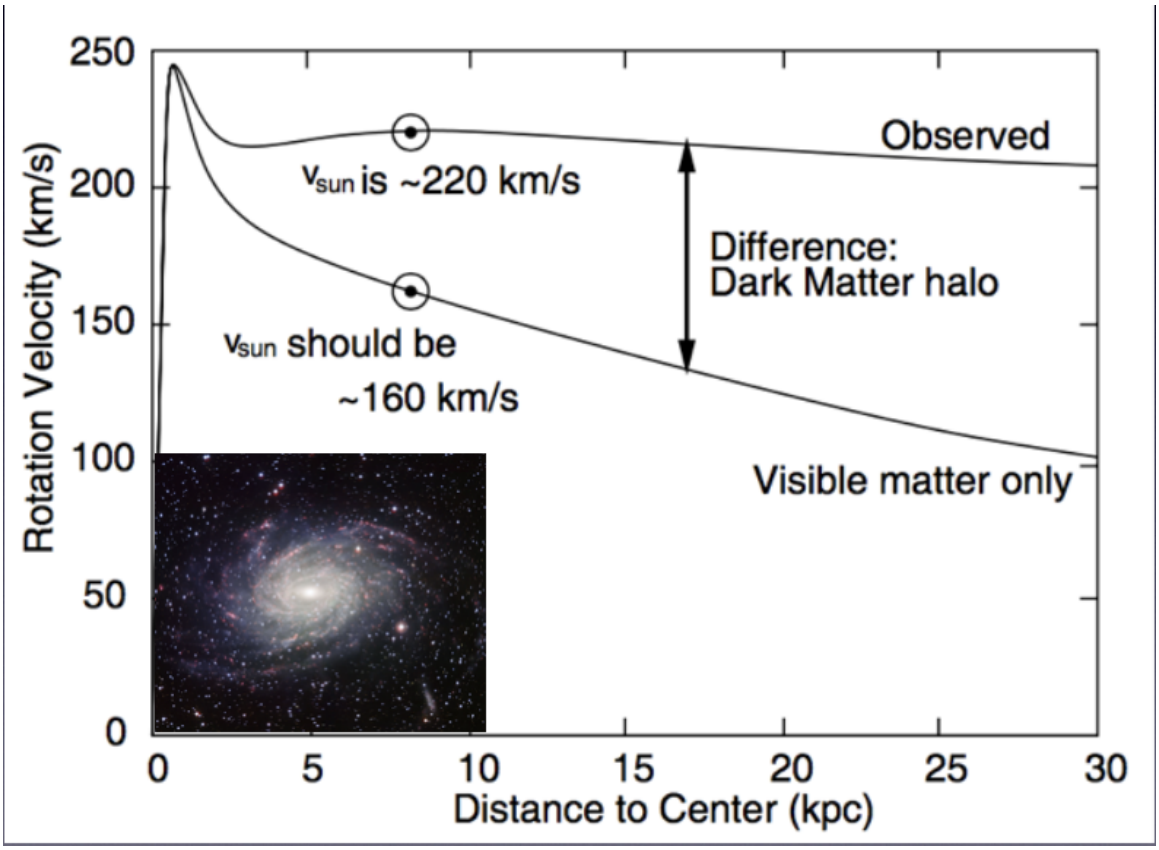

Figure 1.2: Rotation curve as a function of radius for a typical spiral galaxy like our Milky Way. The upper line shows the observed velocity, where the Sun's moves 220 km s^{-1} at 8 kpc from the center of the galaxy. The lower line is the modelled velocity curve when only accounting for the light coming from the galaxy, where the Sun's velocity would be about 160 km s^{-1}. The difference between the observed line and the model line encodes the amount of dark matter contained in the galaxy. Image credit: Peter Schneider (2006).

Schechter theory, which deals with the collapse of density perturbations under gravity and galaxy mergers. The halo mass function provides a quantitative measure of the abundance and clustering of dark matter halos, which can be compared with observations of the large-scale distribution of galaxies. In fact, being able to reproduce the halo mass function is often used as a basic check on the validity of a simulation, semi-analytic model, or dark matter theory. In this upcoming section, we will explore the relationship between dark matter halos and their host galaxies.

1.4 A brief history of galaxy formation and evolution

Only 5 percent of matter in the Universe is visible matter. Most of this matter sits within individual galaxies and galaxy clusters. Galaxies have bound stars, cold gas, hot gas, and dust within a gravitational potential governed by a disk, stellar halo, and a bulge, bar or a combination of both. Galaxies also have a dark matter halo that is not necessarily symmetric. In many cases, galaxies also include a central massive black hole. When thinking about galaxy properties, interactions, and evolution, I like comparing them with humans. Each one of us has an ancestral tree that contributes to our DNA. Likewise, present-day galaxies have characteristics derived from their past. Like a family ancestral tree, present-day galaxies and their dark matter halos are built from previous galaxy mergers and interactions, a common term known as hierarchical structure formation, where halo and galaxy structures merge and grow to form larger ones.

Many galaxy clusters are in high-density regions. When people grow up in places like New York City, their interactions with other people shape their present-day character. Similarly, galaxies that live in clustered regions tend to interact with many other galaxies to the point that their internal characteristics start to change (i.e. their star formation rates, angular momentum transfer, bulge–disk composition, black hole accretion, metallicity). Nonetheless, not everyone who lives in New York City grew up there. There are cases where galaxies that built most of their mass in a low-density region may end up gravitationally bound in a high-density region.

Galaxies come in many shapes, colors, and sizes. The most massive galaxies tend to have smaller satellites orbiting them. Many satellite galaxies have similar properties to that of their host/central galaxy (Stoehr et al., 2002; Zucker et al., 2004). Because of their bound orbit inside the central galaxy's halo, tidal forces can unbind stars and gas from the satellite (Stoehr et al., 2002; Read et al., 2006), and can excite bursts of star formation in the massive galaxy. As the most massive galaxy undergoes several minor and major mergers throughout its lifetime, its morphology, stellar mass, halo mass, metallicity, color, size, and other properties also change. For satellites that orbit relatively close to their host, their gas content may be removed by both

tidal and ram pressure stripping[1] (Abadi et al., 1999; Vollmer et al., 2001; Stevens & Brown, 2017).

Because galaxies are so far away, the main way we can study them is through their light emission. An important challenge in astronomy is the difficulty in observing galaxies close to the start of the Universe. Aside from appearing dim due to their immense distance from us, their peak brightness shifts to a longer waveband. When the first stars are formed, they emit the most light in the ultraviolet (Savage & Sembach, 1996). However, because the Universe is expanding, these photons are stretched as they travel through space, so we observe the light from a pop III star or a protogalaxy in the infrared. Therefore, infrared telescopes, such at JWST, are essential to observe first born stars and galaxies.

Interestingly, we will never observe the instantaneous light from a galaxy. In other words, when we receive light from a galaxy, we are seeing the galaxy as it was when the light left the galaxy. Because light takes time to travel through space, the farther the galaxy is, the longer will take the light to reach us, and the older the galaxy will be once that light reaches us. Observing galaxies in different wavelengths provides new information about physical properties happening inside galaxies. For example, we can study the motion of cold gas in the intergalactic medium and the synchrotron emission[2] from active galactic nuclei[3] (Padovani, 2017), or AGN, through the use of radio telescopes like the Atacama Large Millimeter Array (Bonato et al., 2019), the Very Large Array (Orienti et al., 2020), and the Very Large Baseline Interferometer (Kharb et al., 2014). Using infrared telescopes like JWST, Spitzer, and Herschel, we can study cold and warm dust, warm gas, and molecules in the stars' atmospheres (Pascucci et al., 2009; Yıldız, 2013). The Hubble Space Telescope, which observes at the optical and ultraviolet wavelengths, allows us to view much of the stellar content of a galaxy (Grogin et al., 2011). The color of stars is attributed to how hot they are, and therefore, their lifespan; likewise, the color of galaxies has a strong relationship star formation rates (Salim et al., 2007; Blanton & Moustakas, 2009; Schawinski et al., 2014). Red galaxies tend to be passive galaxies with low star formation rates and old stars remaining, whereas blue galaxies are active, with high star formation rates and very young stars. In the ultraviolet, we may calculate the star formation rates (Salim et al., 2007), and can find the chemical composition and densities of the interstellar medium (Martin et al., 2005). In the X-ray regime, we can detect gas that is super heated to millions of degrees using telescopes like the Chandra X-ray Observatory (Bond, 2001). Lastly, gamma rays are emitted by higher energy processes in galaxies such as powerful magnetic fields in supernovae, colliding neutron stars, pulsars, blazars, and supermassive black holes (Kimura et al., 2021).

[1] Ram pressure stripping occurs when pressure from relative motion through the ambient circumgalactic medium, strips gas out of the gravitationally bound state (Abadi et al., 1999).

[2] The emission of electrons traveling relativistically in a magnetic field

[3] A large amount of light produced by super energetic matter being ejected by a supermassive black hole

1.4.1 Measuring mass from light

Stellar mass is one of the most important properties of galaxies. The fundamental approach to approximate the stellar mass is to measure the light observed from each galaxy and attribute that light to stars. To convert light to mass, astronomers try to fit an observed spectral energy distribution (SED)[4] (Conroy, 2013) to one created by a stellar population synthesis model from an ensemble of stars (Lower et al., 2020) over a wide range of masses, ages, and metallicities. One challenge is that starlight can be obscured by dust before emerging from the galaxy and reaching us. Dust absorbs light and re-emits it in the infrared wavelength, making the light dimmer and redder, which would result in an older stellar population model fit than in reality. Unfortunately, a stellar population that is metal-rich can also appear red, so at first blush, it seems difficult to determine if a galaxy is red because it is dust-obscured, old, or metal-rich.

Observing particular spectral lines can help break degeneracies between age, dust attenuation, and metallicity, but this may require a long time-exposure to collect enough light.

In practice, it is too difficult to measure the stellar properties of each galaxy in the Universe individually. For this reason, we rely on models that we hope describe the majority of the galaxies we observe. As an example, the same shape of the initial mass function (IMF)[5], dust attenuation, mathematical forms to obtain star formation histories, and/or stellar metallicity distribution are used for samples of millions of galaxies (Bruzual & Charlot, 2003; Maraston, 2005; Conroy & Gunn, 2010; Robotham et al., 2020).

Generally, a universal IMF is used for all galaxies across time regardless of their type. It provides a good approximation to the global star formation history (Lilly et al., 1996). Even though the IMF does not vary when derived from different local stellar populations within the Milky Way (Bastian et al., 2010), Conroy & van Dokkum (2012) suggest that the slope of the low-mass IMF may be correlated with the global galactic potential, becoming shallow with decreasing galaxy velocity dispersion. It is important to note that although low-mass stars contribute most to the mass of galaxies, they contribute little to the overall light, so the effect of a changing IMF on the low-mass end would have little effect on the star formation rate as derived from photometry. Changing the high-mass region of the IMF, by contrast, does have a significant effect on the luminosity, given that the most massive stars contribute the most (per unit mass) to the overall luminosity budget.

The Salpeter IMF (Salpeter, 1955) is often assumed, which counts stars between $0.1 - 100\,\mathrm{M}_{\odot}$. However, some models show a turn over at masses below $1\,\mathrm{M}_{\odot}$, which result in a smaller mass-to-light ratio than predicted by Salpeter, so a broken power-law by Kroupa (2001) and a log-normal turnover by Chabrier (2003) were introduced. Once stellar masses are calculated for a population of galaxies, one can measure the

[4] An SED shows the energy emitted by an object at different wavelengths

[5] A function describing the initial distribution of masses for a population of stars

abundances of galaxies as a function of mass. In general, as the stellar mass has been derived, simultaneously, the star formation rates are measured.

1.4.2 Star formation rate measurements

Star formation rate (SFR) measurements are sensitive to the wavelength in which stars and gas are observed. For example, the H-α emission from H_{II} regions comes from photoionization triggered by O-type stars, which are the bluest, hottest stars with lifetimes shorter than 20 Myr, while the optical emission comes from stars with a broader mass range and longer lifetimes (Schmidt, 1959; Searle et al., 1973; Kennicutt, 1998). Thus, the time dependence on star lifetimes may complicate star formation measurements from individual galaxies, especially if their SFR changes abruptly over short timescales.

Additionally, the UV light emitted by stars is absorbed by dust and re-radiated at the mid- to far- infrared wavelengths, so the total IR luminosity is the sum of the energy absorbed by dust. Neglecting AGN emission, most UV radiation comes from star formation, while the IR luminosity is approximately proportional to the absorbed fraction of the energy from star formation. One tricky aspect of measuring star formation rates, however, is to disentangle the contributions from AGN to the UV and IR emission (Kim et al., 2022). Because AGNs contribute to the heating of gas and dust, the re-emitted light from dust may not necessarily come from stars. Assuming that the entire IR luminosity comes from star formation, the star formation rate is measured as:

$$\mathrm{SFR_{IR}} = \kappa_{\mathrm{IR}} \times \mathrm{L_{IR}}, \tag{1.1}$$

where $\kappa_{\mathrm{IR}} = 1.73 \times 10^{-10}\,\mathrm{M_\odot\ yr^{-1}\ L_\odot^{-1}}$ is a calibration factor (Kennicutt, 1998) and $\mathrm{L_{IR}}$ is the total IR luminosity emission integrated over 8 to 1000 μm. To account for the contribution of the UV luminosity, the total star formation rate becomes:

$$\mathrm{SFR_{total}} = \kappa_{\mathrm{FUV}} \times \mathrm{L_{FUV}} + \kappa_{\mathrm{IR}} \times \mathrm{L_{IR}}, \tag{1.2}$$

where $\kappa_{\mathrm{FUV}} = 2.5 \times 10^{-10}\,\mathrm{M_\odot\ yr^{-1}\ L_\odot^{-1}}$ using Conroy et al. (2009). The $\mathrm{L_{FUV}}$ is the total far-UV luminosity at 1500 Å with no correction for extinction.

Dust extinction is mostly relevant around mid-infrared and UV wavelengths where the distinction between star formation and AGN emission is difficult to make (Calzetti, 2001). Observational results from Lyman break galaxies at redshift 2 detected by Herschel found that, in general, 80 percent of the FUV emission is absorbed by dust (Reddy et al., 2012). Many galaxies have a ratio of $\mathrm{L_{IR}/L_{FUV}} > 100$ (Penner et al., 2012), some of which are dust-obscured galaxies (Dey et al., 2008) that are not visible at optical wavelengths.

These galaxies typically contribute between 5 to 10 percent of the star formation rate density at $z = 2$ (Pope et al., 2008). There is also work on measuring the SFRs of quiescent galaxies by taking the 4000 Å break (Kauffmann et al., 2003). Note that, generally, observations of SFRs probe various time-scales, so, in some cases, the measured SFR is not the actual instantaneous quantity, but the average over some time-scale.

1.4.3 The Angular Momentum of Galaxies

Galaxy angular momentum provides clues into their formation and evolution. We know that there exists angular momentum transfer through tidal torques from perturbations of galactic clouds (Hoyle, 1949; Peebles, 1969), which implies that galaxies can gain angular momentum through early interactions. It is assumed from this galaxy formation framework that angular momentum is conserved as material collapses to form a centrifugally-supported disk (Mo et al., 1998; Bullock et al., 2001; Fall & Romanowsky, 2013). The angular momentum of the gas, stars, and dark matter mass determines the morphology of the galaxy, a relation that has been observed and simulated (Fall, 1983; Romanowsky & Fall, 2012; Obreschkow & Glazebrook, 2014; Rodriguez-Gomez et al., 2017; Lagos et al., 2017; Sweet et al., 2018; Porras-Valverde et al., 2021).

Many semi-analytic models (SAMs, defined in Chapter 2) tie the angular momentum of the disk to that of the halo (Fall & Efstathiou, 1980; Fu et al., 2010). It was first believed that the baryonic angular momentum was similar to the angular momentum of the dark matter. However, galaxies at low redshift have experienced mergers and feedback episodes through AGN and supernova explosions, so the existing correlation in direction and magnitude between the baryonic and dark matter angular momentum may be strongly affected (Davis, 2011). In simulations, we can calculate the spin of the dark matter halo, which has a dependence based on the environment in which the halo sits (Barnes & Efstathiou, 1987). Looking at the dark matter halo spin distribution of galaxies with a particular morphology gives us a clear understanding of their evolution (Parry et al., 2009; Sales et al., 2012; Zavala et al., 2016; Rodriguez-Gomez et al., 2017). We know that contrary to ellipticals, spiral galaxies have collapsed and revolving structures that maintain angular momentum while minimizing gravitational potential energy (Figure 1.3). Since dark matter particles trace the motion of baryonic matter in galaxies, using cosmological simulations, we can conclude that the dark matter spin distribution has some information about the galaxy morphology (Rodriguez-Gomez et al., 2017).

To measure the global angular momentum of a galaxy or dark matter halo in a simulation (description of simulations will be present in Chapter 2), we need the sum of the angular momentum of each particle inside the stellar disk or the dark matter halo, J.

$$J = m_i \sum_{i=1}^{N} r_i \times v_i \tag{1.3}$$

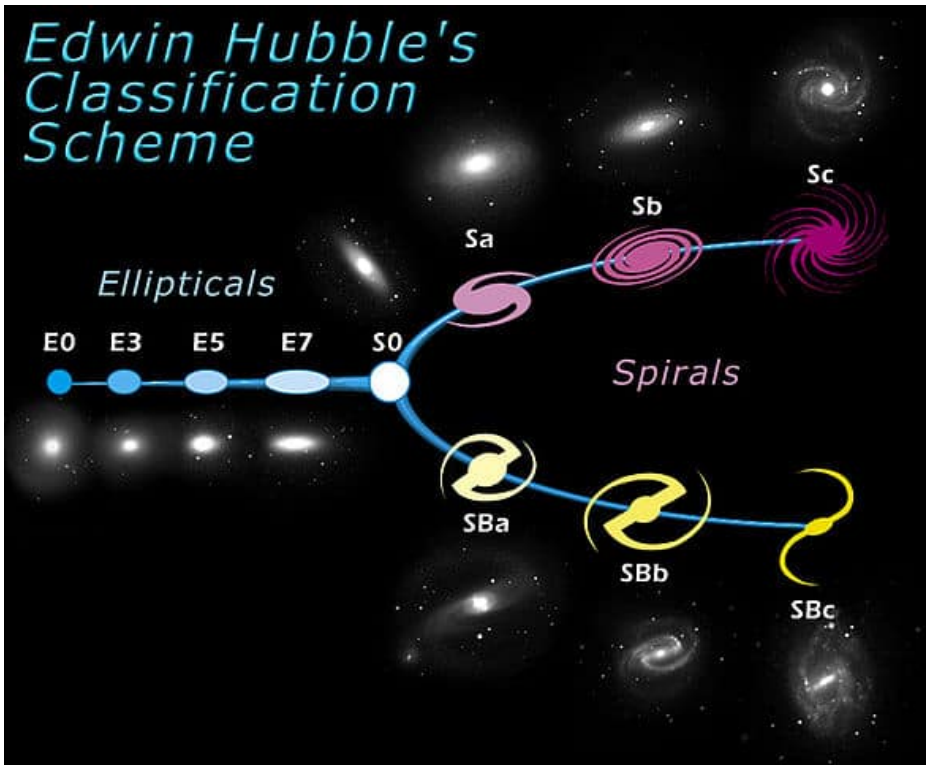

Figure 1.3: Illustration of different galaxy morphologies. Elliptical galaxies (left hand side of the image) are formed from mergers, or from secular star formation of a spiral galaxy once it runs out of cold gas. Irregulars (not shown here) and pseudobulges can form through Toomre (1963) instabilities. Spiral galaxies (right hand side of the image) form also through minor mergers of gas-rich galaxies. Image credit: Nineplanets.org (2023).

where m_i, r_i, and v_i is the mass, position and velocity of the ith particle. We obtain the specific angular momentum, j by dividing the total mass of the system, M.

$$j = \frac{J}{M} \tag{1.4}$$

Several studies show the observed correlation between the angular momentum of galaxies and their morphology at $z = 0$ (Fall, 1983; Fall & Romanowsky, 2013; Porras-Valverde et al., 2021). At fixed stellar mass, the stellar specific angular momentum ($j_{\rm stellar}$) increases with decreasing bulge-to-total stellar mass ratio (B/T) (Fall & Romanowsky, 2018; Posti et al., 2018; Sweet et al., 2018). This angular momentum–stellar mass relation has been studied across several numerical simulations (Genel et al., 2015; Teklu et al., 2015; Zavala et al., 2016; Rodriguez-Gomez et al., 2017; Sokołowska et al., 2017; El-Badry et al., 2018; Obreja et al., 2019). In chapter 3, Porras-Valverde et al. (2021) describes a comparison between observations and simulations of the angular momentum, stellar mass, and morphology relation.

1.4.4 Galaxy–halo connection

The galaxy–halo connection refers to the link between galaxy properties and their dark matter halos. When Peebles (1980) analyzed the two-point correlation function in galaxies to measure clustering statistics, it was discovered that massive galaxies have differing clustering properties than average galaxies (Bahcall & Soneira, 1983; Klypin & Kopylov, 1983). This is important given the correlation between halo clustering and halo mass (Mo & White, 1996). However, initially, cosmological simulations were not able to resolve subhalos within clusters (Moore et al., 1998). This is important because in the simulations these subhalos merged with the central halo more quickly than they should, resulting in a predicted number of subhalos that is significantly lower than expected (Moore et al., 1996a; Klypin et al., 1999). This was known as the "overmerging problem." This overmerging problem is thought to be caused by numerical limitations in the simulations, such as the limited spatial and mass resolution, that caused subhalos to lose more mass and angular momentum than they would if they could properly resolve the physics of tidal stripping and dynamical friction. It was not until the 1990s that Klypin et al. (1999); Colín et al. (1999) resolved subhalos, while approximating a power-law that describes the two-point halo correlation function. Soon after, the observations of hundreds of thousands of galaxies with the Sloan Digital Sky Survey (SDSS) (York et al., 2000) allowed theorists to compare simulated halo clustering properties with observed galaxy clustering as a function of properties like luminosity, color, star formation rates, and stellar masses. At the same time, the establishment of the standard model of cosmology, ΛCDM, became the backbone for our understanding of galaxy formation (Cen & Ostriker, 1994, 1999a,b)

A fundamental relationship studied in ΛCDM and observationally is the correlation between the stellar mass and the halo mass of galaxies. Empirically, one can match the observed stellar mass of galaxies with simulated dark matter halos using a variety of techniques that differ in complexity such as abundance matching (Colín et al., 1999), the halo occupation distribution (Kravtsov et al., 2004), conditional luminosity function (Yang et al., 2003), and models that connect galaxies over time to their histories (Behroozi et al., 2019). Semi-analytic models (e.g. Croton et al., 2006; Croton et al., 2016; Somerville et al., 2001; Somerville & Davé, 2015; Stevens et al., 2016) and hydrodynamical simulations (e.g. Khandai et al., 2015; McAlpine et al., 2016; Naiman et al., 2018) evolve galaxies within their host dark matter halos as a function of time, providing a more physical approach to the galaxy–halo connection.

Wechsler & Tinker (2018) compared the ratio of stellar mass to halo mass as a function of halo mass for different empirical models (see figure 1.4). These data only included central galaxies at $z = 0$. Although, in general, the simulated data are in good agreement with observations, the differences between empirical models arises from different stellar mass functions, luminosity functions, and/or halo mass functions. One important feature in this relation is the peak around $M_h = 10^{12}\,\mathrm{M}_\odot$, which corresponds to less than 10 percent of the matter in galaxies being composed of stars. This means that if these halos have a baryon fraction of about 17 percent, only about 20-30 percent of the baryons have turned into stars. Above or below this peak, star formation efficiency drops. This drop in star formation efficiency comes from feedback mechanisms that affect star formation and black hole growth, which affect galaxies differently based on their mass. For massive galaxies ($M_h \sim 10^{12-15}\,\mathrm{M}_\odot$), AGN suppresses star formation through ejection of cold gas from the disk and heating up the hot gas surrounding the galaxy (Croton et al., 2016). For low-mass galaxies ($M_h \sim 10^{9-11}\,\mathrm{M}_\odot$), stellar feedback is more efficient at driving cold gas out of the galaxy (Hopkins et al., 2012). For even smaller size galaxies ($M_h < 10^{9}\,\mathrm{M}_\odot$), the gravitational potential is too shallow to combat photoionization feedback (Bullock et al., 2000). In the next section, I will focus on the role of feedback in quenching massive galaxies.

1.4.5 Galaxy quenching and Feedback

Galaxy–galaxy interactions can enhance star formation and/or suppress it through feedback (Moore et al., 1996b), a term meaning that energy is injected back into a galaxy from either AGN or star formation.

In many cases, galaxy mergers trigger rapid star formation processes known as starbursts, where the aftermath leaves a lack of cold gas and therefore a quenched galaxy. At redshifts close to 1, post-starburst and quiescent galaxies are predominantly massive, indicating that their associated AGN feedback may contribute to their rapid star formation quenching (Wild et al., 2016). Soon after the peak of the cosmic star formation era ($z = 2$), the number of quiescent galaxies increased, while the number of star-forming galaxies remained constant (Bell et al., 2004) (see figure 1.5). As the gas fractions in galaxies decrease, disks become more

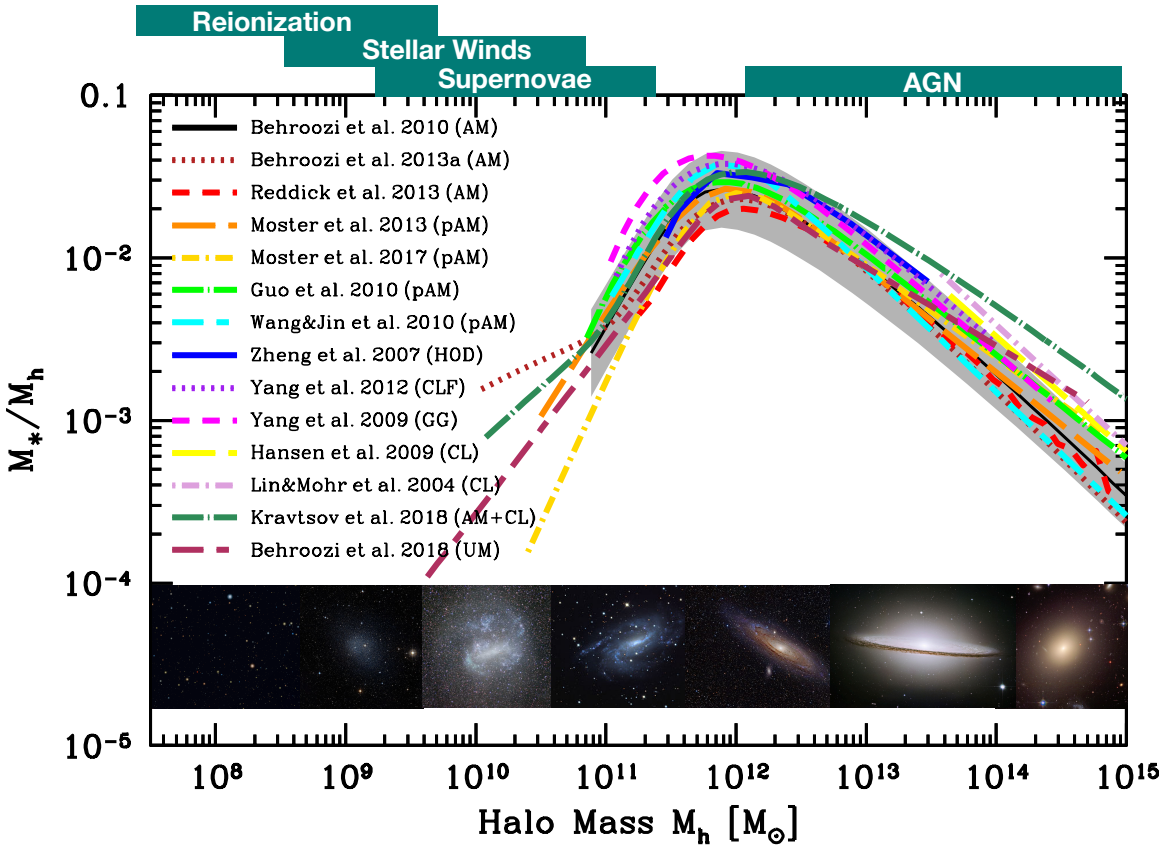

Figure 1.4: The ratio of the stellar mass to halo mass as a function of halo mass for central galaxies at $z = 0$ using different empirical methods that match observed stellar masses with simulated dark matter halos. Note that these studies use different definitions of halo mass, which may play an effect when comparing them within the same set of axes. The top of the figure shows the physical processes that affect galaxies at varying halo mass ranges. The bottom part shows different types of galaxies living within each halo mass range. Image credit: Figure 2 from Wechsler & Tinker (2018).

stable over time and cold gas streams begin to shut down. The constant number of star-forming galaxies in addition to the global decrease in star formation density by a factor of about 10 since $z = 2$ (Madau & Dickinson, 2014) shows that the star formation rates in active galaxies are also declining over time-scales of several Gyr. Yet, it is still unclear how this decline in star formation rates for star-forming galaxies relate to the formation of quiescent galaxies. Because quiescent galaxies are unable to form stars *in situ*, the number density of quiescent galaxies might come from active galaxies shutting down their star formation, and consequently, migrating into the quiescent population (Faber et al., 2007).

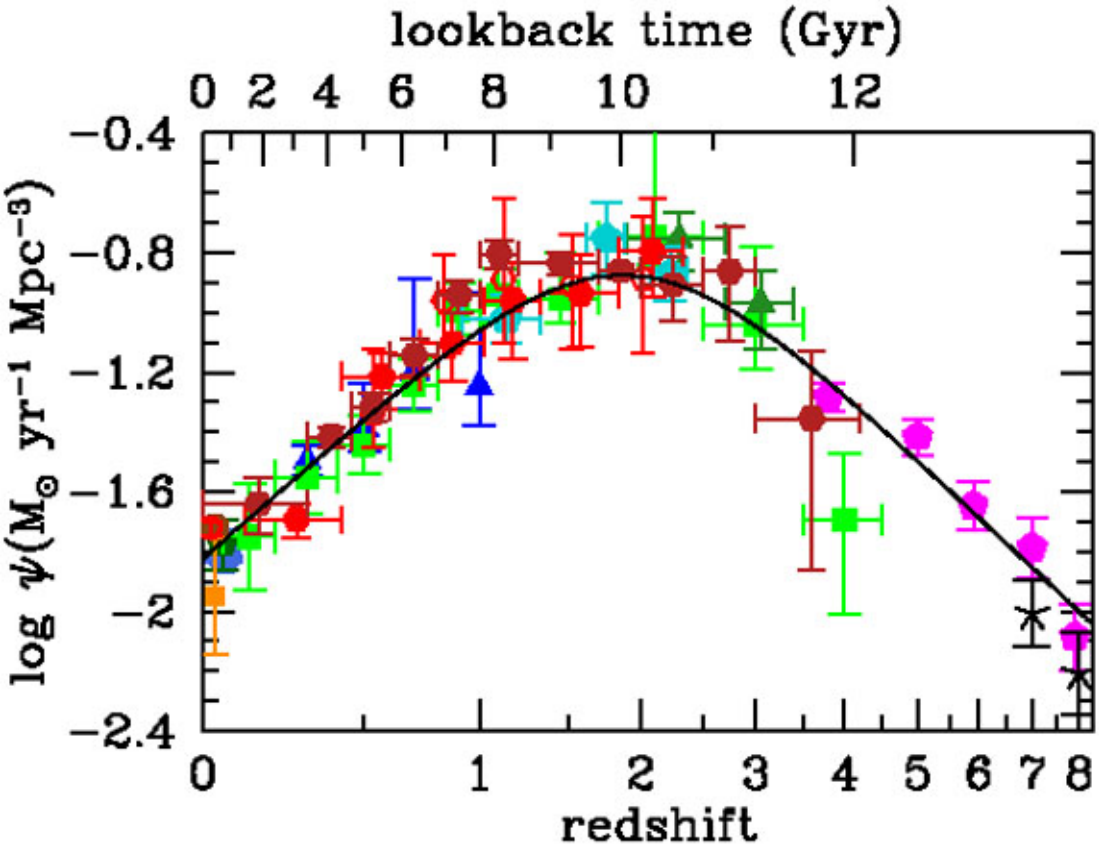

Figure 1.5: The history of cosmic star formation using far-UV and IR rest-frame measurements. Image credit: Figure 9 from Madau & Dickinson (2014).

Several simulations have shown that at least part of the underlying physics behind this evolution comes

from disk instabilities and mergers, which contribute to the formation of quiescent galaxies through rapid gas inflow towards the center of the galaxies (Hopkins et al., 2009a; Dekel & Burkert, 2014). In simulations, efficient outflows are also required to eject the remainder of the gas that is not consumed by star formation via supernovae and/or AGN feedback. Regardless of the mechanism that quenches galaxies, forming quiescent galaxies at high redshift in gas-rich environments remains a challenge for models.

In semi-analytic models, one of the modes of AGN feedback implemented is *radio mode* feedback. *Radio mode* feedback is a mechanism where radio-emitting plasma, typically originating from AGN, heats up and pushes back the surrounding gas. This energy injection regulates the growth of the central black hole and star formation in the host galaxy. This concept of *radio mode* feedback originated from Fabian et al. (2003), where they proposed that the radio jets emanating from AGN can deposit significant amounts of energy into the surrounding intracluster gas, potentially regulating its cooling and preventing the formation of cool cores in galaxy clusters. They argued that it could explain the observed lack of cool cores in some clusters.

SAMs have long incorporated the effects of *radio mode* feedback as an important mechanism for regulating the growth of black holes and the star formation in host galaxies. For example, Croton et al. (2006) and Bower et al. (2006) introduced a model that included the effects of *radio mode* feedback, and found that it could reproduce the observed galaxy luminosity functions and mass-to-light ratios. As a result, this AGN feedback mode starves the central galaxy from cold gas, leading it to quench. Although these models do a great job at ceasing star formation, there are many complications regarding the amount of energy used to heat gas and the timescales at which this heated gas can cool down to form stars. Over the past few decades, improved versions of these models have been developed that incorporate more detailed physical processes and observational constraints. More recently, Henriques et al. (2015) developed a model that included a more detailed treatment of gas cooling and accretion onto black holes, as well as the effects of mergers and feedback from supernovae. This model was able to reproduce the observed properties of galaxies in the local universe, as well as their evolution over cosmic time. Their model reproduces the transition of star-forming galaxies to become predominantly passive, while retaining the growth in the abundance of low-mass galaxies at $z < 2$. Overall, these improved versions of *radio mode* feedback models have played a crucial role in advancing our understanding of galaxy formation and evolution.

Another feedback mode used in semi-analytic models is the *quasar mode*. *Quasar mode* feedback is a mechanism, where energy released by the accretion of gas onto a supermassive black hole in the form of quasar radiation or winds regulates the growth of the black hole and the star formation in the host galaxy. *Quasar mode* feedback is commonly triggered by galaxy mergers or matter accretion coming from regulating disk instabilities. Granato et al. (2004) proposed that quasar winds can heat up and expel gas from the host galaxy, thereby suppressing star formation in short time-scales. They referred to this process as "quasar mode

feedback" and argued that it could explain the observed correlation between the mass of supermassive black holes and the properties of their host galaxies. Most SAMs assume that *quasar mode* accretion occurs simultaneously with starbursts because both processes are thought to be related to the same physical mechanism: the collapse of gas in the central regions of galaxies (Croton et al., 2006; Somerville et al., 2001; Henriques et al., 2013; Stevens et al., 2016). For example, gas-rich mergers between galaxies can drive both processes by funneling gas into the central regions of the merger remnant, where it can fuel the growth of the black hole and trigger star formation. Similarly, gravitational instabilities in the gas disk can lead to the formation of a massive central object that can trigger both quasar mode accretion and starbursts. Nevertheless, it is important to note that assuming *quasar mode* accretion and starbursts occur simultaneously may not always be accurate. More detailed modeling may be necessary in certain contexts, such as the study of low-mass galaxies or galaxies at high redshift.

The concept of *quasar mode* feedback was further developed and refined through theoretical models and observational studies. For example, Hopkins et al. (2006) introduced a model that included both *quasar* and *radio mode* feedback and found that it could reproduce the observed properties of galaxies at high redshift. Moreover, in the original Kauffmann & Haehnelt (2000) model (which many current SAMs use a modification of), only major mergers were considered to trigger the *quasar mode*. Croton et al. (2006) implemented black hole accretion by both major and minor mergers, allowing any merger that perturbs the cold gas within the disk to drive gas onto the central black hole. Though minor mergers were considered to ignite the *quasar mode*, its contribution is a small fraction of the effect that major mergers have in triggering the *quasar mode*. Croton et al. (2006), however, focuses on black hole growth and accretion. In this specific model of the SAM, *quasar mode* feedback is not included. Ten years later, the Semi-Analytic Galaxy Evolution model (SAGE) (Croton et al., 2016) implements *quasar mode* feedback. After rapid accretion as a result of a galaxy merger or disk instability, the model takes the rapid gas accretion rate and turns it into a total energy, some of which will escape the galaxy and halo through outflowing winds and be deposited in a hot gas reservoir. A more detailed explanation of this *quasar mode* feedback will be presented in chapter 2.

Semi-analytic models and hydrodynamical simulations implement AGN feedback differently. In SAMs, AGN feedback is often modeled as a simple energy injection into some gas resevoir, while in hydrodynamical simulations, the energy is released through jets or winds into the surrounding gas in subgrid cells. These differences lead to varying predictions for galaxy properties such as their mass, quenching, and morphology. The implementation of AGN feedback in hydrodynamical simulations is generally considered to be more physically realistic than in SAMs, as it takes into account more complex interactions between the AGN and the gas in the galaxy. However, hydrodynamical simulations are computationally expensive and require a high level of numerical resolution to accurately capture the details of the AGN feedback process. In contrast,

SAMs are computationally less expensive, but they rely on assumptions and simplified models to describe the AGN feedback process.

Another important contributor to galaxy quenching is SNe feedback. SNe feedback happens when very massive stars with short lifetimes explode, exerting enough energy to 1) heat up the cold gas within the galactic disk, or 2) eject the cold gas outside of the galaxy and halo. For every star formation episode, the massive stars soon to die in the form of Type-II supernova, recycling their mass and metals to the interstellar medium. Observations from Martin (1999) suggest that cold gas heated by SNe should be proportional to the rate at which new stars form. Typically in cosmological simulations, low-mass galaxies with shallow potentials that experience strong SNe feedback can remove both cold and hot gas from the galaxy and halo, depriving the galaxy of any future star formation episodes. On the other hand, massive galaxies make it difficult for hot gas to escape the halo, as their gravitational potential is much harder to overcome. In cases where SNe feedback ejects gas outside the halo, the ejected gas is allowed to be reincorporated into the halo at later times. The reincorporation time-scale is where many SAMs differ. Croton et al. (2006) assumed that some fraction of the ejected gas return to the halo after a halo dynamical time. This was applied independent of halo mass. However, doing that could alter the number of low-mass halos, so Croton et al. (2016) allowed the reincorporation rate of gas to increase with halo mass. Immediately after the reincorporation happens, the hot gas is allowed to cool and later form stars. Henriques et al. (2013) implemented an increased time delay for gas to be reincorporated after ejection in a galactic wind, which resulted in reducing the growth of low-mass systems at high redshift (z>2). This was compensated by the enhanced growth between $z = 2 - 0$ as the ejected gas would return, cool down, and fuel star formation. This allowed for a better match to the observed evolution of the stellar mass function. In this model, the time-scale for the gas reincorporation scaled with halo mass and redshift. Henriques et al. (2015) showed that galaxies more massive than $10^{11}\,M_{\odot}$ are not greatly affected by SNe feedback, while the quenched fraction of central galaxies with stellar masses greater than $10^{10}\,M_{\odot}$ increases significantly, suggesting that AGN feedback plays a large role in quenching massive galaxies.

All three forms of feedback used in SAMs (*radio mode*, *quasar mode*, and SNe feedback) play an important role in star formation quenching processes and how galaxies assembly their mass. Part of the work done in chapter 4 looks at the correlation between star formation quenching, stellar mass, and halo mass by exploring different modifications of the black hole physics and its effect on the stellar mass scatter within the stellar mass-to-halo mass relation.

CHAPTER 2

Semi-analytic modeling

Semi-analytic models (SAMs) are a powerful tool used to study the formation and evolution of galaxies within the context of the large-scale structure of the Universe. SAMs combine a set of analytic prescriptions with the results from numerical simulations of the growth of cosmic structure. These models are constructed by applying physically-motivated equations of the evolution of the baryonic components of a galaxy to dark matter halos. The analytical treatment of galaxy formation is then combined with the statistical properties of dark matter halos, such as their mass function and merger histories, to predict the observed properties of galaxies. SAMs can provide a valuable insight into the complex physical processes that govern the formation of galaxies. SAMs are used to investigate the role of different physical mechanisms, such as star formation, feedback from supernovae, and mergers. Moreover, SAMs provide a flexible framework that can be easily modified to test different scenarios and assumptions. For example, they can be used to study the impact of changes in the cosmological parameters (Gilmore et al., 2012; Perez et al., 2022), the initial mass function of stars (Safarzadeh et al., 2017), or the strength of feedback processes on the evolution of galaxies (Pandya et al., 2020).

SAMs have become a widely used tool due to their ability to make detailed predictions about the observable galaxy properties, such as their luminosity, angular momentum, black hole seeding, morphology, and colors. SAMs are also used to make predictions for upcoming surveys, such as datasets from the James Webb Space Telescope (JWST) (Yung et al., 2022), and to interpret the data obtained from past surveys, such as the Sloan Digital Sky Survey (Behroozi et al., 2019) and the Hubble Space Telescope (HST) (Lu et al., 2014).

2.1 N-body simulations of dark matter only

N-body simulations are the backbones of semi-analytic models and hydrodynamical simulations. They are used to model the gravitational interactions between a large number of particles in a system (Bertschinger, 1998; Bagla, 2005). The basic idea behind N-body simulations is to numerically integrate the equations of motion for each individual particle in a system as they interact with each other through gravity. In dark matter-only simulations, baryonic matter is treated as dark matter particles.

The hybrid N-body simulation method combines the advantages of both particle-based and mesh-based methods to accurately simulate a wide range of scales in a cosmological context. In this approach, particle-based methods are used on large scales to capture the large-scale structure formation, while mesh-based methods are employed on small scales to capture the detailed structure of individual halos. One example of

a hybrid N-body simulation method is the Tree-PM algorithm, which combines a particle-mesh method with a hierarchical tree algorithm to solve for the gravitational forces between particles (Efstathiou et al., 1985; Springel et al., 2005; Vogelsberger et al., 2014a). Another example is the Adaptive Refinement Tree (ART) code (Kravtsov et al., 1997). This method uses a tree algorithm to refine the mesh resolution adaptively, allowing for a higher resolution in regions of higher density. Hybrid N-body simulation methods have proven to be effective in simulating large-scale structure formation in a cosmological context while maintaining a high level of accuracy in resolving the detailed structure of individual halos. However, these methods still require significant computational resources and can be more challenging to implement than purely particle-based or mesh-based methods.

2.2 Merger trees

Merger trees in numerical simulations track the growth and merging of dark matter halos over cosmic time, providing insight into the hierarchical buildup of cosmic structure. The construction of merger trees involves identifying the halos and their progenitors at different snapshots in the simulation. Once the halos have been identified, they are linked to form a lineage over time. Figure 2.1 shows a schematic view of a merger tree. The formation of new combined halos may happen at each time-step of the simulation, which is stored in a merger tree.

The first step of creating a merger tree involves identifying dark matter halos, and there are several approaches for this. One approach involves using a Friends-of-Friends (FoF) method (Davis et al., 1985). The basic idea behind FoF is to group together particles that are in close proximity to each other, based on a linking length parameter. Specifically, particles are considered to be "friends" if their separation is less than the linking length, and groups of particles that have overlapping sets of friends are considered to be part of the same halo. Once the FoF groups have been identified, SUBFIND performs a more detailed analysis to locate substructures within each group. It does this by identifying density peaks within the group and tracing particles that are gravitationally bound to each peak. These density peaks represent potential subhalos or substructures within the larger halo. SUBFIND then applies a series of refinement algorithms to improve the accuracy of its substructure identification. These algorithms include removing unbound particles, resolving overlapping substructures, and identifying sub-substructures within larger substructures. Lastly, SUBFIND calculates various properties of the identified substructures, such as their mass, size, and shape, as well as their position and velocity within the larger halo. One advantage of FoF is that it is computationally efficient. Additionally, it can be applied to both particle-based and mesh-based simulations. However, FoF does have some limitations, such as the fact that it tends to merge halos together, which can lead to overestimates of halo masses (Genel et al., 2009; More et al., 2011a). Despite its limitations, FoF provides a useful tool for iden-

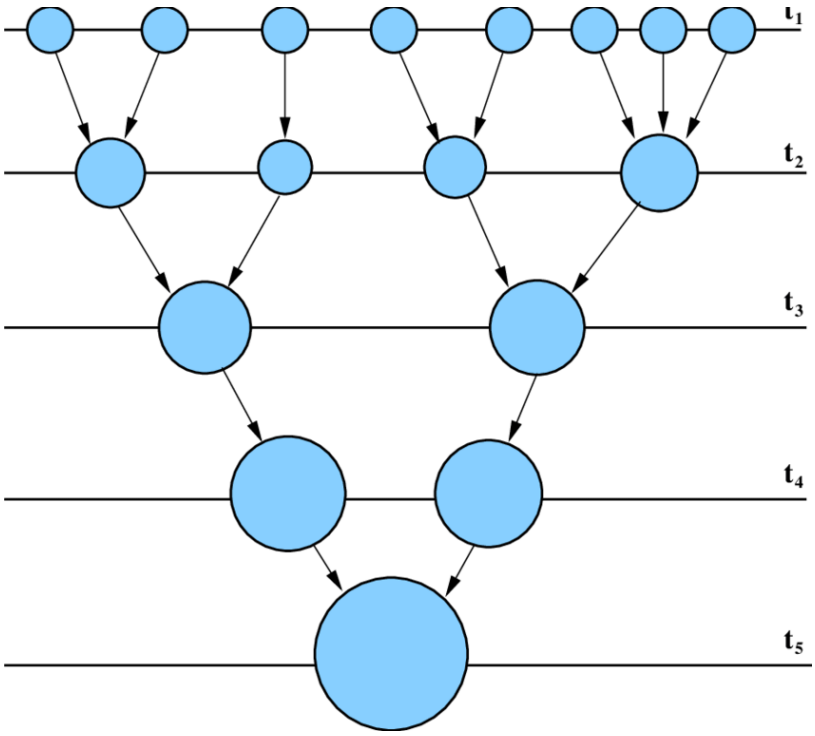

Figure 2.1: An illustration of a dark matter halo merger tree. Each circle represents a dark matter halo. The size of the circle encodes the halo mass. Each horizontal line shows the simulation snapshot in which the halo was taken at timestep t_i. Halos grow through merging with other massive halos or smaller ones. t_5 shows the final halo. Image credit: Baugh (2006)

tifying dark matter halos in cosmological simulations, which is a crucial step for studying galaxy formation and evolution.

Another approach to identify halos uses the Amiga's Halo Finder (AHF), which is a grid-based algorithm (Knollmann & Knebe, 2009). AHF uses a density field approach to identify halos by locating regions with overdensities of particles. First, AHF calculates the local density of each particle using a kernel-based method. The resulting density field is then used to identify regions with high densities, which are taken as the centers of the halos. From these centers, AHF constructs spherical shells around each halo and iteratively adjusts their radii until the virial radius is reached. Substructures within each halo are identified using a saddle-point search algorithm, which allows for the identification of both distinct subhalos and diffuse overdensities. One of its advantages is that it is able to identify halos in simulations with different resolutions and particle numbers, making it a versatile tool for different types of simulations. One limitation of AHF is that it may miss subhalos or underestimate their masses in galaxy clusters. This is because AHF uses a density threshold to identify halos and subhalos, which can lead to the merging of subhalos or the exclusion of small subhalos in high-density regions (Behroozi et al., 2015). Another limitation of AHF is that it may overestimate the size and mass of halos that are not in dynamical equilibrium. This can occur, for example, when a halo is undergoing a major merger or is in the process of formation. AHF also relies on the assumption that halo density profiles follow a universal profile, such as the Navarro-Frenk-White (NFW) profile. However, this may not be the case for all halos, particularly for those that have undergone significant mergers or have experienced interactions with their environment.

Another important approach is using ROCKSTAR, a phase-space-based algorithm that identifies halos and subhalos as locally overdense and kinematically cold regions in six-dimensional phase space (three spatial dimensions and three velocity dimensions) (Behroozi et al., 2013b). ROCKSTAR first identifies all particles within a simulation that are gravitationally bound to each other, and then uses a hierarchical merger tree algorithm to group these particles into halos and subhalos. One of the main limitations is that it may miss smaller substructures within larger halos or may merge nearby halos into one. This is due to the choice of linking length parameter used in the algorithm, which affects the identification of substructures (Behroozi et al., 2015). ROCKSTAR also struggles with identifying halos with extremely elongated shapes, as the algorithm assumes a spherical shape for halos. Despite these limitations, ROCKSTAR has been shown to be a reliable and efficient halo finder for a wide range of simulations, including both dark matter only and hydrodynamic simulations. In particular, it has been used in many large-scale simulations such as the ILLUSTRISTNG simulation (Springel et al., 2018) and the EAGLE simulation (McAlpine et al., 2016). Efforts have also been made to improve the performance of ROCKSTAR, such as by implementing an adaptive linking length scheme to improve the identification of substructures (Behroozi et al., 2013b).

Once the merger trees are constructed, they can be used to study a variety of astrophysical phenomena, including galaxy clustering, galaxy formation, and the intergalactic medium. For example, merger trees can be used to study the correlation between galaxy properties and the mass and merger history of their host halos (Moster et al., 2013). Despite the uncertainties described above, merger trees remain a valuable tool for understanding the growth of cosmic structure and the formation and evolution of galaxies. For more information on halo-finders, see Knebe et al. (2011).

2.3 Modeling galaxy properties in SAMs

SAMs are a valuable tool for studying galaxy formation and evolution, and can provide insights into the physical processes that govern the growth and properties of galaxies. One of the key strengths of SAMs is their ability to follow the hierarchical growth of dark matter halos and the resulting formation and evolution of galaxies within them. SAMs incorporate physical processes such as gas infall, gas cooling, star formation, gas recycling, ejection, heating, and feedback from supernovae and AGN. These are used to predict the properties of galaxies such as the stellar mass function, the cosmic star formation density, metallicity, and others. Figure 2.2 shows a schematic diagram of how a SAM works. First, the merger trees are included as the input to the simulation. Then, the semi-analytic model populates the dark matter halos with baryonic physics as a function of time. Each halo starts with a hot gas reservoir. Cold gas cools to form disks and later stars. When a less massive halo infalls into the main halo, it becomes a subhalo, or a satellite galaxy. Within each of the halos in the merger tree, the SAM contains a reservoir for ejected gas, hot gas, and a stellar and gaseous disk. At every timestep, the simulation checks for star formation, cooling, gas re-incorporation, gas ejected, gas recycling, heating, tidal stripping, and other processes. In general, these are the ingredients that are built into a semi-analytic model.

2.3.1 Gas reservoirs

SAMs design reservoirs that represent the gas that is available for star formation, cooling, re-incorporation, ejection, and heating. The gas reservoirs are typically divided into different components based on their physical state and location within the (sub)halo. For example, the hot gas reservoir is the gas that is located in the halo of the galaxy and is heated by supernova and AGN feedback. There is also an ejected hot gas reservoir that represents gas that has been ejected due to feedback processses. The cold gas reservoir is the gas that is located in the disk of the galaxy and is available for star formation. The evolution of the baryonic gas reservoirs in SAMs is typically modeled using a set of differential equations that describe the rates of gas inflow, outflow, and consumption due to star formation. The inflow of gas onto the galaxy is typically assumed to be driven by accretion, while the outflow of gas is driven by supernova feedback and/or AGN

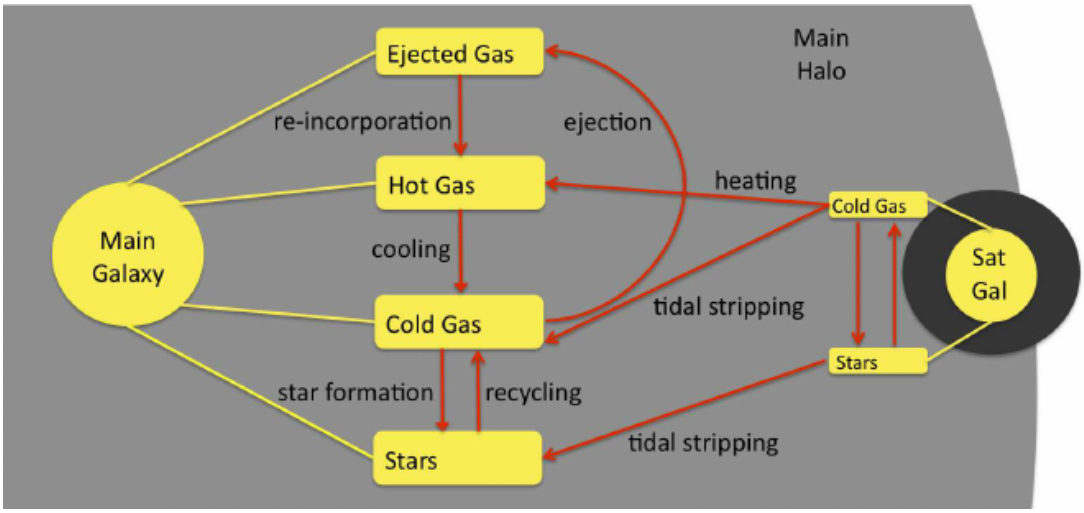

Figure 2.2: A schematic illustration of the components for the evolution of a central galaxy (Main galaxy) within a dark matter halo (grey shade) in a semi-analytic model. The right hand side shows an accreted satellite galaxy with its own dark matter halo. The yellow boxes represent the different analytical processes that the baryons go through. The red arrows show the physical prescriptions implemented. Image credit: Figure 1 from Starkenburg et al. (2013)

feedback.

2.3.2 Cooling

Gas cooling drives the formation and evolution of galaxies (Navarro & Benz, 1991). In SAMs, gas cooling is modeled using the cooling function, which describes the rate at which gas radiates energy as it cools. The cooling function depends on several parameters, including the gas metallicity and the gas density. One common approach to modeling gas cooling in SAMs is to use the cooling rates calculated by photoionization and spectral synthesis codes, such as CLOUDY (Ferland et al., 2013). CLOUDY computes the cooling rates for gas of different metallicities and densities, taking into account various cooling mechanisms such as collisional excitation, recombination, and free-free emission. Another approach is to use tabulated cooling functions, which provide the cooling rates as a function of gas density and temperature for a given metallicity. These cooling functions are usually derived from the radiative transfer codes, but they allow for faster calculations in SAMs as they do not require the cooling rates to be calculated on-the-fly. To calculate the rate at which gas cools, SAMs assume that halo gas first settles into an isothermal density profile (equation 2.1) given by White & Frenk (1991) which is dependent on the virial temperature (equation 2.2).

$$\rho_g(r) = \frac{m_{\rm hot}}{4\pi R_{\rm vir} r^2}, \tag{2.1}$$

$$T_{\rm vir} = \frac{1}{2}\frac{\mu m_p}{k} V_{\rm vir}^2 \ {\rm K}, \tag{2.2}$$

Cooling time is directly calculable at any radius (see figure 2.3). The cooling radius, $r_{\rm cool}$, is defined as the radius at which the cooling time equals a time-scale that varies based on the SAM. In the case of Croton et al. (2016), $r_{\rm cool}$ is defined as the radius at which the cooling time equals the dynamical time, $t_{\rm cool} = \frac{R_{\rm vir}}{V_{\rm vir}}$. Assuming solutions from Bertschinger (1989), the cooling time is given in equation 2.3.

$$t_{\rm cool} = \frac{2}{3}\frac{\mu m_p \, kT_{\rm vir}}{\rho_g(r)\Lambda(T_{\rm vir}, Z)}, \tag{2.3}$$

where μ is the mean molecular weight of the gas, m_p is the mass of the proton, k is the Stefan-Boltzmann constant, and Λ is the cooling function of the gas, which describes how efficiently the gas can radiate energy away and is dependent on the virial temperature of the system, $T_{\rm vir}$, and the metallicity of gas Z. After calculating the cooling time, an instantaneous cooling rate is obtained.

$$\frac{{\rm d}(m_{\rm cool})}{{\rm d}t} = \frac{1}{2}\frac{r_{\rm cool}}{R_{\rm vir}}\frac{m_{\rm hot}}{t_{\rm cool}}, \tag{2.4}$$

Equation 2.4 provides the "hot mode" of accretion, so long as $r_{\rm cool} < R_{\rm vir}$. If $r_{\rm cool} > R_{\rm vir}$, the halos are assumed to be cooling in the "cold mode", meaning the "cooling" time is no longer limited by cooling but rather the time it takes to dynamically move to the cold gas disk. Overall, the modeling of gas cooling in SAMs is a complex process that requires careful consideration of various physical processes.

2.3.3 Star formation

The rate at which star formation occurs depends on the availability of gas, and other factors such as the efficiency of the conversion process and the influence of feedback from stars and AGN. SAMs incorporate several recipes for star formation. One common approach is to use the Kennicutt-Schmidt law (Kennicutt, 1998), which relates the surface density of gas to the surface density of star formation.

$$\frac{{\rm d}(m_{\rm SFR})}{{\rm d}t} = \varepsilon_{\rm SF}\frac{m_{\rm cold} - m_{\rm crit}}{t_{\rm dyn}}, \tag{2.5}$$

where $\varepsilon_{\rm SF}$ is the star formation efficiency (usually a free parameter), $m_{\rm cold}$ is the cold gas mass, $m_{\rm crit}$ is mass at which above it, cold gas can form stars, and $t_{\rm dyn} = \frac{r_{\rm disk}}{V_{\rm vir}}$ is the dynamical time of the disk. The radius of the disk, $r_{\rm disk}$ is obtained using the spin of the halo,λ, and the virial radius in the following form: $r_{\rm disk} = \frac{3}{\sqrt{2}}\lambda R_{\rm vir}$. To calculate $m_{\rm crit}$,

$$m_{\rm crit} = 3.8 \times 10^9 \left(\frac{V_{\rm vir}}{200\ {\rm Kms}^{-1}} \right) \left(\frac{r_{\rm disk}}{10\ {\rm kpc}} \right) {\rm M}_\odot, \tag{2.6}$$

SAMs aim to capture the complex interplay between gas, stars, and feedback in galaxy formation, with star formation being a crucial component of this process. While the implementation of the recipes and assumptions used in SAMs can vary, these models have proven to be a powerful tool for understanding the formation and evolution of galaxies in a cosmological context.

2.3.4 Chemical evolution

Chemical evolution in semi-analytic models involves tracking the enrichment of gas and stars with heavy elements produced by stars over cosmic time. The metallicity of gas and stars in galaxies is important in determining their properties, such as star formation rate. SAMs track the chemical evolution of galaxies, where the metallicity of gas is assumed to be well-mixed and the rate of change in the gas metallicity is given by the balance between metal production by stars and metal consumption by various processes, such as star formation, gas outflows, and accretion of metal-poor gas. The yields of different elements produced by stars are typically modeled as free parameters in semi-analytic models, but often these are tied to assumptions about the IMF. These yields can depend on various factors such as the initial mass function of stars and the type of supernova explosions. For example, the semi-analytic model GALFORM incorporates a modified version of the metal yield model by Woosley & Weaver (1995), which takes into account the metallicity dependence of the mass loss in supernova explosions. The modeling of chemical enrichment in semi-analytic models is often compared to observational data, such as the metallicity-mass relation and the evolution of the cosmic metallicity density. Fontanot et al. (2009) used the SAM GALFORM to predict the evolution of the cosmic metallicity density and compared their results to observations of the metallicity evolution in the intergalactic medium. They found that the model was able to reproduce the observed trends reasonably well, indicating that the assumptions made in the model about the metal production and consumption processes were broadly consistent with observations. The modeling of chemical enrichment is an ongoing area of research, as more detailed models are developed to account for the production and transport of heavy elements in galaxies.

2.3.5 Mergers

Galaxy mergers play a critical role in shaping the formation and evolution of galaxies. In semi-analytic models, galaxy mergers are divided into two types: major mergers and minor mergers. Major mergers occur between two galaxies with similar masses, while minor mergers occur between a smaller satellite galaxy and a larger host galaxy. During a merger, the two galaxies undergo dynamical friction, losing energy and angular momentum as they approach each other. The central black holes of the two galaxies can also coalesce,

leading to the formation of a more massive black hole. The gas in the merging galaxies can also undergo shocks and form new stars, increasing the overall star formation rate of the system. In a semi-analytic model, the merger rate is typically set by the merger tree. Several factors are co-dependent with the merger rate, such as the dynamical friction timescale, the halo mass function, and the merger mass ratio distribution (Zentner & Bullock, 2003; Boylan-Kolchin et al., 2008).

2.3.6 Black hole growth

Black hole growth in semi-analytic models is often linked to two main channels: gas accretion and mergers with other black holes. The rate of gas accretion onto a black hole is usually modeled using the Bondi-Hoyle-Lyttleton formula (Bondi, 1952; Edgar, 2004), which relates the accretion rate to the properties of the surrounding gas, such as its density and velocity. This accretion process can be further modified by factors such as the presence of a hot gas halo around the galaxy, which can enhance the accretion rate (equation 2.7).

$$\frac{\mathrm{d}(m_{\mathrm{bondi}})}{\mathrm{d}t} = 2.5\pi \mathrm{G}^2 \frac{m_{\mathrm{BH}}^2 \rho_0}{c_s}^3, \tag{2.7}$$

where $\frac{\mathrm{d}(m_{\mathrm{bondi}})}{\mathrm{d}t}$ is the black hole accretion rate, G is the gravitational constant, m_{BH} is the mass of the black hole, ρ_0 is the density of the hot gas around the black hole, and c_s is the sound speed, which is approximated by the virial velocity of the parent halo, V_{vir}.

The growth of black holes through mergers is modeled by assuming that black holes merge when they are gravitationally bound and that the merger timescale is proportional to the binary separation. Generally, black hole growth is controlled through a free parameter, one which is either related to the gas accretion, galaxy mergers, or both. This parameter reflects our current uncertainty in the details of black hole growth, but is typically chosen to match a set of observations to calibrate the model, or match observations of the black hole mass function at $z = 0$. There are many different variations of the black hole growth models used in SAMs, and their predictions can vary significantly depending on the specific assumptions made (Croton et al., 2006; Croton et al., 2016; Henriques et al., 2013; Somerville & Davé, 2015). However, overall, SAMs have been successful in reproducing the observed correlation between black hole mass and bulge mass (Somerville et al., 2001; Stevens et al., 2016).

2.3.7 Feedback processes

SAMs implement two general modes of feedback: AGN and supernova. AGN feedback plays a crucial role in regulating the growth of galaxies and their central black holes. SAMs generally include two modes of AGN feedback: *quasar mode* and *radio mode*. As discussed previously, *quasar mode* refers to the high-accretion-rate phase of AGN, where the AGN radiates at the Eddington limit and drives powerful outflows that can affect

the entire host galaxy. The *radio mode* refers to the low-accretion-rate phase of AGN, where the AGN injects energy into the interstellar medium (ISM), heating the gas and potentially suppressing further star formation. In semi-analytic models, AGN feedback is typically implemented using an energetic feedback prescription that depends on the properties of the black hole and the surrounding gas. One common approach is to assume that a fraction of the accreted mass onto the black hole is converted into energy that is then deposited into the ISM (Croton et al., 2016). The efficiency of the AGN heating is a free parameter in models. The details of how this AGN feedback operates and the parameters that govern it are still the subject of ongoing research and debate.

Supernova feedback is strongly tied to the gas reservoir and star formation in galaxies. When a supernova explodes, it injects energy and momentum into the surrounding gas, which can drive outflows and prevent the gas from cooling and forming stars. The efficiency of this process is usually described by the mass-loading factor due to supernovae, which determines the fraction of gas that is ejected from the galaxy per unit of star formation. In SAMs, the mass-loading factor due to supernovae may be a free parameter that is calibrated to match observations. The energy and momentum injected by supernovae can also depend on the star formation rate and metallicity of the gas (Cole et al., 2000; Somerville et al., 2001; Croton et al., 2016). One popular approach for modeling supernova feedback in SAMs include the stochastic heating model, which assumes that the energy from supernovae is deposited randomly in the surrounding gas, and the momentum-driven wind model, which assumes that the momentum from supernovae is the main driver of outflows. The implementation of supernova feedback in SAMs is an active area of research.

We cover the specific implementation of each of these processes for the SAM we used, DARK SAGE, in the next subsection.

2.3.8 Gas reincorporation

Gas reincorporation refers to the process by which gas that has been expelled from a galaxy is re-accreted back onto the galaxy's disk or halo. This gas can be recycled from outflows driven by supernovae or active galactic nuclei, or it can come from the intergalactic medium. The reincorporation of gas can significantly affect a galaxy's star formation rate and metallicity. In semi-analytic models, gas reincorporation is typically modeled using simple prescriptions that take into account the physical processes involved in gas outflows and accretion. Here, I present equations from Croton et al. (2016) describing how reincorporation and ejected mass are calculated.

To reincorporate gas from the ejected gas reservoir into the hot halo,

$$\frac{\mathrm{d}(m_{\mathrm{reinc}})}{\mathrm{d}t} = \left(\frac{V_{\mathrm{vir}}}{V_{\mathrm{crit}}} - 1\right) \frac{m_{\mathrm{ejected}}}{t_{\mathrm{dyn}}}, \tag{2.8}$$

where $t_{\rm dyn}$ is the dynamical time of the halo and $V_{\rm crit}$ is the escape velocity of the particles experiencing a supernova event. The gas mass ejected from the galaxy and/or halo, $m_{\rm ejected}$, is calculated using equation 2.9.

$$\frac{\mathrm{d}(m_{\rm ejected})}{\mathrm{d}t} = \frac{\frac{\mathrm{d}(E_{\rm Excess})}{\mathrm{d}t}}{E_{\rm hot}} m_{\rm hot}, \tag{2.9}$$

where $\frac{\mathrm{d}(E_{\rm Excess})}{\mathrm{d}t}$ is the excess energy in the hot gas after supernova reheating. When $\frac{\mathrm{d}(E_{\rm Excess})}{\mathrm{d}t} < 0$, the amount of energy reheated in the disk is not enough to unbind the hot halo gas. Nonetheless, when $\frac{\mathrm{d}(E_{\rm Excess})}{\mathrm{d}t} > 0$, then the energy is sufficient to unbind some of the hot halo gas and eject it. The excess energy is calculated in equation 2.10.

$$\frac{\mathrm{d}(E_{\rm Excess})}{\mathrm{d}t} = \frac{1}{2}\left(\varepsilon_{\rm halo}\frac{\mathrm{d}(m_{\rm SFR})}{\mathrm{d}t}V_{\rm SN}^2 - \frac{\mathrm{d}(m_{\rm heat})}{\mathrm{d}t}V_{\rm vir}^2\right), \tag{2.10}$$

where $\varepsilon_{\rm halo}$ is the efficiency of supernovae to unbind gas from the hot halo, $\frac{\mathrm{d}(m_{\rm SFR})}{\mathrm{d}t}$ is the star formation rate calculated in equation 2.5. $V_{\rm SN}$ is the mean energy in velocity of the matter ejected by the supernova, where $V_{\rm SN} = 630\ \mathrm{km\,s^{-1}}$. $\frac{\mathrm{d}(m_{\rm heat})}{\mathrm{d}t}$ is the amount of gas mass heated by supernova, where $\frac{\mathrm{d}(m_{\rm heat})}{\mathrm{d}t} = \varepsilon_{\rm disk}\frac{\mathrm{d}(m_{\rm SFR})}{\mathrm{d}t}$ and $\varepsilon_{\rm disk}$ is the mass-loading factor due to supernova.

As described in the previous chapter, gas may also be ejected by quasar mode feedback winds. The way in which this energy is calculated is described in equation 2.16. Overall, the modeling of gas reservoirs is an important component of SAMs that allows for the prediction of key observable properties of galaxies, such as their star formation rates and gas content, which are strongly tied to feedback.

2.3.9 SAM Dark Sage

The semi-analytic model DARK SAGE's (Stevens et al., 2016) framework comes from SAGE (Croton et al., 2016). The focus on tracing the evolution of the galactic disk through annuli structures is what makes DARK SAGE stand out from other semi-analytic models. DARK SAGE self-consistently evolves the one dimensional structure of disks in galaxies using 30 equally-spaced logarithmic bins of fixed angular momentum, a method inspired by Fu et al. (2010, 2013). Most SAMs trace the physics within the disk as global quantities, but DARK SAGE is able to calculate local processes within annuli such as star formation rates, disk instabilities, AGN energy dissipation, and so forth. In DARK SAGE, galaxies are formed within halos of hot gas that cool down through radiative cooling and condensation of hot gas (White & Rees, 1978). Once it cools down, the gas collapses to form a gravitationally-supported disk. DARK SAGE uses two annular disk structures, for stars and gas, to calculate physical processes (Panel (a) of Figure 2.3). Gas from the hot halo can also cool when gas disk and spin vectors are misaligned. Star formation process can occur (Panel (b) of same the figure). The stellar and gas disks may also be misaligned due to precession, which is a natural consequence of having a

rotating fluid body in an axisymmetric potential where their axes of symmetry are offset. In fact, the gas disk precesses to becomes parallel to the stellar spin axis until it reaches coplanarity (Panel (c) of same the figure). DARK SAGE galaxies resolve Toomre (1963) instabilities by transferring unstable gas or stars to neighboring annuli as it conserves angular momentum (Panel (d) of same the figure). In some cases, an unstable annulus may go starburst to resolve instabilities. However, if instabilities reach the inner most annulus, unstable stars are added to the instability-driven bulge, whereas unstable gas is added directly into the central black hole. In addition, DARK SAGE allows stellar disks to be completely destroyed if galaxies have a major merger. The resulting merged galaxy will acquire a newly formed stellar disk structure. In the case of a minor merger, the stellar disk of the satellite is directly added into the merger-driven bulge. In both major and minor mergers, the gas from the secondary goes to the primary's gas disk annuli of the respective specific angular momentum (Panel (e) of same the figure).

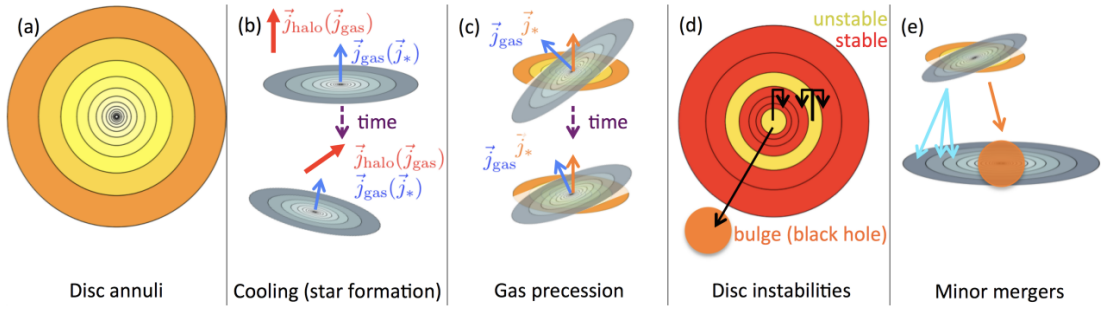

Figure 2.3: An illustration describing the disk structures in semi-analytic model DARK SAGE. Panel (a) shows the disk of a galaxy broken into 30 logarithmic bins. Inside each annulus, star formation rates, instabilities, metallicity mixing, and other galaxy evolution processes happen. Panel (b) shows how gas cools as the cold gas specific angular momentum vector is parallel to that of the halo. Gas cooling also takes place when the gas and halo spin vectors are offset, allowing the direction of the gas disk to change. Panel (c) shows how DARK SAGE lets the cold gas and stellar disk to misalign. By design, they eventually align. Panel (d) illustrates the mass transfer between annuli when the gas and/or stellar disk have unstable disks. Panel (e) shows how the stellar and gas disks transfer material to the most massive galaxy when a satellite merger occurs. Image credit: Figure 2 from Stevens et al. (2016)

When a merger happens, before determining how much gas is added into the primary's gas disk, a fraction (f_{BH}) of the gas feeds directly the central black hole of the primary (see equation 2.14). Once that happens, after the gas of the secondary goes to the respective specific angular momentum annulus, the annulus goes starburst. Both major and minor mergers are important processes that may trigger AGN and stellar feedback activity. The careful treatments within the disk structures of galaxies are what makes DARK SAGE an excellent tool to study star formation quenching and galactic angular momentum.

2.3.10 DARK SAGE calculates SF

In DARK SAGE, cold gas within each annulus lead to the formation of giant molecular clouds that collapse to form stars. The cold gas disk includes hydrogen, helium, some ionized gas, and metals. The formation of stars is dependent on the local H_2 content and the star formation surface density is defined as:

$$\Sigma_{\rm SFR}(r) = \varepsilon_{\rm SF}\Sigma_{\rm H_2}(r), \tag{2.11}$$

where $\varepsilon_{\rm SF}$ is the star formation efficiency (see its value on table 2.1) and $\Sigma_{\rm H_2}$ is the molecular hydrogen surface density which is calculated within each annulus. Feedback mechanisms in the model can halt these star formation processes. This is only one of three channels of star formation in DARK SAGE. DARK SAGE also calculates star formation from Tommre unstable gas, which forms more stars than the H_2-based channel, and through merger starburst.

DARK SAGE quenches galaxies by AGN feedback in *radio mode* and *quasar mode* feedback. Black hole growth is mainly driven by how many major or minor mergers the galaxy has experienced. The unstable gas within the galaxy's disk also contributes to black hole growth, but it does not play a major part. An important remark is that there is no mass threshold in which AGN ignites. AGN feedback starts based on the internal physical dynamics of every galaxy in the simulation. Lastly, the quenching from ram-pressure stripping has been shown to affect mainly galaxies with low stellar masses that live in massive halos (see Fig. 8 of Stevens & Brown 2017).

2.3.10.1 Radio mode in DARK SAGE

DARK SAGE uses an identical *radio mode* prescription as SAGE (Croton et al., 2016), a model that implemented a *radio efficiency* parameter, $\kappa_{\rm R}$, to control for the strength of the black hole accretion rate (see table 2.1 for the $\kappa_{\rm R}$ value). The Bondi accretion rate is written as:

$$\frac{{\rm d}(m_{\rm BH,R})}{{\rm d}t} = \kappa_{\rm R}\,\frac{15}{16}\pi {\rm G}\mu\, m_p\,\frac{kT}{\Lambda} m_{\rm BH,} \tag{2.12}$$

where G is the gravitational constant, μ is the mean molecular weight of the gas, m_p is the mass of the proton, k is the Stefan-Boltzmann constant, and Λ is the cooling function of the gas, which describes how efficiently the gas can radiate energy away. T is assumed to be the virial temperature of the hot gas, and $m_{\rm BH}$ is the mass of the black hole. Using this accretion rate, we can estimate the luminosity of the black hole to be $L_{\rm BH,R} = \eta\frac{{\rm d}(m_{\rm BH,R})}{{\rm d}t}\,c^2$, where $\eta = 0.1$ is the nominal radiative mass efficiency. This is used to estimate the amount of heating injected into the cooling gas, which can be estimated as:

$$\frac{\mathrm{d}(m_{\mathrm{heat}})}{\mathrm{d}t} = \frac{\mathrm{L_{BH,R}}}{0.5\, V_{\mathrm{vir}}^2}, \tag{2.13}$$

Here, they assume that the cold gas is heated by the *radio mode* feedback up to some radius (r_{heat}) at which below that no gas will ever cool back again. This shows that the heating rates dropped significantly compared to the Croton et al. (2006) model, which allows for a more meaningful comparison with observations.

Although the Bondi accretion rate estimates well the rate at which gas accretes onto a black hole, there are several limitations to this approach. One limitation is that it assumes that the gas is moving very slowly relative to the black hole, which may not always be the case close to the black hole, where there are significant gas motions. This can lead to significant uncertainties in the predicted accretion rates. Another limitation is that equation 2.12 assumes that the gas is smoothly distributed around the black hole, which may not always be the case in the real Universe, where there are clumps or filaments of gas surrounding the black hole. In such cases, the actual accretion rate may be significantly lower than the Bondi rate. It is important to keep in mind its limitations and to use caution when applying it to other situations.

2.3.10.2 Quasar mode in DARK SAGE

For *quasar mode*, DARK SAGE calculates the amount of energy produced by the black hole accretion. Then, it checks if the energy is enough to heat up the gas within each annulus in the model. The change in black hole mass due to *quasar mode* is:

$$\Delta m_{\mathrm{BH,Q}} = \frac{f'_{\mathrm{BH}}\, m_{\mathrm{cold/unstable}}}{1 + (\ 280\ \mathrm{km\ s^{-1}} / \ V_{\mathrm{vir}}\ )^2}, \tag{2.14}$$

where f_{BH} is an accretion efficiency (see table 2.1) that controls the fraction of cold gas accretion coming from major/minor mergers or disk instabilities. Thus, f'_{BH} can be:

$$f'_{\mathrm{BH}} = \begin{cases} f_{\mathrm{BH}}\ \frac{m_{\mathrm{satellite}}}{m_{\mathrm{central}}} & \text{if merger} \\ f_{\mathrm{BH}} & \text{if disk instabilities} \end{cases} \tag{2.15}$$

DARK SAGE calculates the energy produced by *quasar mode* feedback on an annulus-by-annulus basis. The change in black hole mass (equation 2.14) is then used to calculate the energy produced by this *quasar mode* accretion:

$$E_{\mathrm{BH,Q}} = \kappa_{\mathrm{Q}}\ \frac{1}{2}\ \eta\ \Delta m_{\mathrm{BH,Q}}\ c^2, \tag{2.16}$$

where κ_{Q} is the efficiency which the quasar wind causes the gas to either be transferred to the gas reservoir

all heated up or escape the halo (see table 2.1). To determine which path the gas would take, DARK SAGE calculates the total thermal energy of the cold and hot gas:

$$\mathrm{E_{cold}} = \frac{1}{2}\, m_{\mathrm{cold}}\, V_{\mathrm{vir}}^2 \text{ and } \mathrm{E_{hot}} = \frac{1}{2}\, m_{\mathrm{hot}}\, V_{\mathrm{vir}}^2, \tag{2.17}$$

Thus, if the total energy is greater than $\mathrm{E_{cold}}$, the cold gas is added to the ejected gas reservoir within the halo. If the total energy is greater than $\mathrm{E_{cold}} + \mathrm{E_{hot}}$, then both cold and hot gas are ejected outside of the halo.

2.3.10.3 Supernova mode in DARK SAGE

In high-density regions, supernovae are able to heat up the gas, but the amount of energy injected in the gas mass depends on the local heating surface density of gas (as taken from Fu et al. (2013):

$$\Sigma_{\mathrm{reheated}}(\mathrm{r}) = \varepsilon_{\mathrm{disk}}\, \frac{\Sigma_{0,\mathrm{gas}}}{\Sigma_{\mathrm{gas}}(\mathrm{r})}\, \Sigma_{\mathrm{SFR}}(\mathrm{r}), \tag{2.18}$$

where $\Sigma_{0,\mathrm{gas}}$ is a reference surface density, Σ_{gas} is a gas surface density, $\Sigma_{\mathrm{SFR}}(\mathrm{r})$ is obtained from eq. 2.11 and the $\varepsilon_{\mathrm{disk}}$ parameter is the mass-loading factor (see table 2.1). As a lower limit for resolution purposes, supernova feedback occurs if a star formation event within an annuli produces stars with mass greater than $100\, h^{-1}\, \mathrm{M}_{\odot}$. In the following subsection, I will discuss the process of calibrating a SAM.

2.3.11 How to calibrate a SAM

In SAMs, the use of many physical prescriptions that approximate processes in galaxy formation results a number of free parameters that can be tuned to match observations. Because of the different implementations in certain equations describing galaxy formation such as AGN feedback, SNe feedback, cooling rate, amongst others, the end result may vary when comparing different SAMs. Each SAM uses its own recipe, merger trees, and set of free parameters that are tuned to different observational statistical relations of galaxy properties. Figure 2.4 shows a comparison between some SAMs and the different model prescriptions they use. Although these models include AGN and SNe feedback, some do not follow the same equation describing these processes.

Each SAM follows its own, unique recipe to simulate the formation and evolution of galaxies. While there are general principles that are shared by most SAMs, such as the conservation of mass/energy and the incorporation of physical processes like gas cooling, star formation, and feedback, the specific implementation and tuning of these processes can vary widely across different models. This is because the details of galaxy formation and evolution are complex and involve many interconnected physical processes that are not fully understood. As a result, SAMs must make a number of simplifying assumptions and parameterizations

	Model				
Feature	DURHAM	MUNICH	SANTA-CRUZ	MORGANA	GALICS
Merger Trees					
→ Analytic	Modified ePS	ePS	ePS	PINOCCHIO	×
→ N-body	✓	✓	✓	×	✓
Halo Profiles	Einasto	Isothermal	NFW	NFW	Empirical
Cooling Model					
→ Metal-dependent	✓	✓	✓	✓	✓
Star Formation	✓	✓	✓	✓	✓
Feedbacks					
→ SNe	✓	✓	✓	✓	✓
→ AGN	✓	✓	✓	✓	✓
→ Reionization	✓	×	✓	✓	✓
Merging					
→ Substructure[16]	N-body	N-body	DF	DF	N-body
→ Substructure–Substructure[19]	✓	×	✓	×	✓
Environments					
→ Ram Pressure Stripping	✓	✓	×	×	✓
→ Tidal Stripping	✓	×	✓	✓	✓
→ Harassment	×	×	×	×	×
Disks					
→ Disk Stability	✓	✓	✓	✓	✓
→ Dynamical Friction[27]	✓	×	×	×	×
→ Thickness	✓	×	×	×	×
Sizes					
→ Adiabatic contraction	✓	×	✓	✓	×
Chemical Enrichment	✓ [delayed[10]]	✓ [instant[29]]	✓ [delayed[30]]	✓ [instant]	✓ [delayed[31]]
Dust	GRASIL	Screen	Slab	GRASIL	Slab

Figure 2.4: Table showing how each semi-analytic model use similar or different physical prescriptions. This is important when taking into account the end result of each simulation. Image credit: Section 8.2, Table 2 from Benson (2010).

Parameter	Description	Value	Fixed
f_b	Cosmic baryon fraction	0.17	Yes
$\varepsilon_{\rm SF}$	Star formation efficiency from H_2 [10^{-4} Myr^{-1}]	3.96	No
$\theta_{\rm thresh}$	Threshold angle for stars and gas to be considered coplanar [degrees]	10.0	Yes
Y	Yield of metals from new stars	0.025	No
$\mathscr{R}$	Instantaneous recycling fraction	0.43	Yes
$\varepsilon_{\rm disc}$	Mass-loading factor due to supernovae at $\Sigma_{0,\rm gas}$	6.0	No
$\Sigma_{0,\rm gas}$	Surface density scaling for supernova reheating [$M_\odot$ pc^{-2}]	8.0	No
$\varepsilon_{\rm halo}$	Efficiency of supernovae to unbind gas from the hot halo	0.4	No
ϑ_t	Precession angle of gas discs about stars in a dynamical time [degrees]	5.0	Yes
$f_{\rm move}$	Fraction of unstable gas that moves to adjacent annuli	0.3	No
$f_{\rm major}$	Threshold mass ratio for a major merger	0.3	Yes
$f_{\rm BH}$	Rate of black hole growth during quasar mode accretion	0.03	No
$\kappa_{\rm R}$	Radio mode feedback efficiency	0.035	No
$\kappa_{\rm Q}$	Quasar mode feedback efficiency	0.005	Yes

Table 2.1: Free parameter values used in fiducial DARK SAGE. The fourth column shows which parameters are used to calibrate (Fixed=No) (Stevens et al., 2016).

in order to be computationally feasible, and these choices can have a significant impact on the predictions and results of the model. For example, in DARK SAGE, 14 parameters described in Table 2.1.

The cosmic baryon fraction, f_b, is the ratio of the mass of baryons to the total matter content in the Universe. The star formation efficiency, $\varepsilon_{\rm SF}$, represents the fraction of cold gas in a galaxy that is converted into stars per unit time. It helps determine the rate at which stars form in galaxies, as well as the amount of gas that is available for future star formation. However, the exact value of the star formation efficiency and its dependence on other physical parameters (such as the gas metallicity and the strength of feedback processes) are not well-constrained by observations and may vary from galaxy to galaxy. Therefore, the star formation efficiency is typically treated as a free parameter in SAMs. The threshold angle for stars and gas, $\theta_{\rm thresh}$, is the angle limit chosen for the stellar and gas disk to be considered coplanar. The yield of metals from new stars, Y, represents the fraction of the mass of a newly formed star that is converted into metals. The yield plays a key role in determining the chemical evolution of galaxies, as it governs the rate at which metals are produced and released into the interstellar medium, where they can be incorporated into new generations of stars. The mass-loading factor due to supernovae, $\varepsilon_{\rm disc}$, is the ratio of the mass of gas that is ejected from a galaxy by supernova explosions to the mass of stars that are formed in the galaxy. This parameter determines how much gas is removed from the galaxy's interstellar medium due to feedback processes.

The surface density scaling for supernova reheating, $\Sigma_{0,\rm gas}$, is the dependence of the energy input from supernovae on the surface density of the gas in a galaxy. This parameter regulates how much energy is deposited into the interstellar medium due to supernova explosions, and how efficiently this energy is able to drive outflows of gas from the galaxy. The efficiency of supernovae to unbind gas, $\varepsilon_{\rm halo}$, represents the fraction of the energy released by supernova explosions that is able to unbind gas from the hot, diffuse halo that surrounds galaxies. The precession angle of gas disks about stars, ϑ_t, is the angle by which the orientation of the gas disk changes with respect to the stars in a galaxy. This parameter is an important factor in regulating the angular momentum of the gas in a galaxy. The fraction of unstable gas that moves to adjacent annuli, $f_{\rm move}$, gives the amount of gas that was not able to be resolved by a starburst, and is therefore, transferred to a neighboring annulus. The threshold mass ratio for a major merger, $f_{\rm major}$, is the limit in which the model considers the merger to be major. The rate of black hole growth, $f_{\rm BH}$, provides the amount of gas that feeds directly into the central black hole, typically in a merger, during quasar mode accretion. Both $\kappa_{\rm R}$ and $\kappa_{\rm Q}$ are the *radio* and *quasar mode* feedback efficiencies previously discussed.

In SAMs, there are some parameters that are left free (not fixed) because their values cannot be predicted from first principles or are uncertain due to observational limitations. The number of free parameters in each SAM varies based on the complexity of the physics implemented. For instance, Croton et al. (2016) includes 14 parameters, while Lagos et al. (2018) uses 40 parameters. Out of those parameters, a fraction of them

are free to change. Free parameters are then constrained by comparing the model predictions with observations of real galaxies. By adjusting the values of the free parameters, semi-analytic models can reproduce a wide range of observed properties of galaxies, such as their luminosity, mass, size, gaseous content, among others. On the other hand, some parameters in SAMs are fixed based on either theoretical considerations or observational constraints. For example, observations of nearby galaxies have shown that the instantaneous recycling fraction is relatively constant and has a value of approximately 0.4, which means that 40% of the mass of dying stars is returned to the interstellar medium in the form of gas. This value is supported by both theoretical models of stellar evolution and observations of the chemical enrichment of galaxies over cosmic time (Cole et al., 2000; Tremonti et al., 2004a). Because the instantaneous recycling fraction is a fundamental property of stellar evolution and is relatively well-constrained by observations, it is typically fixed in semi-analytic models. However, some SAMs may include a dependence of the instantaneous recycling fraction on other parameters, such as the initial mass function of stars, which can introduce some level of flexibility in the modeling. The values of fixed parameters in semi-analytic models are not necessarily well-known, and there may be significant uncertainties associated with them. However, they are typically chosen based on the best available theoretical and observational constraints, and are often varied in sensitivity analyses to test the robustness of the model predictions. Additionally, as new observational data become available, the values of fixed parameters may be updated or revised in order to improve the accuracy of the model predictions.

To calibrate DARK SAGE, Stevens et al. (2016) use a visual inspection of how well the model represents a set of empirical relations. This means that we tweak the free parameters by hand, run the simulation, and assess visually how well the model traces the selected observations. Most SAMs are calibrated to follow the stellar mass function at $z = 0$ (Baldry et al., 2008; Baldry et al., 2012; D'Souza et al., 2015). Some SAMs are tuned to match the local luminosity function (Benson, 2010). The trick to calibrate a SAM involves tweaking free parameters included in some physical prescriptions. DARK SAGE is calibrated using the stellar mass function (Baldry et al., 2008), H I (Zwaan et al., 2005) and H2 mass functions (Keres et al., 2003), the H I–stellar mass scaling relation (Brown et al., 2015), the black hole–bulge mass relation (Scott et al., 2013), the Baryonic Tully–Fisher relation (Stark et al., 2009), the galaxy mass–metallicity relation (Tremonti et al., 2004b), and the mean cosmic star formation density–redshift relation (Somerville et al., 2001). Modern SAMs use sophisticated techniques to calibrate their models such as the Monte Carlo Markov Chain algorithms (Henriques et al., 2020), self-learning methods using Particle Swarm Optimisation (Ruiz et al., 2015) or Bayesian methods (Bower et al., 2010). More information on SAM calibration and comparisons, see Knebe et al. (2015).

CHAPTER 3

Paper 1 - Angular momentum and Morphological Sequence of Massive Galaxies through DARK SAGE

Motivation

Before the 1990s, simulations had a longstanding problem, where galaxies were too small, bulgy, and deficient of angular momentum (Steinmetz & Navarro, 1999). It was not until recently that numerical simulations acquired advanced physical prescriptions involving feedback and improved particle resolution, which allowed galaxies to evolve disks as flat as our Milky Way's while preserving high angular momentum. Since then, angular momentum has emerged as a more fundamental parameter to classify galaxy morphologies than the classical Hubble sequence, which breaks down at high redshift. Although there is uncertainty in the treatments of feedback that solve the angular momentum problem, the relationship between angular momentum and morphology has grown a strong bridge between theory and observations. Using the semi-analytic model DARK SAGE, we are studying the predicted relationship between dark matter spin, stellar spin, and galaxy morphology at z=0.

Abstract

We study the present-day connection between galaxy morphology and angular momentum using the DARK SAGE semi-analytic model of galaxy formation. For a given stellar mass in the range 10^{10}–$10^{12}\,M_{\odot}$, the model predicts that galaxies with more prominent disks exhibit higher *stellar* disk specific angular momentum ($j_{\rm stellar,disk}$). However, when we include the gas in the disk, bulge-dominated galaxies have the highest *total* disk specific angular momentum ($j_{\rm total,disk}$). We attribute this to a large contribution from an extended disk of cold gas in typical bulge-dominated galaxies. Note that while the specific angular momenta ($j = J/M$) of these disks are large, their masses (M) are negligible. Thus, the contribution of these disks to the total angular momentum of the galaxy is small. We also find the relationship between the specific angular momentum of the dark matter ($j_{\rm darkmatter}$) and morphology to be counter-intuitive. Surprisingly, in this stellar mass range, not only do bulge-dominated galaxies tend to live in halos with higher $j_{\rm darkmatter}$ than disk-dominated galaxies, but intermediate galaxies (those with roughly equal fractions of bulge and disk mass) have the lowest $j_{\rm darkmatter}$ of all. Yet, when controlling for halo mass, rather than stellar mass, the relationship between $j_{\rm darkmatter}$ and morphology vanishes. Based on these results, we find that halo mass—rather than angular momentum—is the main driver of the predicted morphology sequence in this high mass range. In fact, in our stellar mass range, disk-dominated galaxies live in dark matter halos that are roughly one fifth the mass of their bulge-dominated counterparts.

3.1 Introduction

For decades, the standard model of cosmology, ΛCDM, which assumes a flat Universe dominated by cold dark matter with a cosmological constant, has greatly contributed to our understanding of galaxy formation (Cen & Ostriker, 1994, 1999b,a; Serna et al., 2003; Grande et al., 2008; Hopkins et al., 2009b). It is widely understood that dark matter halos formed from density perturbations in the early Universe, which subsequently acquired angular momentum through tidal torques from neighboring perturbations (see Field & Shepley, 1968; Peebles, 1969; Harrison, 1971). In a simplistic galaxy formation framework, angular momentum is assumed to be conserved as baryons dissipate energy and quickly collapse into a rotationally supported disk, but the details of how galaxies form, grow, and acquire angular momentum are far from complete. Observationally, there is a clear link between the stellar specific angular momentum, $j_{\rm stellar}$, and the stellar mass of a galaxy, where $j_{\rm stellar} M_*^{2/3}$. This relation also carries a well-known dependence on galaxy morphology, where disk-dominated spiral galaxies have higher $j_{\rm stellar}$ than bulge-dominated elliptical galaxies of the same stellar mass (Fall, 1983; Romanowsky & Fall, 2012; Fall & Romanowsky, 2013; Obreschkow & Glazebrook, 2014; Fall & Romanowsky, 2018). The angular momentum versus stellar mass relation for galaxies of different morphologies is often referred to as the Fall relation.

There are two techniques for modeling the angular momentum–galaxy connection in a cosmological context: *semi-analytic models* (SAMs), which use analytic halo histories or halo merger trees from an N-body cosmological simulation and populate the galaxies as a post-processing step, and *hydrodynamic simulations*, which evolve baryons and dark matter together, but at much higher computational expense. A key assumption of most semi-analytic models is that the baryonic specific angular momentum is equal to that of the dark matter, acquired through tidal torques (White & Frenk, 1991; Cole et al., 1994; Bower et al., 2006; Somerville et al., 2008; Ricciardelli & Franceschini, 2010; Benson, 2012; Croton et al., 2016). As a result of this strong coupling, SAMs tend to produce elliptical galaxies in halos with low angular momentum (Avila-Reese & Firmani, 1999; Kauffmann et al., 1999; Hatton et al., 2003; Tonini et al., 2016). However, cosmological hydrodynamic simulations have revealed that the specific angular momentum of baryons can differ from their host dark matter halo by a factor of 2–5 (Sharma & Steinmetz, 2005; Sales et al., 2010; Kimm et al., 2011; Pichon et al., 2011; Stevens et al., 2017; Zjupa & Springel, 2017). One explanation of this discrepancy is that gas-rich mergers and cold-flow streams spiral through the galaxy halo prior to falling into the galaxy disk, producing a cool gas disk with high angular momentum (Stewart et al., 2011).

Naturally, both semi-analytic and hydrodynamic techniques aspire to be consistent with observations. Several semi-analytic models have successfully recreated the Fall relation (e.g. Stevens et al., 2016, 2018; Zoldan et al., 2018, 2019; Irodotou et al., 2019; Marshall et al., 2019), while others overestimate the total

stellar specific angular momentum of disk-dominated galaxies (Mitchell et al., 2018). As shown by Stevens et al. (2016), the SAGE model (Croton et al., 2016) produces disk-dominated galaxies that overlap observational data from Fall & Romanowsky (2013) and Obreschkow & Glazebrook (2014). Although many semi-analytic models agree with observations, most—like SAGE—assume $j_{\rm stellar}$ to be equal to $j_{\rm darkmatter}$. One model that does not make this simple assumption is DARK SAGE (Stevens et al., 2016). Instead, DARK SAGE numerically evolves each galaxy's disk structure, meaning $j_{\rm stellar}$ is a more physically motivated quantity that is unique to a given galaxy's history. Stevens et al. (2016) show that DARK SAGE is able to produce the Fall relation for disky galaxies with bulge-to-total stellar mass ratios ($B/T = 1-D/T$) less than 0.3. However, they did not explore this relation for galaxies with a significant bulge component. It is important to note that DARK SAGE does not calculate the angular momentum of bulges formed through mergers, and is thus not able to make accurate predictions for the total angular momentum of bulge-dominated galaxies. In this work, we do place some reasonable limits on the bulge angular momenta in galaxies to compare with observations. However, our main focus is to study the *disk* angular momentum for the entire range of morphological types, as predicted by DARK SAGE.

Beyond merely extending the work of Stevens et al. (2016) to study stellar disks over the entire range of D/T, we seek to take advantage of the sophisticated treatment of angular momentum in DARK SAGE to dissect its connection to galaxy morphology in greater detail. Specifically, we explore how disk size and velocity are connected to morphology, and we investigate the connection between galaxy morphology and the angular momentum of dark matter and gas, as well.

This paper is organized as follows. In Section 3.2, we present an overview of the DARK SAGE semi-analytic model and its observational constraints, describe our galaxy sample, and outline our galaxy morphology definition. In section 3.3, we examine DARK SAGE predictions of $j_{\rm stellar,disk}$ and $j_{\rm total,disk}$. Section 3.4 explores the $j_{\rm darkmatter}$ as a function of stellar mass. Section 4.6 presents our conclusions and discusses these results.

3.2 Semi-analytic Model: DARK SAGE

DARK SAGE is a model that uses coupled physical and phenomenological analytic expressions to describe the various processes in galaxy formation, leading to predictions of galaxy properties that can be compared to observations (Stevens et al., 2016). Similar to Croton et al. (2016), DARK SAGE halos contain hot gas reservoirs necessary to form and grow galaxies through radiative cooling and condensation (White & Rees, 1978). The hot gas, assumed to be an isothermal sphere (White & Frenk, 1991), cools at a similar rate prescribed in Croton et al. (2016) and gravitationally collapses to form a galactic disk. Subsequent cooling episodes, however, see some angular momentum lost before reaching the disk, as the baryonic and dark

matter angular momenta are allowed to decouple. The baryonic angular momentum at any given time is non-trivially determined, as it depends on the galaxy's entire history. This is affected not only by changes to its halo properties, but also by feedback from star formation and active galactic nuclei, as well as mergers. Although the baryonic angular momentum encodes the galaxy's history, its contribution to its total halo angular momentum is small, meaning the total halo angular momentum is assumed to be unaffected by internal processes.

DARK SAGE distinguishes itself from other semi-analytic models by also self-consistently evolving the radial structure of galaxy disks. DARK SAGE breaks disks into 30 logarithmically-spaced bins of specific angular momentum. Every disk has two sets of annuli: one responsible for stars and one responsible for gas.

After every cooling episode and merger, DARK SAGE uses the Toomre Q parameter to check stability for each annulus. Internal disk instabilities play an important role in the process of building bulge material (see e.g. Efstathiou et al., 1982; Croton et al., 2006; De Lucia et al., 2011; Guo et al., 2011; Henriques et al., 2015) and in star formation in general (Stevens & Brown, 2017). Bulges are built from a combination of secular processes and mergers (Weinzirl et al., 2009). Here, DARK SAGE allows for matter exchange between annuli from Toomre instabilities, funneling low angular momentum material to the center to grow the bulge component. Stevens et al. (2016) note that by examining $D/T > 0.7$ galaxies with stable disks, those galaxies naturally follow the observed Fall relation, showing that the physics considered in DARK SAGE naturally explains observations. One of our goals is to extend this study to galaxies with $D/T < 0.7$.

Just like any semi-analytic model, DARK SAGE uses prescriptions that include free parameters whose values are obtained by calibrating the model. DARK SAGE only allows eight free parameters to vary during the calibration process. The calibration is done by hand using a set of observational constraints, including the stellar mass function (Baldry et al., 2008), H I (Zwaan et al., 2005) and H2 mass functions (Keres et al., 2003), the H I–stellar mass scaling relation (Brown et al., 2015), the black hole–bulge mass relation (Scott et al., 2013), the Baryonic Tully–Fisher relation (Stark et al., 2009), the galaxy mass–metallicity relation (Tremonti et al., 2004b), and the mean cosmic star formation density–redshift relation (Somerville et al., 2001). See appendix A of Stevens et al. (2016) for further details.

Beyond these statistics that DARK SAGE is explicitly calibrated to match, the model produces predictions that can be tested against current and future observations; physically informative models will successfully produce a wide suite of observables for which they were not tuned. For example, DARK SAGE reproduces realistic surface density profiles of stars, H I, and H_2 for disk-dominated galaxies (Stevens et al., 2016). The model also successfully predicts the stellar specific angular momentum–stellar mass sequence for disk-dominated galaxies. However, DARK SAGE has some shortcomings. For example, the model does not consider bars, which could affect the internal physical properties of disks. Moreover, the stellar half-mass

radii of disk-dominated galaxies in DARK SAGE are systematically 0.1 dex lower than the half-light radii of galaxies in the GAMA survey (Stevens, 2016). Pinpointing the ways in which a semi-analytic model succeeds and fails to reproduce observations can map out the fidelity of the prescriptions used to govern the physics of galaxy evolution.

To conduct our study, we use the Theoretical Astrophysical Observatory[1] (TAO) (Bernyk et al., 2016) to construct our data sample. This version of DARK SAGE is built on merger trees from the Millennium simulation (Springel et al., 2005). The Millennium simulation uses a periodic box with $500\,h^{-1}$ Mpc in length, allowing us to sample about 10^6 galaxies in this paper (see Section 3.2.1). It uses cosmological parameters from the Wilkinson Microwave Anisotropy Probe data (Spergel et al., 2003) with $\Omega_m = 0.25$, $\Omega_\Lambda = 0.75$, $\Omega_b = 0.045$, $\sigma_8 = 0.9$, and $h = 0.73$. The simulation evolves the dark matter distribution with GADGET-2 (Springel, 2005) adopting a particle mass of $8.6 \times 10^8\,h^{-1}\,\mathrm{M}_\odot$. The merger trees are constructed with L-HALOTREE (Springel, 2005) and the halos and subhalos are found using FOF and SUBFIND (Springel et al., 2001), which also provides the specific angular momentum of each halo. We adopt a minimum halo mass of $10^{11.2}\,\mathrm{M}_\odot$, which corresponds to about 200 particles. It is important to note that DARK SAGE refers to all "halo" quantities as the sum over all matter within the halo. However, because dark matter dominates in mass, the angular momentum of the halo is similar to that of the dark matter. For the purposes of this paper, the dark matter, halo, and total j are treated the same.

For a more detailed description of the version of DARK SAGE used in this paper, please refer to Stevens et al. (2016). We note that later versions of the model have since been published (e.g. Stevens et al., 2018), and the model is under constant development. For practical reasons and ease of reproducibility, we adopted the 2016 version of the model, as it is the only one readily available on TAO. As updates to DARK SAGE are incremental, we would not expect significant changes to the results and conclusions of this paper were we to change the version of the model.

3.2.1 Galaxy sample

Our goal is to examine $j_{\mathrm{stellar,disk}}$, $j_{\mathrm{total,disk}}$, and $j_{\mathrm{darkmatter}}$ as a function of stellar mass and galaxy morphology. Only central galaxies are part of our study, as the angular momenta of satellites' subhalos in N-body simulations are subject to environmental effects and numerical decisions that are out of scope here. As we mention above, we adopt a halo mass threshold of $10^{11.2}\,\mathrm{M}_\odot$, requiring that every halo with a galaxy has at least 200 particles. Although we are missing some galaxies with stellar masses greater than $10^{10}\,\mathrm{M}_\odot$ in low-mass halos, our threshold ensures we are at least 84% complete in halo mass for any stellar mass. Given that the main results of this paper pertain to connecting galaxy properties with halo properties, it is important that we

[1] https://tao.asvo.org.au/tao/

ensure completeness in terms of halo mass for the stellar mass range we assess. For this reason, we maintain a more conservative sample than Stevens et al. (2016). To illustrate our data selection, Figure 3.1 shows the stellar-to-halo mass relation for DARK SAGE galaxies. The violet line represents the median of data binned by halo mass, where all bins include at least 30 galaxies. The dark and light shaded regions enclose the inner 68 and 95 percent of the data, respectively. For comparison, we also show results from several empirical models. Specifically, the blue solid line shows the Behroozi et al. (2010) model, in which the stellar mass scales as $M_h^{2.3}$ for halo masses between 10^{11}–$10^{12}\,\mathrm{M}_\odot$, and as $M_h^{0.3}$ for halo masses greater than $10^{14}\,\mathrm{M}_\odot$ at redshift 0. The yellow and orange solid lines show the Behroozi et al. (2019) and Kravtsov et al. (2018) models, respectively. The yellow dashed lines show the one-sigma scatter from Behroozi et al. (2019). The grey vertical line shows our halo mass threshold, and the grey horizontal line at $10^{10}\,\mathrm{M}_\odot$ denotes the stellar mass cut used to conduct our study. The plot shows that the galaxies in our sample live in well-resolved halos. Our sample totals 964,793 semi-analytic galaxies. Overall, the DARK SAGE stellar mass–halo mass relation exhibits reasonable qualitative agreement with results from Behroozi et al. (2010, 2019) and Kravtsov et al. (2018). However, there are some notable differences, including a slightly different location for the 'knee' of the relation and a significantly different scatter. At halo masses below $10^{11.2}\,\mathrm{M}_\odot$, DARK SAGE galaxies have higher stellar masses than the other relations, but we note that these are the galaxies that live in less-resolved halos. At halo masses above $10^{11.2}\,\mathrm{M}_\odot$, DARK SAGE most closely tracks the Behroozi et al. (2019) relation. An expanded analysis of the stellar mass–halo mass relation in DARK SAGE is left for a future paper.

3.2.2 Defining galaxy morphology

It is common in observational studies to use luminosity or surface brightness profiles to define galaxy morphology (de Vaucouleurs, 1953; Roberts, 1994; Blanton et al., 2003; Driver et al., 2006; Moffett et al., 2016). Kauffmann et al. (2003) found that massive elliptical galaxies experience high surface mass densities, which usually carry old stellar populations. On the other hand, low-mass galaxies have low surface mass densities, which typically translate to disks commonly containing young stellar populations.

Semi-analytic models have *a priori* distinction between disks, bulges, and other baryonic reservoirs. It is therefore standard to quantify morphology through the disk-to-total (or equally the bulge-to-total) stellar mass ratio of a semi-analytic galaxy. In our study, galaxy morphology is based on the ratio of disk-to-total stellar mass D/T, where the total stellar mass is defined as the sum of the disk and bulge stellar mass components. DARK SAGE treats bulge formation through multiple channels; the bulge component is divided into merger-driven, instability-driven, and pseudobulge components. We treat the pseudobulge as part of the disk (see Stevens et al., 2016), so the sum of the first two make up the total bulge mass. Figure 3.2 shows the normalized distribution of this ratio for our galaxy sample. We divide our sample into three morphological

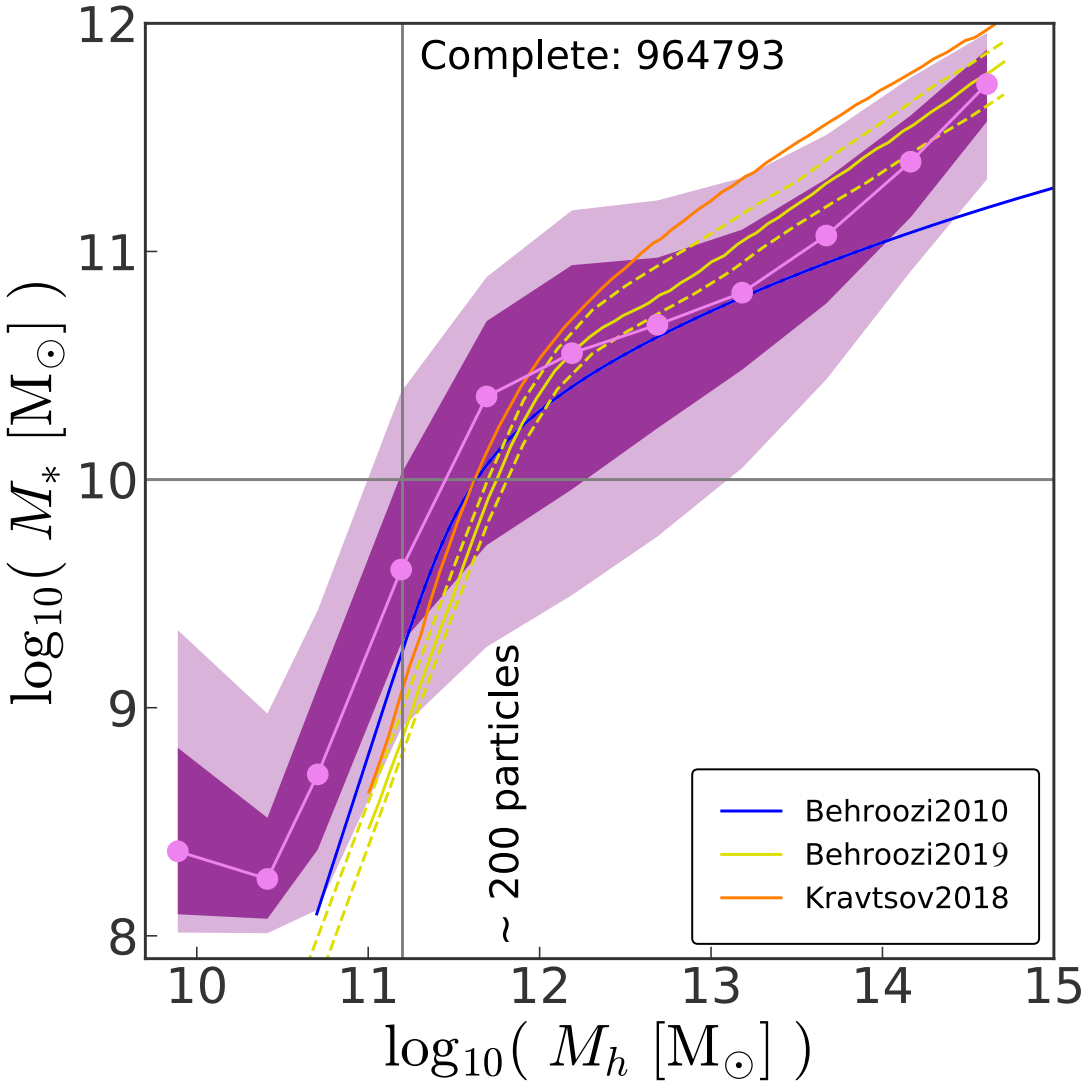

Figure 3.1: The stellar-to-halo mass relation for central galaxies in DARK SAGE at $z = 0$. The violet line connecting the dots shows the median binned by halo mass. The dark and light shaded regions enclose 68 and 95 percent of the data, respectively. The blue, yellow, and red solid lines come from the empirical models of Behroozi et al. (2010, 2019) and Kravtsov et al. (2018). The yellow dashed lines show the one-sigma scatter from Behroozi et al. (2019). The grey vertical line at $10^{11.2}\,\mathrm{M}_\odot$ denotes our halo mass threshold, while the grey horizontal line at $10^{10}\,\mathrm{M}_\odot$ denotes the stellar mass cut used to conduct our study. Our complete sample contains 964,793 model galaxies.

types, based on the D/T ratio. Galaxies with $D/T > 0.58$ are defined as the disk-dominated population, containing 498,869 galaxies (Region c of Figure 3.2). Galaxies with D/T between 0.1 and 0.58 are an intermediate population, containing 352,129 galaxies (Region b), and galaxies with D/T less than 0.1 are spheroidal (hereafter 'bulge-dominated'), containing 113,795 galaxies (Region a). This stellar morphology distribution looks similar to that measured in the Sloan Digital Sky Survey (Bluck et al., 2014), in that both exhibit a large narrow peak for massive galaxies with D/T less than 0.1, although our morphology distribution does not show a peak of pure disks.

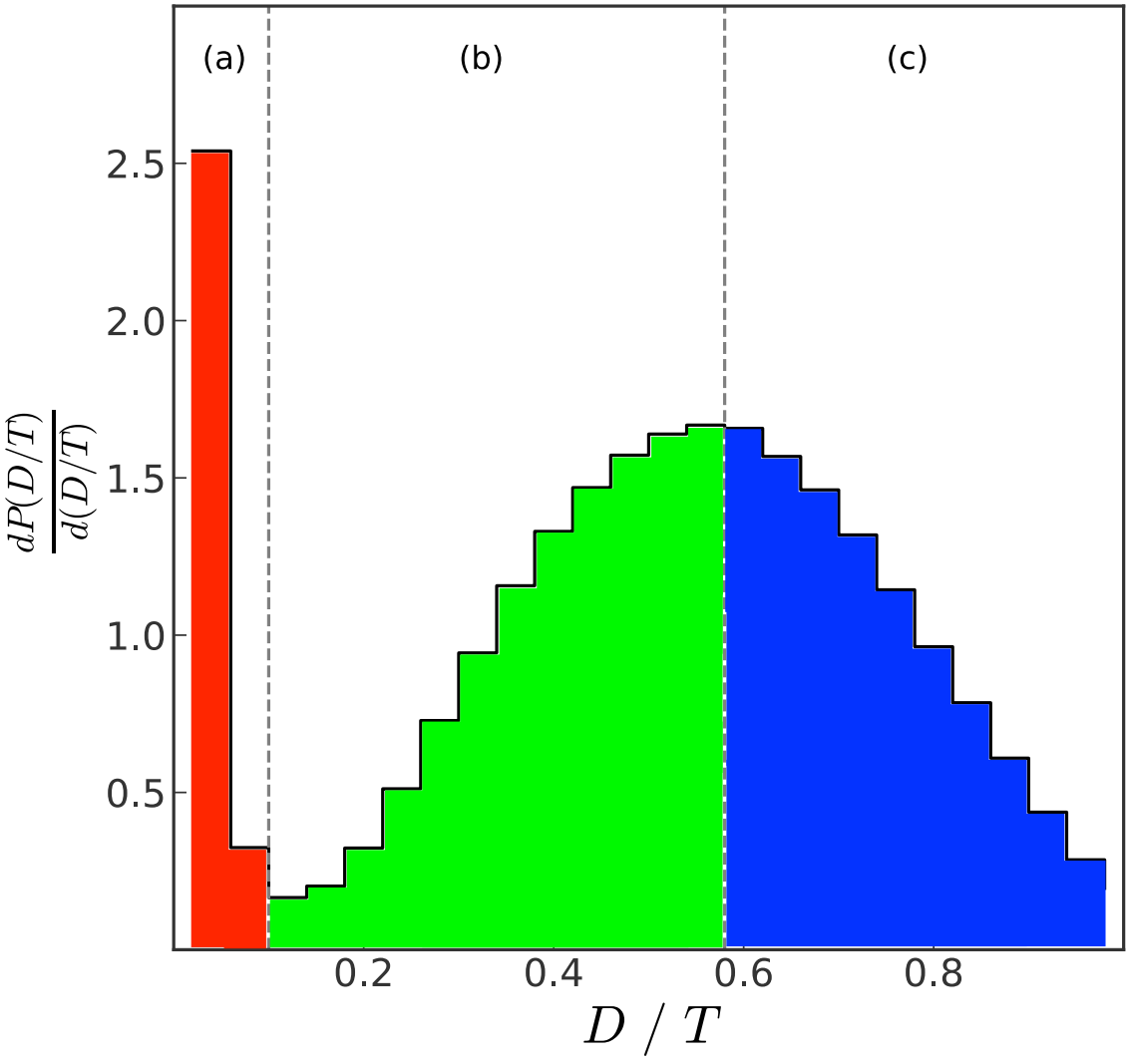

Figure 3.2: Distribution of disk-to-total stellar mass ratio within our galaxy sample at $z=0$. The vertical black dashed lines denote our morphology cuts. Galaxies with a D/T less than 0.1 are bulge-dominated, containing 113,795 galaxies (Region a; red); galaxies between 0.1 and 0.58 are the intermediate population, containing 352,129 galaxies (Region b; green); and galaxies with a D/T greater than 0.58 are disk-dominated, containing 498,869 galaxies (Region c; blue).

3.2.3 Bulge composition

There is evidence from both observations (Matteucci & Brocato, 1990; Kormendy, 1993; Rich, 1996) and simulations (Efstathiou et al., 1982; Noguchi, 1999) that bulges can grow through multiple channels, leading to variations in both their spatial structure and kinematic behavior. DARK SAGE explicitly tracks two bulge components in each galaxy: the *instability-driven* and *merger-driven bulge*, each with its own evolutionary path. The *instability-driven bulge* grows from the Toomre-unstable stars in the innermost disk annulus, but typically, when there is an unstable annulus farther out in the disk, the unstable stars cascade all the way into the center (see section 3.7 of Stevens et al. 2016 for further details).

The *merger-driven bulge* grows through both major and minor mergers of galaxies. When a major merger occurs, the stellar bulges and disks of both galaxies are added to the newly formed *merger-driven bulge*. The angular momentum vectors of the gas disks from the two galaxies are summed and projected onto the new disk plane, across which a starburst is triggered.

The stars formed through a merger-driven starburst are added into the *merger-driven bulge*, while a fraction of the gas from the star-bursting annuli also feeds the supermassive black hole. The framework used in DARK SAGE for these processes is an extension of Kauffmann & Haehnelt (2000); Somerville et al. (2001) (see section 3.9 of Stevens et al. 2016 for more details).

For minor mergers, the satellite stellar bulge and disk is added into the host's *merger-driven bulge*. The satellite's cold gas is deposited into the central's annuli whose angular momentum overlaps with that of the satellite's orbital angular momentum immediately prior to merging. These annuli exclusively then experience a starburst. As in major mergers, a fraction of the gas flows into the black hole, and the new stars join the *merger-driven bulge* of the host (see section 3.9 of Stevens et al. (2016) for more details).

DARK SAGE galaxies also include rotationally supported 'pseudobulges', but these are implicitly part of the disk. A galaxy can be identified as hosting a pseudobulge when the disk surface density profile is notably steeper than an exponential towards its centre. See section 4.1 of Stevens et al. (2016) for further details.

Figure 3.3 shows the fractions of merger-driven (red) and instability-driven (blue) mass over the total bulge mass within the stellar mass ranges of 10^{10}–10^{11} and 10^{11}–$10^{12}\,\mathrm{M}_{\odot}$ for bulge-dominated (Region a), intermediate (Region b), and disk-dominated galaxies (Region c). DARK SAGE predicts that mergers contribute 99.9% of the mass of the bulge in bulge-dominated galaxies (Region a). For both intermediate and disk-dominated galaxies, the instability-driven bulges are most massive, accounting for 70–80% and 40–60% of the total bulge mass, respectively.

To explore what contributes to the bulge build-up, we also looked at the time of last major merger for all galaxies. We find that 80% of bulge-dominated galaxies in our sample had at least one major merger in the

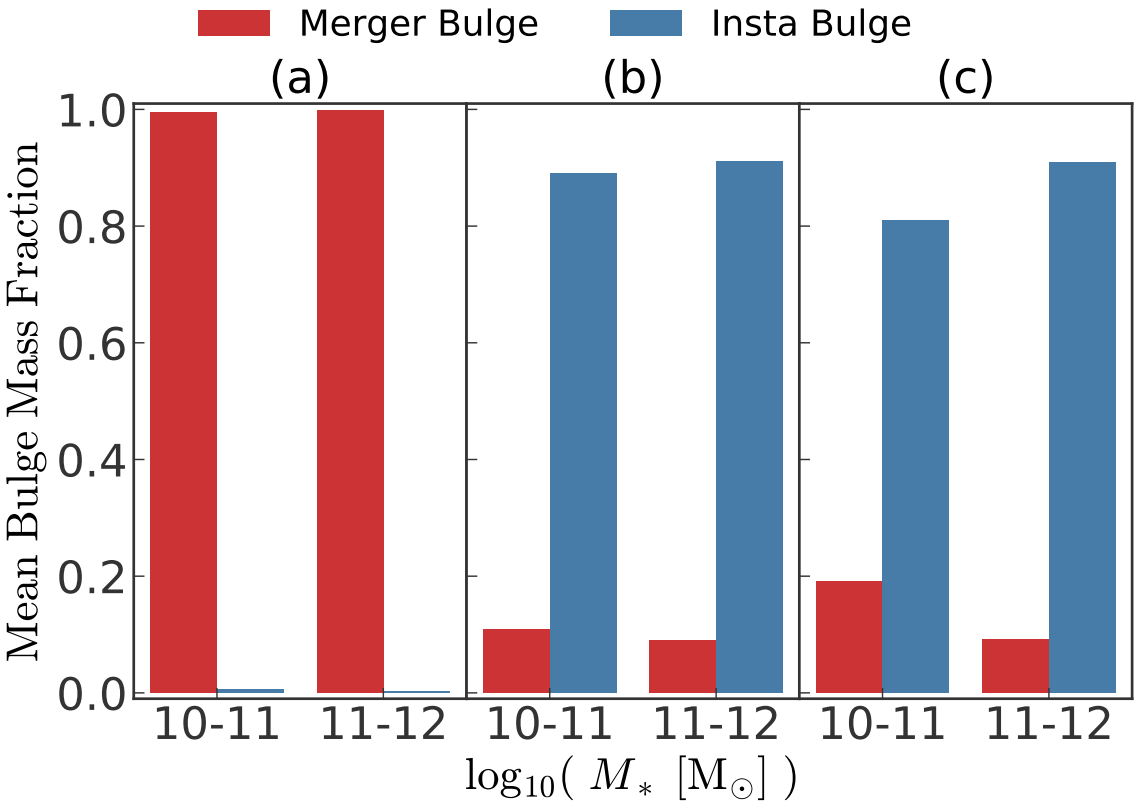

Figure 3.3: Fraction of merger-driven (red) and instability-driven (blue) mass over the total bulge mass within the stellar ranges of 10^{10}–10^{11} and 10^{11}–$10^{12}\,M_{\odot}$ for bulge-dominated (region a), intermediate (region b), and disk-dominated galaxies (region c). Most of the mass in the bulge for bulge-dominated galaxies comes from mergers. For intermediate and disk-dominated galaxies, the instability-driven bulge contributes the most to the bulge masses.

last 5.5 Gyr. In contrast, about 80% of intermediate and disk-dominated galaxies did not experience a major merger, and of those that had major mergers, 20% percent had their most recent merger more than 5.5 Gyr ago. Other studies suggest that, after a major merger, the angular momentum of every component of a galaxy can change significantly (Bekki, 1998; Cox et al., 2006; Lotz et al., 2010; Moreno et al., 2015; Sparre & Springel, 2016). Much of this change depends on the gas fraction of the merging galaxies. If the smaller merging galaxy has no gas, then any gas disk in the larger system will persist relatively unimpeded (Lagos et al., 2018). For a merger of gas-rich galaxies, most of the gas is consumed in the starburst and by black hole accretion. Minor mergers will also disrupt the structure of the gas disk, causing star formation in various parts of the disk, which could alter $j_{\mathrm{stellar,disk}}$. In the case of DARK SAGE, all the stars end up in the merger-driven bulge, and the stellar disk has to regrow from the remains of the post-starburst gas disk and future accretion episodes. In essence, a large number of mergers can translate to a diversity of angular momentum.

However, DARK SAGE does not explicitly track the angular momenta of bulges. In principle, the merger-driven bulge has angular momentum, but it is not calculated and is treated as zero for all galaxies. This is a valid approximation for galaxies with merger-driven bulge masses that constitute a small fraction of the total bulge mass (i.e. intermediate and disk-dominated galaxies according to Figure 3.3). This is not a good approximation for galaxies with significant merger-driven bulge masses. Thus, bulge-dominated galaxies may be missing a great deal of angular momentum from the merger-driven bulge that is not taken into account. The instability-driven bulge, by definition, has no angular momentum, since it is composed exclusively of stars on random orbits that lost all their angular momentum to other parts of the disk. In other words, for intermediate and disk-dominated galaxies, the disk stellar angular momentum $J_{\mathrm{stellar,disk}}$ is approximately the same as the total stellar angular momentum $J_{\mathrm{stellar,gal}}$.

This is an important caveat given that observations typically include the bulge component when measuring the stellar specific angular momentum. For example, Romanowsky & Fall (2012) and Fall & Romanowsky (2013) include the stellar angular momentum of the bulge in their j_{stellar} measurements. In the cases of Posti et al. (2018) and Sweet et al. (2018), non-circular motions are neglected, but the bulge mass is included in their total stellar mass, which is used to calculate the stellar specific angular momentum of the galaxy. To make a comparison with observations in this paper, we explore some conservative limits on the bulge angular momentum, but for most of this paper we focus on the angular momentum of the disk, rather than the whole galaxy.

3.2.4 Calculating angular momentum

DARK SAGE calculates the total angular momentum inside a disk annulus as:

$$J_{\rm annulus} = m_{\rm annulus} * 0.5 * (j_{\rm inner} + j_{\rm outer}), \tag{3.1}$$

where $m_{\rm annulus}$ is the mass inside the annulus and $j_{\rm inner}$ and $j_{\rm outer}$ are the specific angular momenta of the inner and outer boundaries of the annulus, respectively. The sum over the total number of annuli (30 in our case) gives the total angular momentum of the disk. Then, the specific angular momentum is obtained by dividing this by the total mass of all annuli.

We define $j_{\rm total,disk}$ as the combined specific angular momentum of a galaxy's cold gas and stellar disk. In DARK SAGE, the 'cold gas' mass includes atomic hydrogen (H I), molecular hydrogen (H_2), helium, metals, and some residual ionized gas.

The specific angular momentum of the dark matter comes directly from the Millennium simulation, which accounts for all particles inside R_{200}.

3.3 Connecting the stellar and total disk specific angular momentum

To dissect the anatomy of our galaxy morphology sequence, in Figure 3.4, we break down the angular momentum contribution of the stellar and cold gas disk components. Figure 3.4 illustrates the ratio of $j_{\rm coldgas,disk}$ (blue) and $j_{\rm stellar,disk}$ (orange) over $j_{\rm darkmatter}$ within the stellar mass ranges of 10^{10}–10^{11} and 10^{11}–$10^{12}\,{\rm M}_{\odot}$ for bulge-dominated (panel a), intermediate (panel b), and disk-dominated galaxies (panel c).

Figure 3.4 shows that, for bulge-dominated galaxies in our model, the dark matter component has the highest specific angular momentum, followed by cold gas, with the stellar disk coming in last. The dominance of $j_{\rm darkmatter}$ is strongest for galaxies with higher overall stellar mass. In contrast, for intermediate and disk-dominated galaxies, the cold gas disk generally has the highest specific angular momentum, with dark matter coming next, and the stellar disk coming in last. We do not see a strong trend of these results with stellar mass. Because we consider $j_{\rm darkmatter}$ as the total angular momentum, we get a clearer idea of the contribution of $j_{\rm coldgas,disk}$ and $j_{\rm stellar,disk}$ at different morphologies.

$j_{\rm stellar,disk}$ has a strong correlation with stellar mass and morphology. In Figure 3.5 we examine this relation in DARK SAGE and compare to observations. As we discussed in the previous section, DARK SAGE does not calculate the angular momentum of the bulge component of galaxies; it only calculates the stellar disk component, $j_{\rm stellar,disk}$. However, observational measurements of angular momentum typically capture the total stellar angular momentum, $j_{\rm stellar,gal}$. In order to have an apples-to-apples comparison, we adopt two limiting cases for the bulge angular momentum of DARK SAGE, which we show in the two panels of

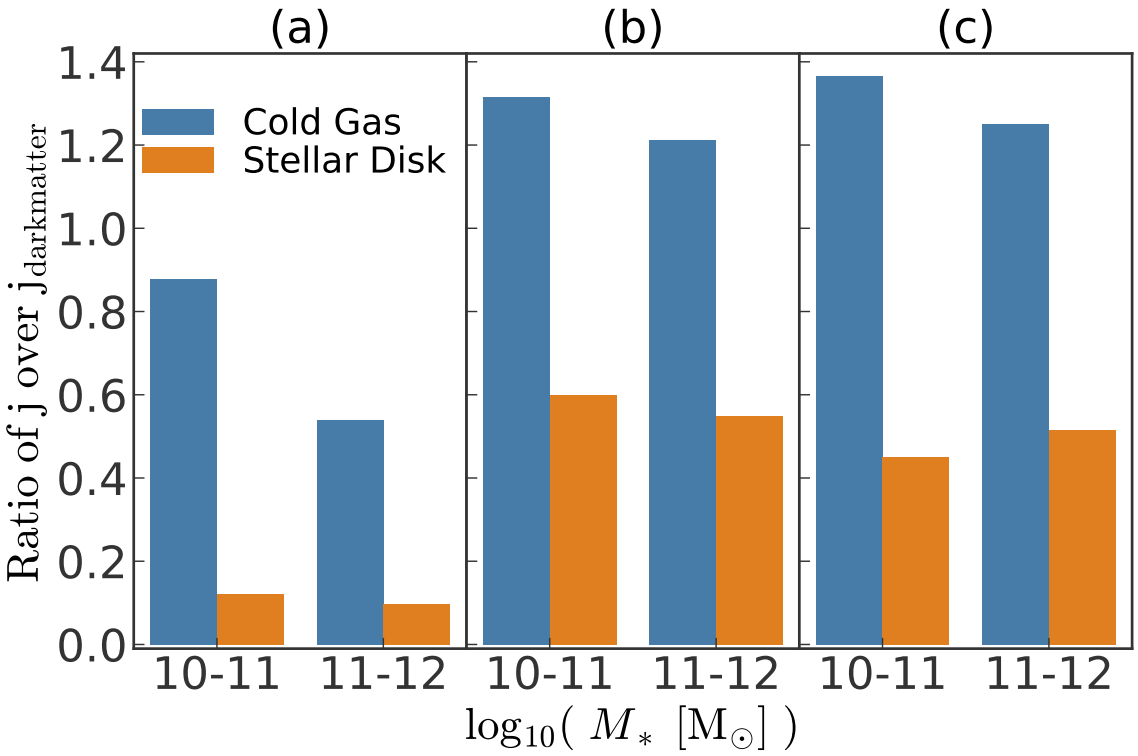

Figure 3.4: From left to right: the ratio of $j_{\mathrm{coldgas,disk}}$ (blue) and $j_{\mathrm{stellar,disk}}$ (orange) over $j_{\mathrm{darkmatter}}$ within the stellar mass ranges of 10^{10}–10^{11} and 10^{11}–$10^{12}\,\mathrm{M}_\odot$ for bulge-dominated (panel a), intermediate (panel b), and disk-dominated galaxies (panel c). For all galaxies, the cold gas component has more specific angular momentum than the stellar component. Intermediate and disk-dominated galaxies have higher $j_{\mathrm{coldgas,disk}}$ than $j_{\mathrm{darkmatter}}$. Bulge-dominated galaxies have the least $j_{\mathrm{stellar,disk}}$.

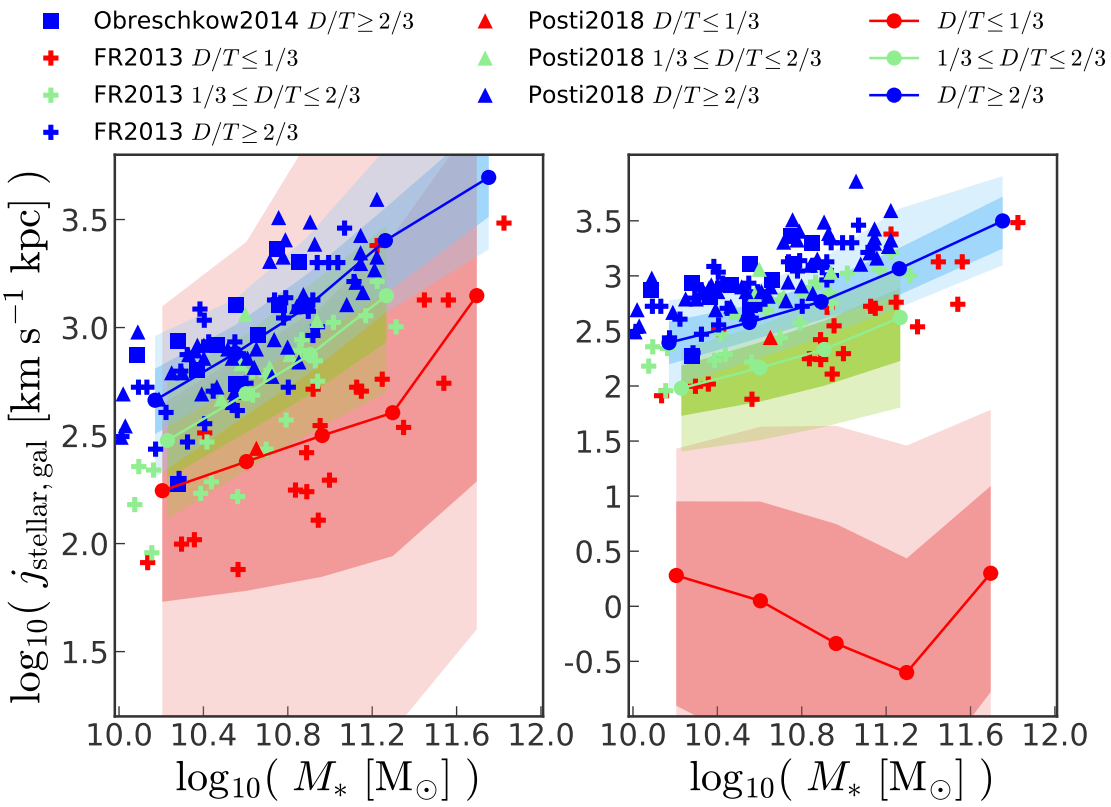

Figure 3.5: Stellar specific angular momentum as a function of stellar mass for bulge-dominated (red), intermediate (green) and disk-dominated (blue) galaxies. Panels show limiting cases of the DARK SAGE model where the bulge specific angular momentum, which the model does not calculate, is set to be equal to either that of the stellar disk (upper limit; left panel) or zero (lower limit; right panel). Solid lines show the median within stellar mass bins of width 0.4 dex, while dark and light shaded regions enclose the inner 68 and 95 percent of the data for the respective distributions. Squares, crosses, and triangles show measurements of observed galaxies from Obreschkow & Glazebrook (2014); Fall & Romanowsky (2013, 2018); Posti et al. (2018) and are the same in both panels. The legend above the panels lists the studies from which the points are taken, along with the disk-to-total fractions, D/T, that correspond to each set of points. DARK SAGE reproduces the observed relationship between $j_{\rm stellar,gal}$, stellar mass and morphological type, but only in the upper limit case where each galaxy's stellar bulge contains as much specific angular momentum as its disk.

Figure 3.5. In the left panel we set the specific angular momentum of each galaxy bulge to be equal to the specific angular momentum of its stellar disk. In this case, $j_{\rm stellar,gal} = j_{\rm stellar,disk}$. This is an upper limit; in general, one would expect the specific angular momentum of the bulge to be lower than the disk. In the right-hand panel we set the specific angular momentum of each galaxy bulge to zero. In this lower-limit case, $j_{\rm stellar,gal} = j_{\rm stellar,disk} \times (D/T)$. The two panels show $j_{\rm stellar,gal}$ as a function of total stellar mass for bulge-dominated (red), intermediate (green), and disk-dominated (blue) galaxies. The solid lines connecting the dots show the running medians for DARK SAGE galaxies binned by stellar mass. The dark and light shaded regions enclose 68 and 95 percent of the data from their respective distributions.

The squares, crosses, and triangles in Figure 3.5 show observational measurements (Fall & Romanowsky, 2013, 2018; Obreschkow & Glazebrook, 2014; Posti et al., 2018) and are exactly the same in both panels. It should be noted that the observational studies use different bulge and disk decomposition methods, concentrate on different morphological cuts, and span different mass ranges to define their samples. For example, Obreschkow & Glazebrook (2014) spans a stellar mass range of $10^{9.1}$–$10^{10.9}\,{\rm M}_{\odot}$ with a narrow D/T range of $2/3 \leq D/T \leq 1$, where they assume a universal mass-to-light ratio of 0.5. Fall & Romanowsky (2013) use a variable mass-to-light ratio for the bulge and disk components. This is important to mention given that distinct mass-to-light ratios result in different bulge and disk masses. This sample covers a stellar mass range of $10^{8.9}$–$10^{11.8}\,{\rm M}_{\odot}$ and a range of D/T between 0 and 1. Fall & Romanowsky (2013) and Posti et al. (2018) use bulge fraction cuts to define disk-dominated ($2/3 \leq D/T \leq 1$), intermediate ($1/3 \leq D/T \leq 2/3$), and bulge-dominated ($0 \leq D/T \leq 1/3$) galaxies. Posti et al. (2018) use observed surface brightness profiles to define an outer disk component. Their galaxy sample covers a stellar mass range of $10^{7.0}$–$10^{11.3}\,{\rm M}_{\odot}$ with mostly low bulge-to-total ratios.

For the purposes of consistency in comparing to observations, for this figure only, we adopted the same D/T cuts in DARK SAGE as in Fall & Romanowsky (2013) and Posti et al. (2018). We note that our results do not change significantly if we use our data-derived morphology cuts shown in Figure 3.2 instead. The only difference we get in changing morphology cuts is in the scatter of the distribution of bulge-dominated galaxies, where galaxies with $D/T < 0.1$ would have a slightly larger scatter in $j_{\rm stellar,disk}$ at low stellar masses. This is related to the transition of bulges being predominantly formed by mergers for galaxies with $D/T < 0.1$ to being predominantly formed by instabilities for higher D/T. We will present an analysis of this scatter in DARK SAGE in future work. We return to our cuts for the remainder of our analysis because they are more natural given the morphology distribution seen in Figure 3.2.

Figure 3.5 shows that the upper-limit case of DARK SAGE (left panel), in which galaxy bulges have as much specific angular momentum as disks, successfully reproduces most of the observational trends for our sample. The median relations of disk, intermediate, and bulge-dominated galaxies predicted by DARK

SAGE go through the middle of the corresponding observational data points. The scatter is also in rough agreement for disk-dominated and intermediate galaxies ($\sim$0.15 dex), though it is significantly larger for bulge-dominated galaxies ($\sim$0.5–0.8 dex).

In the case of disk-dominated galaxies, this comparison is very similar to Stevens et al. (2016) since that paper considered $j_{\rm stellar,disk}$, which is essentially what is shown in the left panel of Figure 3.5. What is striking, however, is that the model works equally well for intermediate and bulge-dominated galaxies even though it represents an upper limit. When we set the bulge angular momentum to zero, which is the lower-limit case shown in the right panel of Figure 3.5, the stellar specific angular momentum of bulge-dominated galaxies is much lower than the observations. Even the disk-dominated and intermediate galaxies have enough of a bulge component pulling them down that they are not as consistent with observations as they are in the left panel.

Though our upper-limit case reproduces the observed Fall relation and its dependence on galaxy morphology, we note that the underlying explanation of the morphological trend is quite different from the interpretation put forth by Fall & Romanowsky (2018). In the left panel of Figure 3.5, stellar disks have specific angular momenta that vary with morphology, with disks in disk-dominated galaxies carrying more specific angular momentum than disks in intermediate or bulge-dominated galaxies. In contrast, Fall & Romanowsky (2018) suggest that all disks are similar (at fixed stellar mass) and all bulges are similar to each other, but have less specific angular momentum than disks, and that the morphological sequence is due to a varying mixture of disk and bulge.

We now focus on better understanding how galaxy disks in DARK SAGE vary as a function of morphology. Disks with high specific angular momentum must have large radii and/or high rotation velocities by definition. We can gain a deeper insight into trends of j with morphology by assessing which (if either) of these two aspects is more important. Figure 3.6 shows the radius, R_{90}, where 90 percent the stellar disk mass is enclosed (right panel) and the rotation velocity, V_{90} (left panel) as a function of stellar mass. For an exponential disk of scale radius R_d with a flat rotation curve, $j_{\rm stellar,disk} = 2R_dV_{90}$ and $R_{90} = 3.89\,R_d$.

From this, even though disks in DARK SAGE are not strictly exponential, we approximate $V_{90} = 1.95\,\frac{j_{\rm stellar,disk}}{R_{90}}$. We find that all three galaxy populations have similar median rotational velocities and overlapping distributions. The scatter of disk velocity for intermediate and disk-dominated galaxies is about 0.05 dex, slightly increasing with stellar mass, while bulge-dominated galaxies have a much larger scatter of 0.2 dex, increasing to about 1.0 dex within our mass range.

When looking at the radius of the disk, we find a morphological sequence in which, at a given stellar mass, disk-dominated galaxies in DARK SAGE have larger disk sizes, followed by intermediate galaxies with intermediate sized disks, and bulge-dominated galaxies, which have the smallest disks. In general, disk-

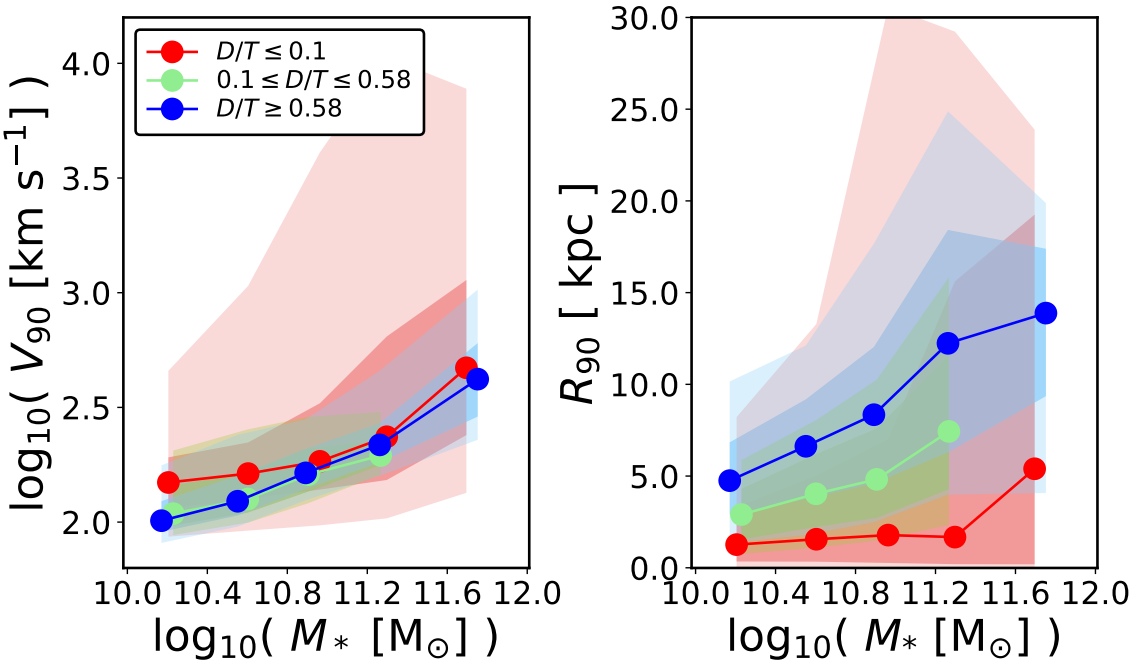

Figure 3.6: Flat rotational velocity (left panel) and disk radius (right panel) as a function of stellar mass, for bulge-dominated (red), intermediate (green) and disk-dominated (blue) galaxies in DARK SAGE. Disk radius here is defined as that enclosing 90% of the stellar disk mass. Bins, lines, and shaded regions are the same as in Figure 3.5. All three galaxy populations have similar rotational velocities, but different average disk radii. Generally, disk-dominated galaxies in our model have disk structures that are about 5–10 times larger than the disk structures in bulge-dominated galaxies. This difference increases with stellar mass.

dominated galaxies in our model have disk radii that are about five to ten times larger than bulge-dominated galaxies. This difference increases with stellar mass. The scatter of R_{90} for disk-dominated and intermediate galaxies is about 2.5 kpc, increasing with stellar mass, while bulge-dominated galaxies have a scatter of 3.5 kpc, increasing to about 10 kpc within our mass range. Note, though, that the scatter—especially for the latter—is not symmetric. Recall that R_{90} only refers to the size of the stellar disk in the galaxy and it does not make any predictions for the size of the bulge structure. Bulge-dominated galaxies within our sample have a large range of disk sizes. The median of the distribution shows that the most massive bulge-dominated galaxies have small R_{90}. Nevertheless, there is a large scatter in the distribution, where a significant number of these also have large disk structures. The large scatter in both the rotational velocity of the disk and R_{90} reflect the large variations in $j_{\rm stellar,disk}$, which non-trivially depends on the host halo's accretion history, spin history, and merger history.

Obreschkow & Glazebrook (2014), Butler et al. (2017), and Wang et al. (2019) investigated baryonic angular momentum, and found a weak empirical correlation between $j_{\rm baryonic}$, baryonic mass and morphology, whereby galaxies with higher bulge-to-total stellar mass ratios have lower $j_{\rm baryonic}$ at a given mass. It is important to keep in mind, however, that most galaxies in these studies are pure disk galaxies with little to no bulge component. Here, we investigate this correlation with DARK SAGE over the entire range of morphology. Figure 3.7 illustrates the $j_{\rm total,disk}$ (including both the cold gas and stellar disk components) to stellar mass relation for our galaxy sample. Like in Figure 3.5, the dots show the median values, and the dark and light shaded regions enclose 68 and 95 percent of the samples, respectively. We find that $j_{\rm total,disk}$ for disk-dominated and intermediate galaxies track $j_{\rm stellar,disk}$. Surprisingly however, bulge-dominated galaxies have the highest $j_{\rm total,disk}$. The scatter of the $j_{\rm total,disk}$ for disk-dominated and intermediate galaxies is about 0.20 dex and fairly independent of mass. For bulge-dominated galaxies, the scatter is about 0.4 dex in the first bin, and decreases with mass to $\sim$0.25 dex.

This contrasts with the left panel of Figure 3.5, which effectively shows $j_{\rm total,disk}$, arises because bulge-dominated galaxies contain disks with high gas fractions in DARK SAGE. Gas disks tend to have higher j than stellar disks, as disk stars preferentially form from the lowest-j gas in the disk (see figure 2 of Stevens et al. 2018). In bulge-dominated galaxies, these cold gas disks are typically low mass and more radially extended, and are therefore stable against star formation. As shown in Figure 3.4, the ratio of $j_{\rm coldgas,disk}$ and $j_{\rm stellar,disk}$ is much higher for bulge-dominated galaxies (around 6–8) than for intermediate and disk-dominated galaxies (closer to 2–3). The scatter in the specific angular momenta of disks for bulge-dominated galaxies may be due to the diversity of disk sizes and velocities. Note, though, that the masses of cold gas disks of bulge-dominated galaxies are negligible compared to the masses of their stellar bulges. We take a closer look at this in DARK SAGE by taking the ratio of cold gas mass to bulge stellar mass for bulge- and disk-dominated

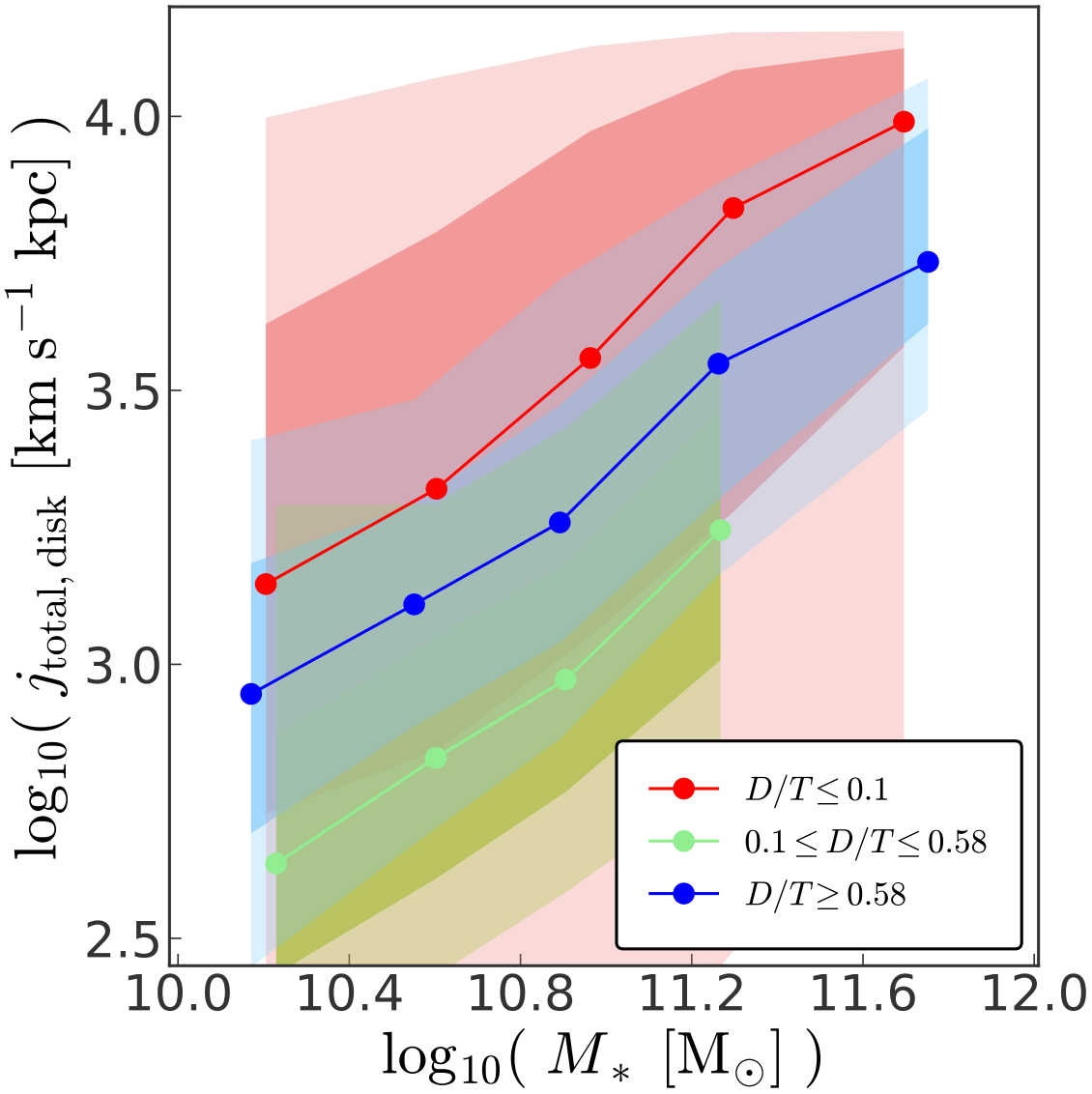

Figure 3.7: Total (stellar + gas) specific angular momentum of the disk as a function of stellar mass for bulge-dominated (red), intermediate (green), and disk-dominated (blue) galaxies. The figure includes running median lines, while the dark and light shaded regions enclose the inner 68 and 95 percent of the sample, respectively (as in Figure 3.5). We find that $j_{\rm total,disk}$ of disk-dominated and intermediate galaxies tracks $j_{\rm stellar,disk}$. Surprisingly, bulge-dominated galaxies have the highest $j_{\rm total,disk}$, implying that $j_{\rm coldgas,disk}$ boosts $j_{\rm total,disk}$.

galaxies. We find that this ratio for bulge-dominated galaxies in our sample is 100 times smaller than that of disk-dominated ones. For this reason, even if the total specific angular momentum of the disk is larger for bulge-dominated galaxies than for disk-dominated galaxies, the total specific angular momentum of the galaxy as a whole (stellar and gas disk plus stellar bulge specific angular momentum) is still smaller for bulge-dominated galaxies than for disk-dominated galaxies of the same stellar mass. We note that DARK SAGE was calibrated to match the mean H I fraction of galaxies as a function of stellar mass (see Stevens et al., 2016; Stevens & Brown, 2017). Therefore, any concern that bulge-dominated galaxies have overly massive cold gas disks in DARK SAGE is unwarranted. We discuss the observability of these extended gas disks in bulge-dominated galaxies in Section 4.6.

3.4 Dark matter specific angular momentum and Morphology: is there a correlation?

Some semi-analytic models use the simple assumption that the size of the galactic disk is related to the size of its host halo and its spin. This idea was first derived by Fall & Efstathiou (1980); Fall (1983); Mo et al. (1998), as galaxies are believed to initially form through the collapse of hot gas within the halo, which dissipates energy to create a rotationally-supported disk (Peebles, 1969). Analytic galaxy formation models show that galactic disks formed from halos with high spin should have large sizes (Mo et al., 1998). This simple idea is at the core of most semi-analytic models and thus provides a strong motivation to better understand how the dark matter halo impacts galaxy morphology. Seemingly contradicting this foundational framework, Rodriguez-Gomez et al. (2017) found no correlation between the halo spin parameter (Bullock et al., 2001) and kinematic morphology (i.e. dispersion- vs. rotation-dominated galaxies) within the stellar mass range 10^{11}–10^{12} for central galaxies at $z=0$ in the Illustris simulation. For stellar masses of 10^{10}–$10^{11}\,M_{\odot}$, however, they do find a small correlation, whereby rotation-dominated galaxies have a higher halo spin parameter than dispersion-dominated galaxies. At even lower stellar masses, this correlation becomes quite strong. Using DARK SAGE, we are able to confirm this when we make the same mass and morphology cuts as Rodriguez-Gomez et al. (2017).

Logically, the idea that halo spin drives galaxy morphology is inconsistent with the wide distribution of specific angular momentum at a given stellar mass for galaxies of all types compared to the much narrower distribution of specific angular momentum of halos at a given mass. Thus, galaxy morphology must largely decouple from halo spin (Romanowsky & Fall, 2012). It makes sense that halo spin should not determine whether a galaxy is spiral or elliptical; since massive elliptical galaxy evolution is punctuated with galaxy mergers, the dynamical details of which are likely to be a stronger driver of the angular momentum distribution than the halo spin. On the other hand, for less massive disk-dominated galaxies, halo spin should correlate with D/T as they are less affected by major mergers.

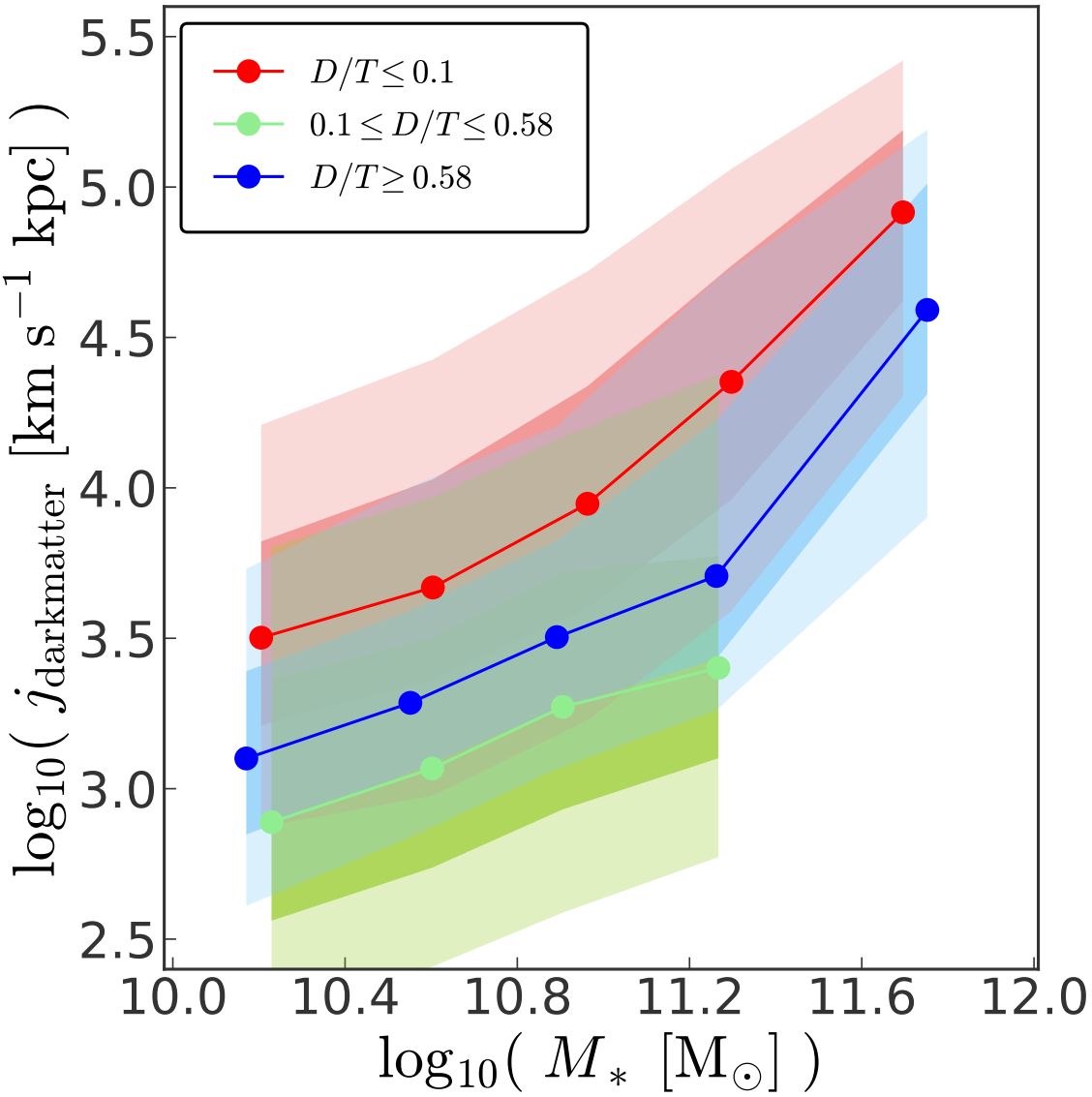

Figure 3.8: Dark matter specific angular momentum as a function of stellar mass for bulge-dominated (red), intermediate (green), and disk-dominated (blue) galaxies. Bins, lines, and shaded regions are the same as in Figure 3.5. Surprisingly, for a given stellar mass, bulge-dominated galaxies have a higher $j_{\rm darkmatter}$ than disk-dominated galaxies, while intermediate galaxies have the lowest $j_{\rm darkmatter}$.

Cole & Lacey (1996), Macciò et al. (2007), and Knebe & Power (2008) showed that there is little to no correlation between the Bullock et al. (2001) halo spin parameter and halo mass at $z=0$. Nonetheless, there is an existing correlation between $j_{\rm darkmatter}$ and halo mass (Fall & Efstathiou, 1980; Fall, 1983). We now examine the relation between $j_{\rm darkmatter}$ and both stellar mass and halo mass for bulge-dominated, intermediate, and disk-dominated galaxies. Figure 3.8 shows the relationship between $j_{\rm darkmatter}$ and stellar mass for our different morphological samples. We find that this relationship is counter-intuitive. Surprisingly, for a given stellar mass, bulge-dominated galaxies have higher $j_{\rm darkmatter}$ than disk-dominated galaxies. Moreover, intermediate galaxies have the lowest $j_{\rm darkmatter}$ out of the three galaxy populations. DARK SAGE disk-dominated and intermediate galaxies have a $j_{\rm darkmatter}$ scatter of 0.25 and 0.4 dex, respectively, both slightly increasing with stellar mass. Bulge-dominated galaxies have a scatter of 0.25 dex, independent of mass. We cross-checked these results against the earlier SAGE model (Croton et al., 2016); although the disk-to-total stellar mass morphology distribution is different, the morphology sequence in $j_{\rm darkmatter}$ is consistent.

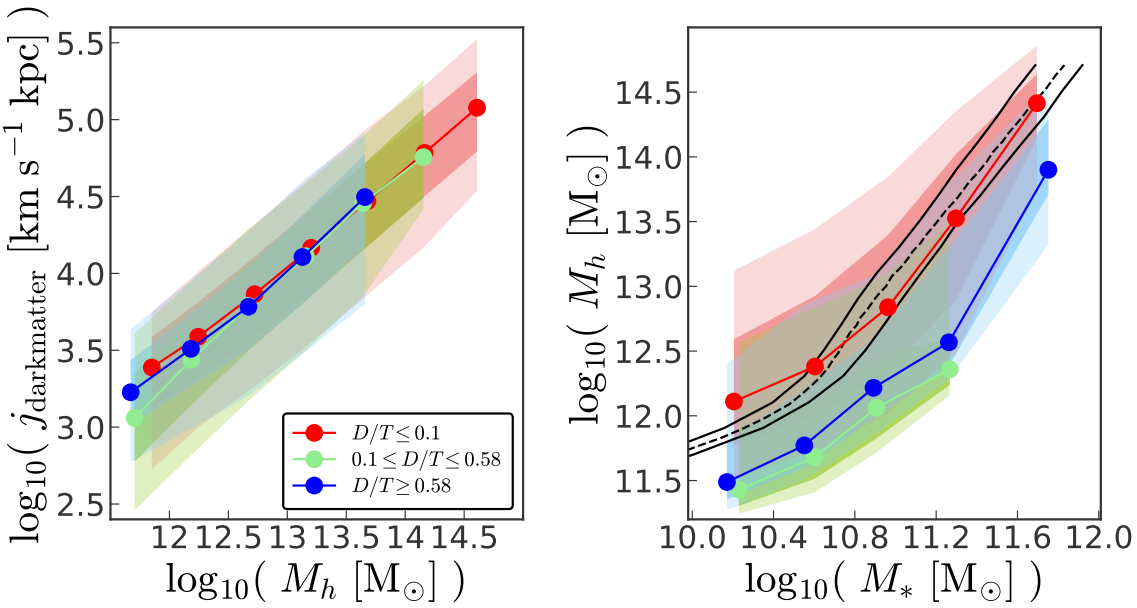

Figure 3.9: Left panel: Dark matter specific angular momentum as a function of halo mass. Right panel: Dark matter halo mass as a function of central-galaxy stellar mass. Bins, colored lines, and shaded regions are the same as in Figure 3.5. The black dashed and solid lines show the best-fitting relation and one-sigma scatter, respectively, from Behroozi et al. (2019). Bulge-dominated galaxies live in halos that are about five times more massive than disk-dominated galaxies at a given stellar mass, which explains the result in Figure 3.8. However, there is no dependence of morphology on $j_{\rm darkmatter}$ when controlling for halo mass.

To understand how DARK SAGE disk-dominated galaxies can have a higher $j_{\rm stellar}$ (Figure 3.5), but lower $j_{\rm darkmatter}$ than bulge-dominated galaxies (Figure 3.8), we explore the contribution of halo mass to these trends. The left panel of Figure 3.9 shows $j_{\rm darkmatter}$ as a function of halo mass for bulge-dominated (red), intermediate (green), and disk-dominated (blue) galaxies. When controlling for halo mass, the relationship

between angular momentum and morphology vanishes entirely at all but the lowest masses we probe. This means that halo mass is the main contributor to the morphological trends seen in Figure 3.8, while $j_{\rm darkmatter}$ does not seem to be driving galaxy morphology. These theoretical results, that galaxy morphology must decouple from halo spin at high masses, is consistent with observational results from Romanowsky & Fall (2012).

The right panel of Figure 3.9 shows the stellar mass-to-halo mass relation for all three galaxy populations in our sample. The black dashed line is the result from Behroozi et al. (2019), with the one-sigma scatter shown by the solid black lines. We find that, at fixed stellar mass, DARK SAGE bulge-dominated galaxies have higher halo masses than disk-dominated galaxies, while intermediate galaxies live in the lowest-mass halos. The halo mass scatter for disk-dominated and intermediate galaxies is about 0.25 dex, while for bulge-dominated galaxies it is about 0.3 dex, both independent of mass. A close examination of these results shows that bulge-dominated galaxies live in halos that are about five times more massive than the ones in which disk-dominated galaxies live. As we explore in the next section, bulge-dominated galaxies formed from halo mergers, and their high $j_{\rm darkmatter}$ comes purely from their high mass, which is expected for higher merger rates (Toomre, 1977; White & Rees, 1978; Heyl et al., 1994; Barnes & Hernquist, 1996). In a follow-up paper, we will further analyze the scatter and shape of the stellar–halo mass relation for different morphologies.

3.5 Summary and Discussion

We used the DARK SAGE semi-analytic model to investigate the relationship between the stellar mass, morphology, and specific angular momentum of galaxies with their parent halo properties. DARK SAGE is unique in its treatment of galaxy evolution, in part because it breaks disks into a series of annuli of fixed specific angular momentum, within which most secular processes are performed. Crucially, the net baryonic angular momentum of a galaxy depends on the entire history of its halo, and can therefore decouple from the halo's instantaneous properties. This not only has downstream effects for how the disks and bulges of galaxies are grown, but it also means the model is predictive (as opposed to prescribed) when it comes to relating galaxy morphology to the halo at $z = 0$. Here, we explored this for galaxies with stellar masses between 10^{10}–$10^{12}\,{\rm M}_{\odot}$. Our results are summarized as follows:

- DARK SAGE predicts a morphological sequence whereby, for a given stellar mass, $j_{\rm stellar,disk}$ increases with D/T. To compare with observational studies that measure the total stellar specific angular momentum, $j_{\rm stellar,gal}$, we explore the limiting cases where the bulge component has either the same specific angular momentum as the disk or zero. In the former limit,DARK SAGE predicts a relation between $j_{\rm stellar,gal}$, morphology, and stellar mass that matches observational studies from Fall & Romanowsky (2013); Obreschkow & Glazebrook (2014); Posti et al. (2018) (Figure 3.5).

- DARK SAGE predicts that at fixed stellar mass, galaxies with high $j_{\rm total,disk}$ tend to be bulge-dominated (Figure 3.7). Bulge-dominated galaxies can still have a disk component, and these disks exhibit high gas fractions. Generally, gas disks tend to have higher j than stellar disks, as disk stars preferentially form from the lowest-j gas in the disk. Thus, the higher a disk's gas fraction, the higher its j. We also show that the $j_{\rm total,disk}$ of disk-dominated and intermediate galaxies traces the $j_{\rm stellar,disk}$. Even though the total specific angular momentum of the disk is larger for bulge-dominated galaxies than for disk-dominated galaxies, the total specific angular momentum of the galaxy as a *whole* is still smaller for bulge-dominated galaxies than for disk-dominated galaxies of the same stellar mass.

- We find that the relationship between $j_{\rm darkmatter}$ and stellar morphology is not simple. At fixed stellar mass, bulge-dominated galaxies have a higher $j_{\rm darkmatter}$ than disk-dominated galaxies. Intermediate galaxies have the lowest $j_{\rm darkmatter}$ (Figure 3.8).

- To understand how bulge-dominated galaxies have high $j_{\rm darkmatter}$, we explore the correlation between $j_{\rm darkmatter}$ and halo mass. We find that halo mass is the main contributor to the morphological trends with $j_{\rm darkmatter}$. When controlling for halo mass, the relationship between angular momentum and morphology vanishes (left panel of Figure 3.9). We also find that DARK SAGE bulge-dominated galaxies live in halos that are about five times more massive than disk-dominated galaxies, whereas intermediate galaxies live in the least massive halos (right panel of Figure 3.9). Based on these results, halo mass and not $j_{\rm darkmatter}$ is the driver of the morphological trend we see, confirming previous analysis from Romanowsky & Fall (2012, see discussion in their sections 5.5 and 6.2).

We mainly focused on the angular momentum of galaxy disks because DARK SAGE does not compute the angular momentum of classical bulges (see 3.2.3 for further details). That being said, DARK SAGE prediction matching the Fall relation is unexpected since the observations measure the total specific angular momentum, which includes the bulge component. The agreement we find would only be preserved if galaxies in DARK SAGE had bulges with equal specific angular momentum as their disks. This would be a different interpretation of the observed morphological dependence of the Fall relation to the one suggested by Fall & Romanowsky (2018), according to whom all bulges follow one relation and all disks follow another relation, and galaxies are simply a weighted average of these two depending on their D/T. These different interpretations can be tested by accurately disentangling the bulge and disk components of intermediate galaxies and measuring their specific angular momenta separately.

We note that, in principle, our results may be sensitive to our semi-analytic model physical prescriptions and choice of values for the model's free parameters. However, the free parameters were calibrated to agree with the stellar mass function, the H I and H_2 mass function, and the mean H I mass fraction. As a result,

there is not as much freedom in the model as one might think. The model is under constant development, and a soon-to-be-released new version by Stevens et al. (in prep.) will not only overhaul many aspects of the model to be better physically motivated, but will also significantly reduce the number of free parameters. Future work with this model would allow us to explore the morphology–angular momentum–stellar mass plane (among many other galaxy scaling relations) in even greater detail.

An interesting prediction in our results is that bulge-dominated galaxies harbour cold gas disks with high specific angular momentum relative to their stellar disks. However, on average, the mass ratio of the gas disk to the stellar bulge for these systems is of order 1/100. As such, assuming the stellar components of these galaxies have non-zero angular momentum, the contribution of the extended gas disks to the overall specific angular momenta is effectively negligible.

Following the tight relationship between the H I size and mass of galaxies, which DARK SAGE has proven to reproduce successfully (Lutz et al., 2018; Stevens et al., 2019), we expect that in the real Universe, some bulge-dominated galaxies contain extended H I disks. Within our stellar mass range, we found several of these galaxies with H I disks up to 2 to 5 times larger in size than the Milky Way (Oosterloo et al., 2007; Donovan et al., 2009; Struve et al., 2010; Hagen et al., 2016). These extended cold gas disks might result from gas accretion and/or merging events of gas-rich nearby dwarf companions, carrying more angular momentum than the stellar component of the host galaxy.

Observationally, bulge-dominated galaxies with extended H I disks within our stellar mass range have neither been widely detected nor ruled out. In Figure 3.10 we explore the capability of current H I surveys to detect these galaxies. The figure shows the ratio of H I mass to stellar mass as a function of stellar mass for bulge-dominated (red) and disk-dominated (blue) DARK SAGE galaxies. The solid black and grey lines show the detection limits for the GALEX Arecibo SDSS survey (GASS) (Catinella et al., 2010) and the Arecibo Legacy Fast ALFA Survey (ALFALFA) (Giovanelli et al., 2005), respectively. The detection limit for GASS is taken to be $M_{\rm HI} > \max\left(10^{8.7}\,{\rm M}_{\odot}, 0.015\,M_{*}\right)$, while for ALFALFA, we used the H I-detected volume-limited sample from Brown et al. (2015). The ALFALFA line represents the stacked average H I fraction as a function of galaxy stellar mass (from figure 3 in Brown et al., 2015). We see that, for stellar masses of 10^{10}–$10^{11.5}\,{\rm M}_{\odot}$, most bulge-dominated galaxies fall below the ALFALFA detection limit. However, theoretically, DARK SAGE predicts that 4 percent of bulge-dominated galaxies would be detectable by ALFALFA. Moreover, 38 percent of bulge-dominated galaxies have gas disks that would be detectable by GASS.

To test the ALFALFA prediction, we calculated the H I detection fraction using the ECO catalog from the RESOLVE survey, which uses ALFALFA data (Moffett et al., 2015). We find a detection rate of about 9

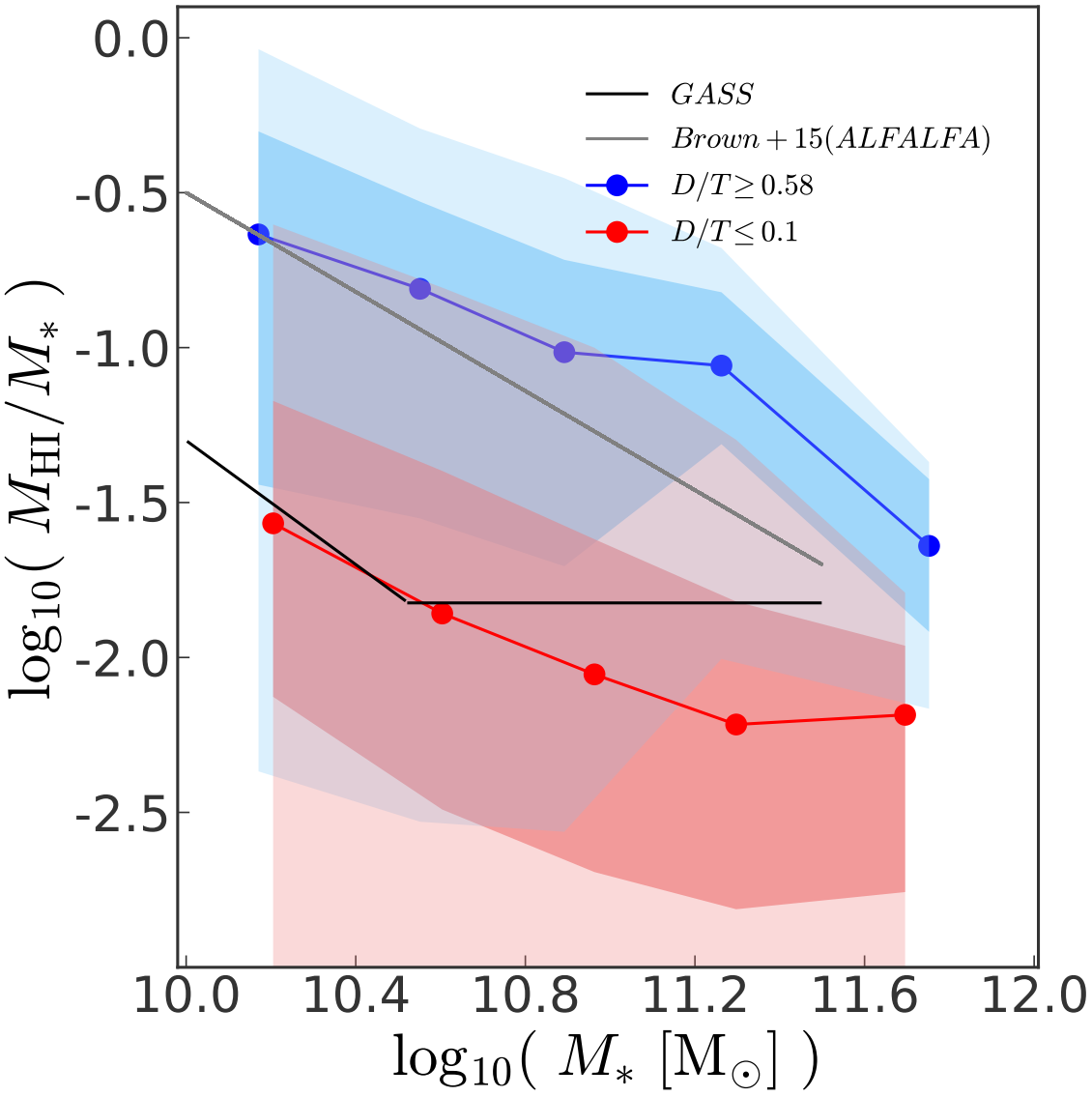

Figure 3.10: Ratio of H I mass to stellar mass as a function of stellar mass for bulge-dominated (red) and disk-dominated (blue) galaxies in our sample. The solid grey and black lines show the ALFALFA and GASS detection limits, respectively, up to stellar masses of $10^{11.5}\,{\rm M}_\odot$. About 19 percent of bulge-dominated galaxies within our sample should theoretically be detected by both ALFALFA and GASS.

percent for early-type galaxies. This detection may go as high as 22 percent if confused sources[2] are included. To test the GASS prediction, we find that the observed H I detection fraction in GASS for galaxies with stellar masses greater than $10^{10}\,M_{\odot}$ and $D/T < 0.1$ is about 13 percent excluding confused sources (Cook, private communication – cf. Cook et al., 2019), which shows that DARK SAGE overestimates this detection fraction. It appears that DARK SAGE over-predicts bulge-dominated galaxies with H I detection in GASS by a factor of 3.

Our results imply that the angular momentum of the disk and that of dark matter are not tied together in massive galaxies. In DARK SAGE, the size of the disk and the halo spin are correlated, but not bound to each other; this is reflected, for example, in H I-excess galaxies – see Lutz et al. 2018). As pointed out by Romanowsky & Fall (2012), there are internal and external physical mechanisms, such as mergers, outflows, galaxy stripping, and radial migration of stars, that contribute to the diversity of angular momentum acquisition in the baryonic and dark matter components (see discussion in their section 6.3). We have shown that the angular momenta of the disk and dark matter differ for each galaxy type. The halo spin in DARK SAGE determines how gas in a single cooling episode is added to the disk, and the way in which matter is distributed in the disk depends on the galaxy's entire history.

Although we focus on trends between specific angular momentum, morphology, and stellar mass here, we find that DARK SAGE galaxies have a scatter in stellar mass larger than 0.2 dex at a fixed halo mass. The scatter in the stellar–halo mass relation has profound implications on the galaxy–halo connection. Understanding the scatter may constrain different galaxy quenching models that describe diverse ways in which galaxies gain halo mass (Behroozi et al., 2019; Man et al., 2019). In our upcoming paper, we will examine the scatter in the stellar–halo mass relation, and its correlation with morphology and color to further understand the morphological sequence found in this paper.

ACKNOWLEDGEMENTS We thank Amanda Moffett, Darren Croton, and Victor Calderón for insightful conversations. We also thank the referee for the very helpful comments that developed this manuscript to its best informative state. This paper used data from the Theoretical Astrophysical Observatory (TAO) https://tao.asvo.org.au/. TAO is part of the All-Sky Virtual Observatory (ASVO) funded and supported by Swinburne University of Technology, Astronomy Australia Limited, and the Australian Government through the Commonwealth's Education Investment Fund and National Collaborative Research Infrastructure Strategy. We used computational facilities from the Vanderbilt Advanced Computing Center for Research and Education (ACCRE). Literature reviews for this work were conducted with NASAâs Astrophysics Data System. Results were produced using the IPython package (Pérez & Granger, 2007), SCIPY (Jones et al., 2001),

[2] A confusion flag here means that there are at least two sources within the Arecibo beam, so the H I could be coming from a different galaxy than the early-type one

MATPLOTLIB (Hunter, 2007), ASTROPY (Robitaille et al., 2013), and NUMPY (Van Der Walt et al., 2011).

CHAPTER 4

Paper 2 - Why do semi-analytic models predict higher scatter in the stellar mass–halo mass relation than cosmological simulations?

Motivation

Similar to Chapter 3's motivation, around the 1990s, simulations not only produced galaxies with deficient angular momentum, but also overproduced the amount of massive galaxies (Navarro et al., 1997; Kauffmann et al., 1999). Stellar mass functions derived from observations shows that there are relatively few enormous galaxies in the real Universe. To match observations, simulations needed to introduce a mechanism that would suppress the growth of galaxies. Here is where feedback was introduced in the galaxy formation models (Springel & Hernquist, 2003; Di Matteo et al., 2005; Sijacki et al., 2007). By including stellar and AGN feedback, the number of massive galaxies in simulations began to match the observed stellar mass function. Thus, feedback became the main crux of our understanding of galaxy evolution. Feedback suppresses star formation, which in turn allows galaxies to grow steadily. Once feedback was introduced, simulated galaxies at halo masses above $10^{11}\,M_{\odot}$ were matching the empirical stellar-to-halo mass relation (Behroozi et al., 2010; Behroozi et al., 2013b; Moster et al., 2013; Kravtsov et al., 2018).

Generally speaking, hydrodynamical simulations use the mean or median stellar-to-halo mass relation from empirical results to calibrate their models. The scatter in stellar mass at fixed halo mass produced within the stellar-to-halo mass relation is a physical prediction of the model. Generally, hydrodynamical simulations agree with observations in that the scatter in stellar mass at fixed halo mass is less than 0.2 dex for halo masses above $10^{11}\,M_{\odot}$ (Mandelbaum et al., 2006; Conroy et al., 2007; More et al., 2011b; Leauthaud et al., 2012; Coupon et al., 2015). Nevertheless, Wechsler & Tinker (2018) shows that several semi-analytic models disagree with empirical and hydrodynamical results. SAMs predict this scatter to be about 2 orders of magnitude above that observed. A simple experiment where we turn off one mode of AGN feedback allows DARK SAGE galaxies to match the stellar mass scatter in hydrodynamical simulations and most empirical relations. Given the influence of black hole physics in this scatter, in this chapter, we develop a model in which DARK SAGE galaxies are forced to follow the black hole mass–halo mass median relation from ILLUSTRISTNG. We implement this model in DARK SAGE and add an input parameter that allow us to give a desired scatter in BH mass to test how varying that scatter would affect the scatter in stellar mass as a function of halo mass.

Abstract

The galaxy–halo connection is a fundamental bridge between observations and theory that supports our

understanding of the underlying physics of galaxy formation. Generally, empirical models use observations to map galaxy stellar masses to halo masses from N-body simulations to infer several statistical characteristics, one of them being the mean stellar mass-to-halo mass relation (SMHMR). Most hydrodynamical simulations are calibrated to match the mean SMHMR from empirical relations, but the *scatter* in stellar mass that results after calibration is a physical prediction of the simulation. Interestingly, in general, there are discrepancies of a factor of 2 in the stellar-mass scatter predictions between simulations. Semi-analytic models (SAMs) systematically predict higher stellar-mass scatter at a given halo mass than hydrodynamical simulations and most empirical models. Our goal is to investigate the physical origin of this scatter by exploring modifications to the physics in the SAM DARK SAGE. Our experiments show that turning off *radio mode* black hole feedback reduces the stellar-mass scatter significantly. Modifying black hole seeding and treatment of Active Galactic Nuclei (AGN) feedback reduces the scatter in stellar mass at halo masses between $10^{11-14}\,\mathrm{M}_{\odot}$. Taken together, these results suggest that *radio mode* feedback in SAMs acts in a qualitatively different way than AGN feedback implemented in cosmological simulations. This means that either or both may require substantial modification to match the empirically inferred SMHMR scatter.

4.1 Introduction

The standard model of cosmology, ΛCDM, is the backbone for our understanding of galaxy formation (Blumenthal et al., 1984; Cen & Ostriker, 1994, 1999b,a). Within this model, collapsed dark matter halos forming filaments in the large-scale structure of the Universe serve as the skeleton to the luminous material accumulated in galaxies (White & Rees, 1978; Kauffmann et al., 1993). Dark matter halos are key to our physical modeling of galaxy formation, but the problem is the difficulty to directly observe them. Naturally, the connection between galaxies and dark matter halos form a fundamental bridge between observations and theory that supports our understanding of the underlying physics of galaxy formation.

For decades, *empirical* and *physical* models have been used to study the multivariate distributions of properties formed and evolved in galaxies and halos. *Empirical models* constrain the relationship between halos and galaxies by assigning galaxies to halos in such a way that observations (e.g. galaxy abundance and spatial correlations) are reproduced, whereas *physical models* directly evolve galaxies in dark matter halos while parameterizing the physics of galaxy formation (Wechsler & Tinker, 2018). Semi-empirical or semi-analytical models (SAMs) and hydrodynamical simulations are parametric models that connect the observable Universe with theory. However, SAMs are generally built on physically and/or empirically motivated relations of galaxy properties that are described macroscopically, whereas hydrodynamical simulations self-consistently evolves galaxy evolution in tandem with the large-scale structure of the (simulated) Universe. Generally, *empirical models* map the stellar mass of galaxies to halo masses from N-body simulations to infer a mean stellar

mass-to-halo mass relation (SMHMR) that can be used to calibrate *physical models* (Pillepich et al., 2018; Forbes et al., 2019). The stellar-mass scatter produced from this relation is a prediction from simulations.

Most *empirical models* fundamentally assume that the scatter in stellar mass ($\sigma(\log_{10}(M_*|M_h))$) is irreducible, whereas in *physical models*, one can distinguish between irreducible scatter and the scatter owing to other galaxy properties. Observationally, the scatter in stellar mass has been constrained using galaxy clustering (Leauthaud et al., 2012; Coupon et al., 2015), galaxy–galaxy lensing (Mandelbaum et al., 2006; Hudson et al., 2015), and satellite kinematics (Conroy et al., 2007; More et al., 2011b). Using halo bias, Tinker et al. (2017) determined that a scatter model with value of $\sigma(\log_{10}(M_*|M_h)) = 0.18$ dex from their SMHMR prediction of the Baryon Oscillation Spectroscopic Survey (BOSS) from the Sloan Digital Sky Survey (SDSS) galaxies at $z = 0.5$ fits best for galaxies with stellar masses $M_* > 10^{11}$. Adding the galaxy–galaxy lensing technique alongside clustering from the SDSS, Zu & Mandelbaum (2015) found scatter values of $\sigma(\log_{10}(M_*|M_h)) = 0.18$ dex at halo masses of $10^{14}\,\mathrm{M}_\odot$ and $\sigma(\log_{10}(M_*|M_h)) = 0.22$ dex at halo masses of $10^{12}\,\mathrm{M}_\odot$. Estimating halo masses from X-ray measurements, Kravtsov et al. (2018) find $\sigma(\log_{10}(M_*|M_h)) = 0.17$ dex from a direct measurement of the scatter in the mean SMHMR at halo masses between $10^{14} - 10^{15}\,\mathrm{M}_\odot$. Additionally, tracing the gravitational potential of central galaxies using satellite kinematics, More et al. (2011b) finds $\sigma(\log_{10}(M_*|M_h)) < 0.2$ dex for galaxies with stellar masses between $10^{10} - 10^{12}\,\mathrm{M}_\odot$, results that are in agreement with galaxy clustering and galaxy lensing results. All in all, the scatter is generally constrained to be 0.2 dex for central galaxies ($z = 0$) with $M_h > 10^{11}\,\mathrm{M}_\odot$ (Figure 4.1).

From the perspective of galaxy formation models, Wechsler & Tinker (2018) compares $\sigma(\log_{10}(M_*|M_h))$ predictions from empirical, SAMs, and hydrodynamical simulations. Several *empirical models* (Hearin & Watson, 2013; Behroozi et al., 2013a; Becker, 2015) and hydrodynamical simulations (McAlpine et al., 2016; Pillepich et al., 2018) agree that the scatter in stellar mass at fixed halo mass is constrained to be 0.2 dex for galaxies with halo masses above $10^{12}\,\mathrm{M}_\odot$. However, SAMs predict a much larger scatter in stellar mass, ranging between $0.2 - 0.4$ dex at halo masses between $10^{11} - 10^{15}\,\mathrm{M}_\odot$ (Henriques et al., 2015; Croton et al., 2016; Stevens et al., 2016). These predictions are in line with the Behroozi et al. (2019) *empirical model*, which uses star formation histories that are matched to the halo formation time.

In this paper, we investigate the physical origin of the scatter in the stellar mass–halo mass relation by exploring modifications to the physics in the SAM DARK SAGE. We find compelling evidence that much of the scatter arises from the treatment of AGN quenching, so our modifications focus on this area of the SAM. Within DARK SAGE, we isolate two potential contributions to the stellar mass scatter at fixed halo mass: 1) the black hole mass distribution, and 2) the treatment of AGN feedback. To explore the former, we force DARK SAGE to follow the black hole mass–halo mass median relation produced by the ILLUSTRISTNG 300-1 hydrodynamical simulation using the highest-resolution box (TNG hereafter). We vary the scatter in

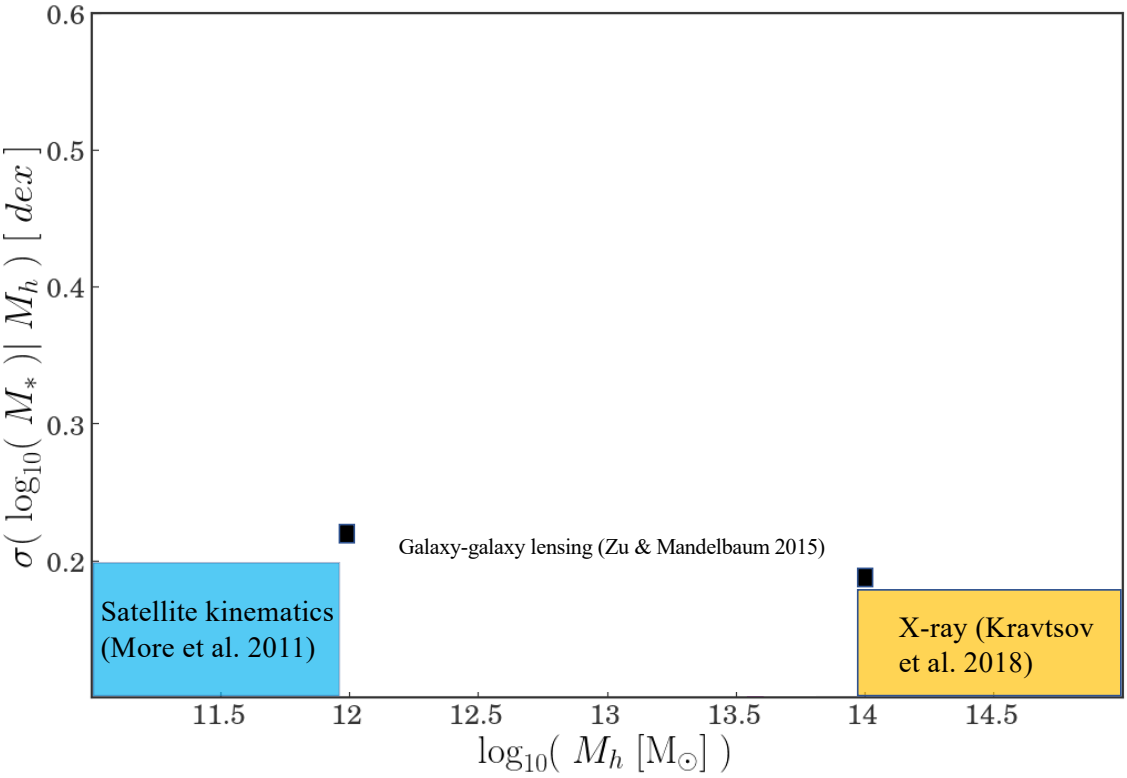

Figure 4.1: The stellar mass scatter – Observational constrains from satellite kinematics (More et al., 2011b), galaxy-galaxy lensing (Zu & Mandelbaum, 2015), and X-ray (Kravtsov et al., 2018) measurements showing that the scatter in stellar mass at fixed halo mass is 0.2 dex for central galaxies ($z = 0$) with $M_h > 10^{12}\,\mathrm{M}_\odot$.

black hole mass at a given halo mass to determine if this affects the scatter in stellar mass. To explore the latter, we run DARK SAGE with AGN quenching models that affect the various gas reservoirs in the SAM differently.

This paper is organized as follows. In Section 4.2, we present an overview of the semi-analytic model DARK SAGE, where we detail how black hole seeding and AGN feedback is implemented in the model. We do the same in Section 4.3 for the TNG simulation. In section 4.4, we examine the stellar mass-to-halo mass relation in both models. Section 4.5 explores the black hole seeding and AGN effect in changing the $\sigma(\log_{10}(M_*|M_h))$. Sections 4.6 and 4.7 discuss our results and present conclusions. DARK SAGE uses cosmological parameters from the Wilkinson Microwave Anisotropy Probe data (Spergel et al., 2003), where $\Omega_M = 0.25$, $\Omega_\Lambda = 0.75$, $\Omega_b = 0.045$, $\sigma_8 = 0.9$, and $h = 0.73$.

4.2 Semi-analytic Model: DARK SAGE

DARK SAGE (Stevens et al., 2016) is a semi-analytic model of galaxy formation and evolution that uniquely evolves the one-dimensional structure of disks in galaxies. This is done by breaking down galaxy disks into 30 equally spaced logarithmic bins of specific angular momentum. In DARK SAGE, galaxies evolve their stellar and gas disk structure to calculate physical processes happening within halos of hot gas that radiatively cool and condense to form a cold gas disk that is supported by angular momentum (White & Rees, 1978). The orientation of angular momentum vector from the cooling gas is assumed to be parallel to that of the halo at the cooling time. Once the gas is cool, it forms stars, which are then transferred to the respective angular momentum annulus of the stellar disk structure. Both major and minor mergers are important drivers of disk evolution and are treated carefully in DARK SAGE. Major mergers completely destroy an existing disk and will acquire a new set of annuli for gas reaccretion. Minor mergers can also contribute to the mass build-up of disk structures within a galaxy's lifetime. As galaxy mergers may regulate star formation, DARK SAGE an excellent tool to study the cycle of stellar build-up and quenching.

In this paper, we use the 2018 version of DARK SAGE (Stevens et al., 2018). In this new version, DARK SAGE updates the way in which the cooling scale radius for the *hot-mode* cooling is done a fitting function from Stevens et al. (2017). DARK SAGE now calculates the stellar disk scale radius using the half-mass radius and the radius at which 90 percent of the matter is enclosed. This is done now as opposed to making no distinction between the scale radius for cooling and the actual scale radius of the galaxy's stellar disk. Lastly, DARK SAGE updates calculations on the dispersion support in disks by introducin a factor that takes into account the fraction of gravity balanced by the rotational (circular) motion. The model uses merger trees from the Millennium simulation, which has a boxsize of 500 h^{-1} Mpc (Springel et al., 2005). The simulation uses cosmological parameters from the Wilkinson Microwave Anisotropy Probe data (Spergel et al., 2003),

where $\Omega_M = 0.25$, $\Omega_\Lambda = 0.75$, $\Omega_b = 0.045$, $\sigma_8 = 0.9$, and $h = 0.73$. The simulation has a particle mass resolution of $8.6\times10^8\ h^{-1}\,\mathrm{M}_\odot$. Our DARK SAGE sample contains galaxies within the stellar mass range of $10^9 - 10^{12}\,\mathrm{M}_\odot$. To ensure that galaxies at redshift 0 live in well-resolved halos, we adopt a halo mass cut of $10^{11.2}\,\mathrm{M}_\odot$. For a more detailed description of DARK SAGE, please refer to Stevens et al. (2016).

4.3 Hydrodynamical simulation: TNG

The ILLUSTRISTNG is a state-of-the-art hydrodynamical simulation that models the evolution of galaxies and their environments in a cosmological context (Pillepich et al., 2018; Springel et al., 2018; Nelson et al., 2019a; Naiman et al., 2018; Nelson et al., 2018; Marinacci et al., 2018). The simulation was developed as an upgrade to the original Illustris simulation (Vogelsberger et al., 2014b,a; Genel et al., 2014; Sijacki et al., 2015; Nelson et al., 2015). It includes improved physical models and higher spatial and mass resolution. TNG includes a set of physical processes such as gas cooling and heating, star formation, stellar feedback, black hole growth, and feedback from active galactic nuclei. The simulation has been used to study a wide range of topics, including the role of feedback in shaping the properties of galaxies (Weinberger et al., 2018; Terrazas et al., 2020), the connection between the properties of galaxies and their dark matter halos (Bose et al., 2019; Martizzi et al., 2020; Zanisi et al., 2020), and the properties of galaxy clusters and their galaxies (Ntampaka et al., 2019; Sales et al., 2020; Joshi et al., 2020).

4.3.1 Black hole growth in the TNG

TNG sows $8\times10^5\,h^{-1}\,\mathrm{M}_\odot$ black hole seeds when halos reach a critical mass of $5\times10^{10}\,h^{-1}\,\mathrm{M}_\odot$ (Weinberger et al., 2017). After being seeded, black holes grow purely through Bondi accretion limited by the Eddington rate, which scales as $\dot{m}_{Bondi} \propto \mathrm{m}_{BH}^2$. At the start, black holes have low-accretion rates. After enough gas reaches the center of the halo, black holes start producing higher accretion rates, allowing for future rapid growth. During this phase, the feedback is significantly strong, and the black hole gas supply becomes self-regulated. Around black hole masses of $10^8\,\mathrm{M}_\odot$, black holes begin to slow down their growth, going back into low-accretion rates.

When running TNG using black hole seeds below $10^6\,\mathrm{M}_\odot$, the black holes take more than a Gyr to grow to supermassive black hole (SMBH) size because the Bondi accretion rate scales as $\dot{m}_{Bondi} \propto \mathrm{M}_{BH}^2$ (Weinberger et al., 2017). Therefore, black holes growth gets delayed as more gas is needed in the center of halos for rapid growth. This means that black holes in $10^{12}\,\mathrm{M}_\odot$ halos have not ended their rapid accretion period at redshift 0. In turn, there is less feedback energy injected into galaxies, which causes significant cold gas accumulation. As a result, stars form at higher rates, growing galaxies with higher stellar masses over the whole range of halos. Additionally, changing the threshold of the halo mass by which a black hole should

be seeded has similar results. Lowering the black hole seed mass while increasing the halo mass threshold requirement to seed the black hole delays black hole growth although not as significantly as in the previous described case (Weinberger et al., 2017).

4.3.2 AGN feedback in the TNG

The TNG simulation includes gas dynamics, which enables it to model the effects of feedback mechanisms more accurately compared to semi-analytic models. Here, AGN feedback energy is injected into gas cells directly, and its effects on the gas are then tracked. TNG uses two distinct feedback modes: the *thermal mode* at high-accretion rates and the *kinetic mode* at low-accretion rates (Weinberger et al., 2017). The *thermal mode* introduces thermal energy isotropically to the surrounding gas. The *kinetic mode* injects directed momentum kicks into the local environment. The AGN feedback model in DARK SAGE also has two modes (as described in section **??**), but they operate differently in terms of physics and when these modes are active. The *quasar mode*, equivalent to the *thermal mode* in TNG, operates only during mergers and couples to the ISM. The *radio mode*, equivalent to the *kinetic mode* in TNG, operates at all times, becoming more important at higher stellar masses. The *kinetic mode* in TNG is particularly effective in high-mass galaxies (Pillepich et al., 2018; Springel et al., 2018). This is because the energy from the outflow or jet is deposited over a large volume, and the mass of the gas that is accelerated is proportional to the volume. As a result, the kinetic energy per unit mass of gas is lower in low-mass galaxies than in high-mass galaxies. The *thermal mode*, on the other hand, is more effective in low-mass galaxies (Nelson et al., 2019a). This is because the gas content in low-mass galaxies is less massive and has lower binding energy than the gas in high-mass galaxies. As a result, it is easier to heat and disperse the gas.

TNG uses a combination of the Bondi-Hoyle (equation 4.1) and the Eddington (equation 4.2) accretion rates to determine if the AGN feedback should be *thermal mode* or *kinetic mode* (Weinberger et al., 2017). The model assumes that black holes accreet at the Bondi rate, but limited by the Eddington rate. This accretion rate is obtained by taking the minimum of both rates, $\dot{m}_{\rm Bondi}$ (equation 4.4).

$$\dot{m}_{\rm Bondi} = \frac{4\pi G^2 m_{\rm BH}^2 \rho}{c_s^3}, \tag{4.1}$$

$$\dot{m}_{\rm Edd} = \frac{4\pi G m_{\rm BH} m_p}{\varepsilon_r \sigma_T}\, c, \tag{4.2}$$

$$\dot{m}_{\rm BH} = min(\dot{m}_{\rm Bondi}, \dot{m}_{\rm Edd}), \tag{4.3}$$

A black hole mass dependence threshold, χ, is calculated to determine the energy output.

$$\chi = min\left[0.002\left(\frac{m_{\rm BH}}{10^8\,{\rm M}_\odot}\right)^2, 0.1\right], \tag{4.4}$$

If the Eddington ratio exceeds χ, then the *thermal mode* feedback takes place. The energy output becomes:

$$\dot{E}_{\text{thermal AGN}} = 5.66\times10^{42}\text{erg s}^{-1}\,\frac{\dot{m}_{\rm BH}}{5\times10^{-3}\,{\rm M}_\odot\ \text{yr}^{-1}}, \tag{4.5}$$

For low-accretion rates, energy output is:

$$\dot{E}_{\text{max kinetic AGN}} = 5.66\times10^{43}\text{erg s}^{-1}\,\frac{\dot{m}_{\rm BH}}{5\times10^{-3}\,{\rm M}_\odot\ \text{yr}^{-1}}, \tag{4.6}$$

In TNG, the star formation efficiency is highest around halo masses of $10^{12}\,{\rm M}_\odot$. To quench massive halos, SMBHs transition to the low-accretion state and remain as such throughout their ongoing evolution (Weinberger et al., 2017). This transition takes place around black hole masses of $10^8\,{\rm M}_\odot$. Because of the tight relationship between black hole mass-bulge mass (or stellar mass), the *kinetic mode* feedback takes over for galaxies above $10^{10.25}\,{\rm M}_\odot$, reducing greatly star formation rates, and fully quenching galaxies above such mass.

There are some limitations to using TNG, or hydrodynamical simulations in general, to model AGN feedback. One of the main limitations is the particle resolution. In order to accurately model the details of the feedback processes, simulations need to have high resolution. Additionally, the exact physical mechanisms behind AGN feedback are still not fully understood, and so there is some uncertainty in the parameters that are used to model the feedback in the simulations (Somerville & Davé, 2015). Combining the work of semi-analytic models alongside hydrodynamical simulations provides a valuable approach for studying the effects of AGN feedback on galaxy formation and evolution.

4.4 Stellar Mass-to-Halo mass relation for TNG and DARK SAGE galaxies

One of the main differences between DARK SAGE and TNG is how feedback and black hole seeding is implemented. Because feedback helps regulate the growth of galaxies, understanding the relationship between black hole physics, stellar mass, and halo mass is important. Weinberger et al. (2017); Weinberger et al. (2018) show that the quenched fraction of galaxies is closely tied to the stellar mass and black hole mass. The change in star formation efficiency at black hole masses close to $10^8\,{\rm M}_\odot$ is caused by the switch from the *thermal* to *kinetic mode* feedback, which is even more apparent for galaxies with stellar masses around $10^{10.25}\,{\rm M}_\odot$ (see figure 5 in both Weinberger et al. (2017); Weinberger et al. (2018)). When massive galaxies

switch to *kinetic mode* feedback, the star formation efficiency is significantly reduced, which in turn, changes the shape of the star formation rate and significantly reduces cooling. As a result, galaxies with black holes above $10^8\,M_\odot$ have zero mean star formation rates.

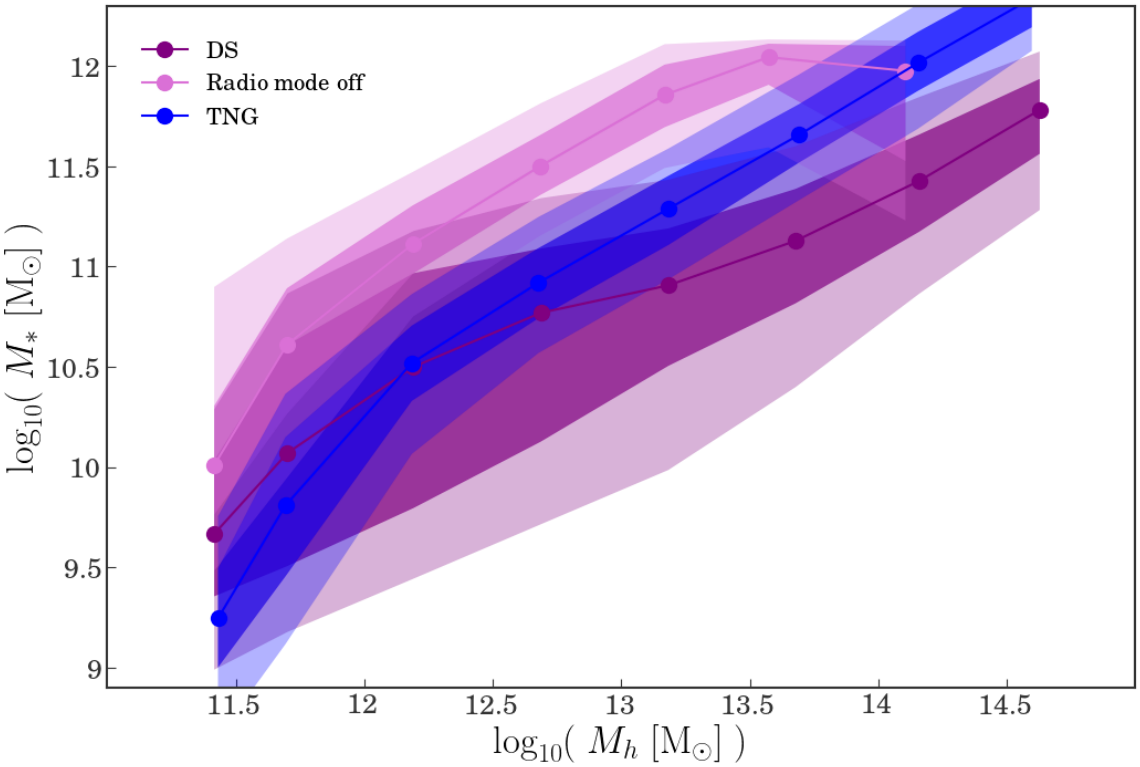

Figure 4.2: Stellar mass as a function of halo mass for central galaxies using DARK SAGE (purple), DARK SAGE run when we turn off radio mode feedback (violet), and TNG (blue). The solid line connecting the dots shows the median binned by halo mass. The dark and light shaded regions enclose 68 and 95 percent of the data, respectively. Surprisingly, when we turn off *radio mode* feedback, the scatter in stellar mass at fixed halo mass reduces significantly at all halo masses. Additionally, now all DARK SAGE galaxies have higher stellar masses at fixed halo mass than in TNG. All models predict different slopes, where TNG galaxies that live in more massive halos have higher stellar masses than fiducial DARK SAGE galaxies.

Figure 4.2 shows the stellar mass-to-halo mass relation for central galaxies in TNG (blue), DARK SAGE when *radio mode* feedback is turned off (violet), and fiducial DARK SAGE (purple). The solid line connecting the dots shows the median binned by halo mass. The dark and light shaded regions enclose 68 and 95 percent of the data, respectively. We see that all models have significantly different median slopes and scatter. Generally, in high-mass halos, TNG galaxies have more stellar mass than DARK SAGE galaxies. This relationship flips when looking at the low-mass halos. The differences in the slopes is possibly due to the fact that DARK SAGE is calibrated to match the Baldry et al. (2008) stellar mass function, which cuts down near $10^{12}\,M_\odot$, whereas TNG galaxies match better to Bernardi et al. (2013), a sample with few more massive galaxies (Pillepich et al., 2018). It is important to note that TNG300 was calibrated using the same

model parameterizations as the TNG100 (Nelson et al., 2019b), so it is known to overproduce high stellar mass galaxies. In this work, we are not including the "rescaling factor" used to used to scale the particle masses and resolution of the simulation. While TNG galaxies have an approximately constant scatter, DARK SAGE has a significantly larger scatter at low halo masses that decreases with increasing halo mass.

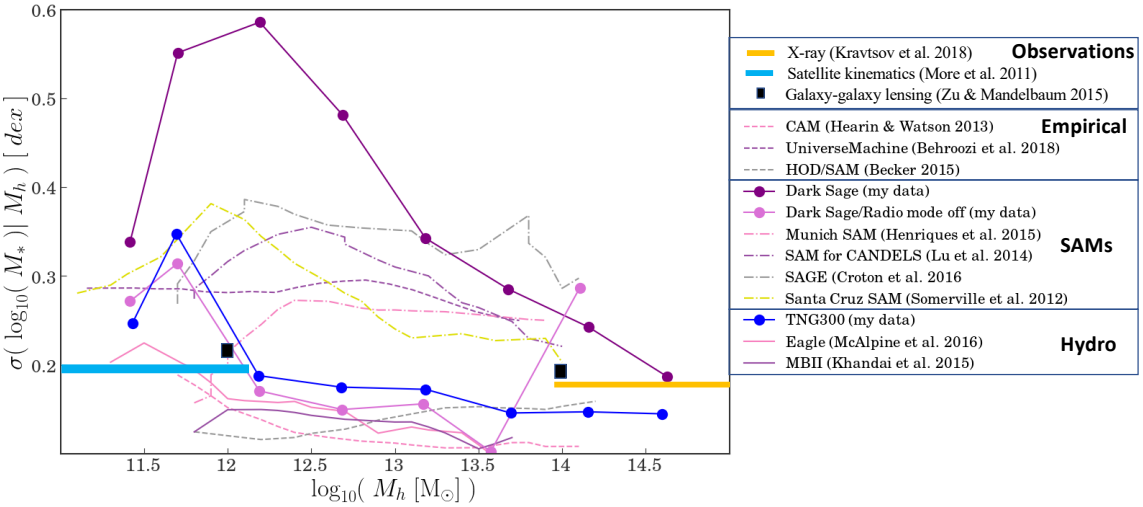

Figure 4.3: The stellar mass scatter – computed as half the 16th–84th interpercentile range – at fixed halo mass ($\sigma(\log_{10}(M_*|M_h))$) as a function of halo mass for central galaxies using DARK SAGE (purple), DARK SAGE run when we turn off radio mode feedback (violet), and TNG (blue). This plot includes data from various theoretical, empirical models, and observations from figure 4.1 (Wechsler & Tinker, 2018). The yellow and blue bars show the stellar-mass scatter from X-ray and satellite kinematic measurements, respectively (Kravtsov et al., 2018; More et al., 2011b). The black dots show the galaxy–galaxy lensing constraint (Zu & Mandelbaum, 2015). The dashed lines show the empirical models from Behroozi et al. (2019) (black), Becker (2015) (dark violet), and Hearin & Watson (2013) (dark blue). The solid lines are the semi-analytic model predictions from Henriques et al. (2015) (light green), Lu et al. (2014) (yellow), Croton et al. (2016) (red), Somerville et al. (2012) (orange) as well as from hydrodynamical simulations EAGLE (McAlpine et al., 2016) (dark red) and MASSIVEBLACK II (Khandai et al., 2015) (green). The stellar mass scatter is significantly larger in DARK SAGE compared to TNG and most models at roughly all masses. We find that when we turn off radio mode feedback, the scatter in stellar mass at fixed halo mass reduces significantly at all halo masses. However, now all DARK SAGE galaxies have higher stellar masses at fixed halo mass than in TNG.

Surprisingly, when the *radio mode* feedback is turned off in DARK SAGE, the scatter in stellar mass is significantly reduced, closely resembling that of TNG. Interestingly, a similar experiment only turning off *quasar mode* or stellar feedback shows no significant change in the stellar-mass scatter. This simple experiment shows that the *radio mode* feedback in DARK SAGE contributes significantly to the large scatter in stellar mass at fixed halo mass. Because *radio mode* feedback is in charge of dumping energy into the hot halo to prevent hot gas from cooling, we see that when it is turned off, this hot gas cools rapidly to form stars at faster rates. As a result, we see significant stellar mass growth in all galaxies at fixed halo mass.

Figure 4.3 shows the stellar mass scatter – computed as half the 16th–84th interpercentile range – at fixed halo mass $\sigma(\log_{10}(M_*|M_h))$ as a function of halo mass. At all halo masses, DARK SAGE galaxies have a

higher scatter in stellar mass than in TNG and roughly all other models. Unlike DARK SAGE, the scatter in TNG is generally constant at ~ 0.2 dex, except at low halo masses where the scatter spikes up. This low scatter prediction is consistent with other hydrodynamical simulations (Khandai et al., 2015; McAlpine et al., 2016), empirical models (Hearin & Watson, 2013; Becker, 2015), and observations from satellite kinematics (More et al., 2011b), galaxy-galaxy lensing (Zu & Mandelbaum, 2015) and X-ray (Kravtsov et al., 2018) measurements. On the other hand, DARK SAGE's scatter almost gets as large as 0.6 dex, which is higher than other semi-analytic models. However, when the *radio mode* is turned off in DARK SAGE, the scatter drops to about 0.2 dex. At the highest halo mass bin, the scatter increases possible due to mergers.

There is further work to be done to help constrain the scatter in stellar mass at low halo masses ($M_h < 10^{11} M_\odot$). It is possible that the increased stellar mass scatter is due to the unrealistic blow-outs of gas in TNG, which leads to overly massive galaxies and low stellar metallicities in their central regions. This is only known to happen for halos with underdense gas (Nelson et al., 2019b). Another possibility is the resolution of the simulation. Figure 8 in Wechsler & Tinker (2018) shows the scatter in stellar mass at fixed halo mass for TNG300 and TNG100. They show that at fixed halo mass for $M_h < 10^{12} M_\odot$, TNG300 galaxies have a larger stellar mass scatter. The scatter difference between the simulations increases up to ~ 0.1 dex with decreasing halo mass. Using MARVEL-OUS DWARFS (Munshi et al., 2019) and DC JUSTICE LEAGUE (Applebaum et al., 2021) zoom-in cosmological simulations, Munshi et al. (2021) finds that galaxies between $M_* \sim 10^{6-9} M_\odot$ and $M_h \sim 10^{8-11} M_\odot$ have a constant scatter in stellar mass of 0.3 dex. In the case of empirical models, at the low halo mass regime, the standard techniques that match galaxies with dark matter halos from cosmological simulations would not be as reliable since the assumption of a nonlinear monotonic relationship between the stellar mass and the halo mass may break. This is important given that there is an explicit degeneracy between the observationally-inferred scatter and the SMHM slope (Garrison-Kimmel et al., 2017). An exploration of the scatter in stellar mass at $M_h < 10^{12} M_\odot$ will follow in future works. We now explore ways to reduce the scatter in stellar mass taking into account the significant contribution of the black hole mass and feedback.

4.5 Black hole seeding and AGN effect on reducing stellar mass scatter

We begin by exploring how black hole formation changes the scatter in stellar mass at fixed halo mass. We present two cases as shown in figure 4.4: the SMBH seeding and the BH–halo mass analytic function (BHMh analytic). For the SMBH seeding case, we allow DARK SAGE galaxies to grow their black holes as they normally do, through gas accretion (see equation 4.1) and mergers (equation **??**) as described in section **??**. However, in this model, we now seed a black hole mass of $10^6\,\mathrm{M}_\odot$ for every halo that reaches $10^{10.5}\,\mathrm{M}_\odot$. DARK SAGE initializes black holes with zero mass in the fiducial run. Here, we are basically mimicking how

TNG treats black hole seeding as described in section 4.3.1.

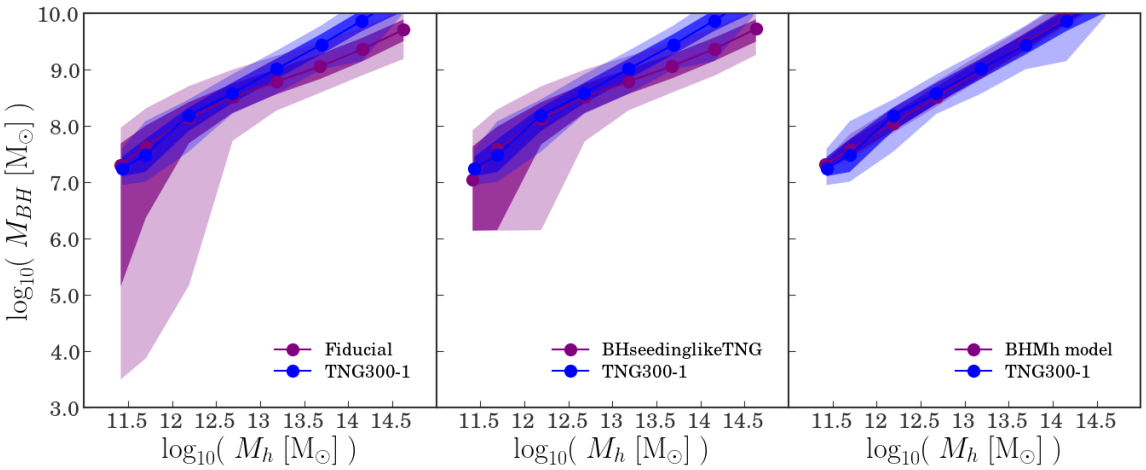

Figure 4.4: Black hole mass as a function of halo mass for DARK SAGE (purple) and TNG (blue) galaxies. In all panels, the blue line is unchanged. The left panel shows fiducial DARK SAGE. The mid panel shows DARK SAGE results when the model seeds black holes like in TNG (i.e. if a halo of $10^{10.5}\,\mathrm{M}_\odot$ does not have a black hole of $10^{6}\,\mathrm{M}_\odot$, then assign one). The right panel shows DARK SAGE galaxies when we apply our black hole mass model, where we force galaxies to follow the black hole mass–halo mass median relation shown in TNG including the following black hole mass scatter values: 0, 0.2, 0.4, 0.7, and 1 dex. In this plot, we only display the black hole mass–halo mass median relation with a black hole mass scatter of 0 dex.

In the case of the BH–halo mass analytic function, we remove any form of black hole growth that fiducial DARK SAGE implements. Instead, we force all black hole masses to follow the median black hole mass–halo mass relation from TNG. DARK SAGE now assigns black hole mass using equation 4.7.

$$\frac{m_{\mathrm{BH}}}{10^{10}\,\mathrm{M}_\odot} = \frac{m_{\mathrm{halo}}^{0.95}}{10^{10}\,\mathrm{M}_\odot} \times 10^{-4.04+x}, \tag{4.7}$$

To control the black hole mass - halo mass scatter, we add x, a random variable normally distributed with mean zero and standard deviation σ_{BH}. We do this to test whether the scatter in stellar mass could change depending on the scatter in black hole mass - halo mass.

Figure 4.4 shows the black hole mass - halo mass relation for DARK SAGE (purple) and TNG (blue) galaxies. In all panels, the blue line is unchanged. The left panel shows fiducial DARK SAGE. The mid panel shows DARK SAGE results when the model seeds black holes like in TNG. The right panel shows DARK SAGE galaxies when we apply our BH–halo mass analytic function, where we force galaxies to follow the black hole mass-halo mass median relation from TNG. Note that this is the run when we select our scatter input to be 0.

Because star formation rate and quenching of a galaxy are strongly tied to black hole feedback, we now turn to dissecting the effect of black hole mass within three different AGN feedback models: DARK SAGE

fiducial AGN feedback, turning off AGN feedback while also turning off cooling for galaxies with black hole masses above $10^8\,M_\odot$, and lastly, doing the former while also removing all the cold gas mass. In the following sections, we analyze how both black hole mass and these three modes of feedback contribute to reducing the scatter in stellar mass.

4.5.1 Fiducial AGN feedback model

In this case, we allow DARK SAGE to prescribe the *radio mode* and *quasar mode* feedback models as described in section **??**. In both seeding cases (adapting SMBH seeding and using the BHMh analytic model), DARK SAGE allows black holes as it does normally to suppress star formation. Figure 4.5 shows the black hole mass–halo mass relation colored by the quenched fraction ($\log_{10}\left(\mathrm{sSFR}\ \left[\mathrm{yr}^{-1}\right]\right) < -11.0$) for DARK SAGE fiducial (top left), TNG (bottom left), SMBH seeding, and several runs of the BHMh analytic function for varyingly imposed scatter. For the BHMh analytic function, we impose a scatter of 0, 0.2, 0.4, 0.7, and 1 dex. *Note that in the results, where AGN feedback is turned on, there is a decoupling between the forced black hole mass and its accretion rate, so, currently, the accretion rate experienced in every black hole is not their instantaneous accretion.*

In the SMBH seeding case, galaxies quench when their black holes reach a mass of $\sim 10^8\,M_\odot$, in similar agreement with fiducial DARK SAGE and TNG galaxies. In the case of the BHMh analytic model, both black hole mass and halo mass contribute to suppressing star formation. Interestingly, a population of high-mass black holes that live in low-mass halos that are star-forming emerge and become more apparent for larger σ_{BHM} values. Because low-mass black holes are assigned to low-mass halos, these high-mass black holes have been around for quite some time, but not enough to start their high-accretion rates. These black holes acquire mass rapidly through mergers and *quasar mode* feedback without triggering *radio mode* efficiently. This is probably because the virial temperatures are low, which causes the suppression of AGN accretion rate and *radio mode* feedback. Since *quasar mode* does not do much to regulate quenching like *radio mode* does, then we get star-forming galaxies with massive black holes that live in low-mass halos. One thing to keep in mind is that this population of galaxies are at the tails of the median distribution. Their stellar masses range from $10^{9-11.5}\,M_\odot$ and those with massive black holes are few in comparison to the whole sample. As the scatter in black hole mass–halo mass increases, galaxies start to become less physical, and the black hole mass-stellar mass median relation flattens.

We see the effect of these black hole seeding cases and feedback model within the stellar-to-halo mass relation. Figure 4.6 shows this relation colored by the quenched fraction. The layout of the plot is just like in figure 4.5. We find that the overall scatter in stellar mass is not reduced by the change in black hole seeding for this particular feedback model. We do notice an increase in the stellar mass scatter when increasing the

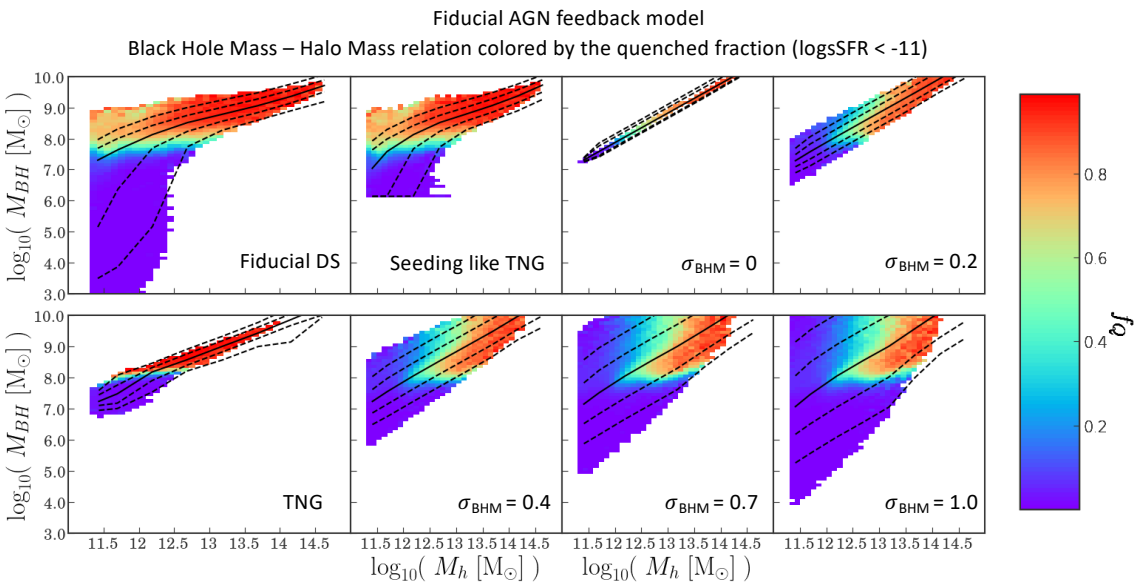

Figure 4.5: Fiducial AGN feedback model: Black hole mass as a function of halo mass colored by the quenched fraction ($\log_{10}\left(\mathrm{sSFR}\ \left[\mathrm{yr}^{-1}\right]\right) < -11.0$) for DARK SAGE fiducial (top left), TNG (bottom left), SMBH seeding and several sigma runs with a forced BHMh analytic function. For the BHMh analytic case, we assume a scatter of 0, 0.2, 0.4, 0.7, and 1 dex. In the case of SMBH seeding, the quenching transition happens around a black hole mass of $10^8\,\mathrm{M}_\odot$, like in DARK SAGE fiducial and TNG. In the case of the BH–halo mass analytic function, both black hole mass and halo mass contribute to suppressing star formation.

scatter in black hole mass. The same blue strip in the upper part of the stellar-to-halo mass relation in the BHMh analytic models shows up, increasing with larger black hole mass scatter values.

To examine closely the change of scatter in stellar mass, we look at the scatter in black hole mass. Figure 4.7 presents the stellar mass scatter at fixed halo mass ($\sigma(\log_{10}(M_*|M_h))$) as a function of black hole mass scatter at fixed halo mass ($\sigma(\log_{10}(M_{BH}|M_h))$). Each purple line with dots show the different narrow halo mass bins. The purple squares and stars show DARK SAGE fiducial and SMBH seeding data respectively. The blue triangles show TNG data. In all data points, the bolder the color, the higher the halo mass bins. Lastly, the black line is a one-to-one line.

For the BH–halo mass analytic function, we find that changing the scatter in black hole mass increases the stellar mass scatter at all halo mass bins. We see that low-mass halos have the largest stellar mass scatter of about 0.8 to 1, whereas the highest halo mass bins stay around $0.2-0.3$ dex, which are in constant agreement with the DARK SAGE fiducial and SMBH seeding cases. The latter model surprisingly tracks well the former, even if the lowest halo mass bin has a black hole scatter difference of about 0.4 dex. This suggests that adapting SMBH seeds does not play a significant effect in reducing the scatter in stellar mass, as shown previously in figure 4.6. Lastly, we see how TNG galaxies compare with all models, yielding the lowest stellar mass and black hole mass scatter of all. These results show that modifying the black hole formation

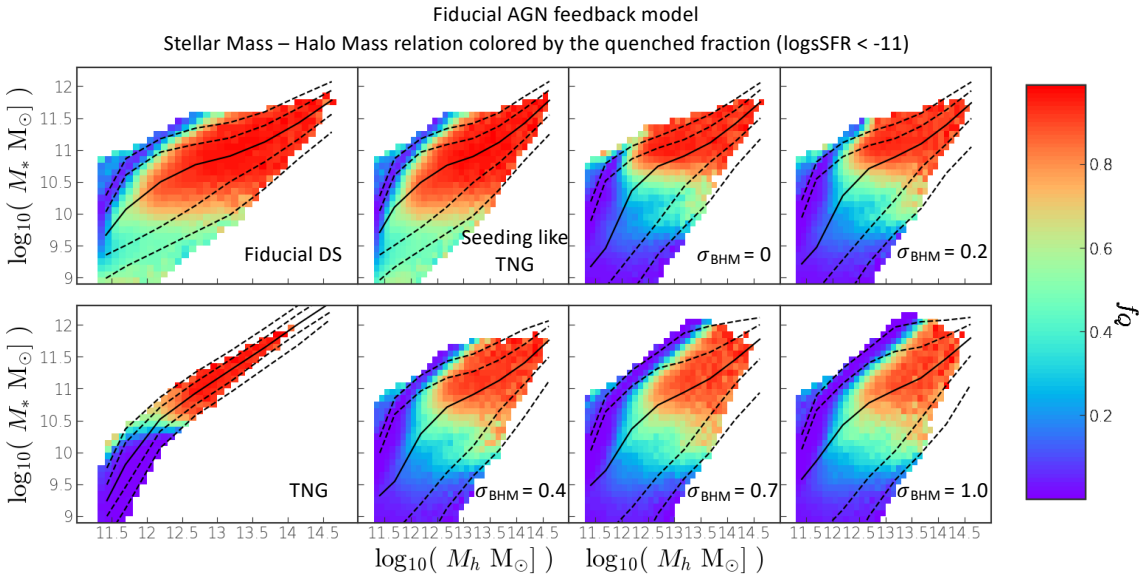

Figure 4.6: Fiducial AGN feedback model: Stellar-to-halo mass relation colored by the quenched fraction for the same black hole models as in Figure 4.5. We find that the overall scatter in stellar mass is not reduced by the change in black hole seeding for this particular feedback model. We do notice an increase in the stellar mass scatter when increasing the scatter in black hole mass.

channels in DARK SAGE is not enough to decrease the scatter in stellar mass down to 0.2 dex. For this reason, the next step is to do a modification to the AGN feedback in DARK SAGE to understand explore whether the scatter in stellar mass could be reduced.

4.5.2 No AGN and turning off cooling for galaxies with black hole masses above $10^8\,M_\odot$

We now introduce a new AGN feedback model that approximates the output of TNG's quenched fraction at $z = 0$. We turn off AGN feedback in DARK SAGE fiducial and force galaxies with black hole masses above $10^8\,M_\odot$ to stop cooling. We specifically chose the $10^8\,M_\odot$ black hole mass threshold because of the sharp quenching transition around that mass seeing in figure 4.8. In this figure, we see small differences in the quenching fractions in comparison to figure 4.5. In particular, the black hole mass-halo mass sigma run of 0.2 dex shows the closest resemblance to the TNG black hole mass-halo mass relation in terms of scatter and transition of the quenched population when looking at the quenched fractions.

We then see how this translates to the stellar mass-to-halo mass relation in figure 4.9. We see that the scatter in stellar mass is significantly reduced when adopting the black hole mass seeding like TNG and when choosing low scatter values within the black hole mass-halo mass relation. For the black hole mass-halo mass scatter runs above 0.4 dex, the scatter in stellar mass starts to increase. Additionally, interestingly, the low-mass black hole population in massive stellar mass galaxies (as seen in figure 4.6) are still present for the

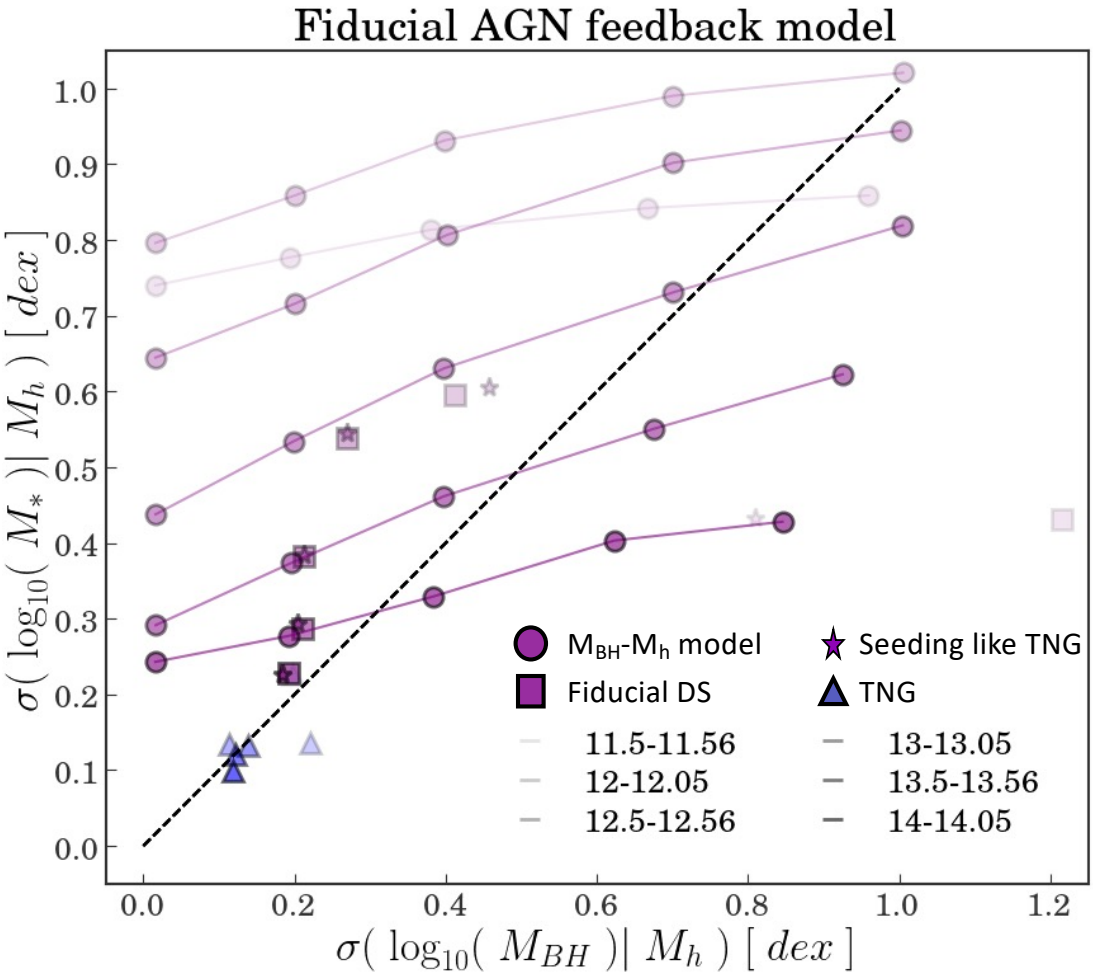

Figure 4.7: The stellar mass scatter at fixed halo mass ($\sigma(\log_{10}(M_*|M_h))$) as a function of black hole mass scatter at fixed halo mass ($\sigma(\log_{10}(M_{BH}|M_h))$. Fiducial AGN feedback model, where the only change we make is the way black holes masses are calculated. Each purple line with dots show the different narrow halo mass bins. The purple squares and stars show DARK SAGE fiducial and SMBH seeding data respectively. The blue triangles show TNG data. In all data points, the bolder the color, the higher the halo mass bins. Lastly, the black line is a one-to-one line. When seeding SMBH DARK SAGE, there is no significant difference in the scatter in stellar mass. However, when implementing the MBH-Mh analytic function, we find that the low black hole mass scatter yields lower stellar mass scatter.

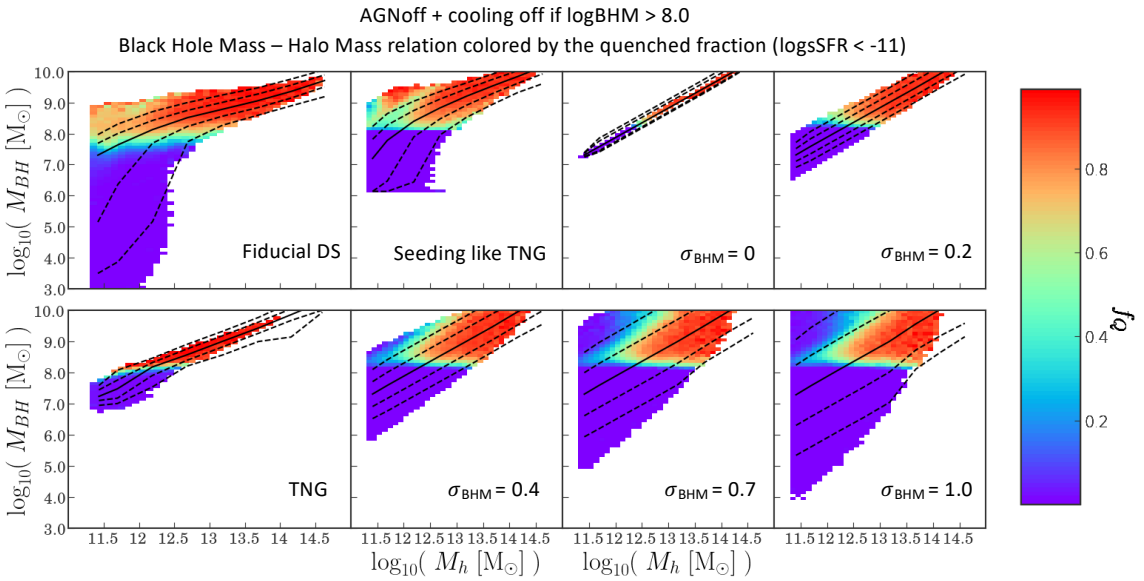

Figure 4.8: Black hole mass as a function of halo mass colored by the quenched fraction for the same black hole models as in Figure 4.5. We see small differences in the quenching fractions in comparison to figure 4.5 although the black hole mass–halo mass sigma 0.2 dex run best resembles TNG prediction in terms of scatter and quenched fraction transition.

seeding like TNG model and the large sigma runs using the black hole mass-halo mass run. This causes the quenching of these galaxies to be both stellar mass (and thus black hole mass) and halo mass driven. The quenching within galaxies following the black hole mass-halo mass relation that have 0 and 0.2 dex scatter become halo mass driven.

We dissect the effect of this AGN quenching model by looking at the scatter in stellar mass as a function of the scatter in black hole mass (Figure 4.10). When adapting different black hole seeding, we see a significant reduction in the scatter in stellar mass at all halo mass bins, except at the highest. For the BH–halo mass analytic function, around the halo quenching mass and below, we can reduce the scatter in stellar mass by controlling for the scatter in black hole mass. The most abrupt change in the scatter in stellar mass takes place for the lowest halo mass bin, which is reduced to 0.1 dex in scatter stellar mass at a black hole mass scatter of 0 dex, but it may increase up to 0.5 dex in stellar mass when the black hole mass scatter reaches 1 dex. For the highest halo mass bin, regardless of which black hole mass scatter value we choose, the scatter in stellar mass seems to be almost unaffected. In the case of SMBH seeding, the lowest halo mass bins be have a reduced stellar mass scatter of 0.2 dex but at the expense of having a black hole mass scatter of close to 1 dex. Interestingly, this model follows DARK SAGE fiducial stellar mass and black hole mass scatter values until it reaches the 0.4 dex intercept. Thereafter, DARK SAGE fiducial continues to increase in both stellar and black hole mass scatter, whereas, in the SMBH seeding model, the scatter in stellar mass diminishes

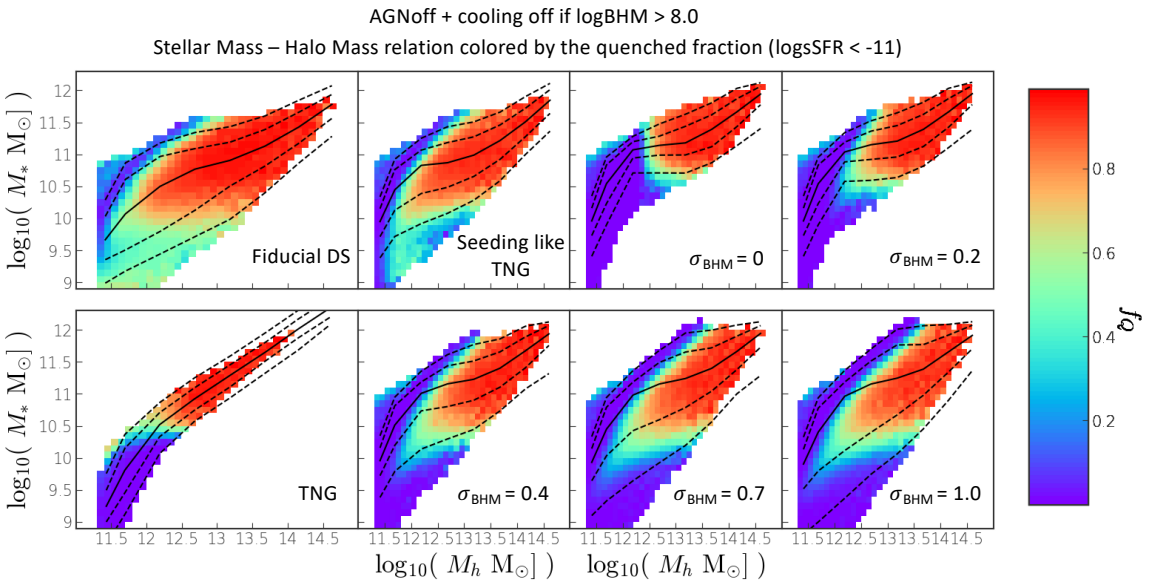

Figure 4.9: AGNoff and cooling off for galaxies with black hole mass above $10^8\,M_\odot$: Stellar-to-halo mass relation colored by the quenched fraction for the same black hole models as in Figure 4.5. We see that the scatter in stellar mass is significantly reduced when adopting the SMBH seeding and when choosing low scatter values within the black hole mass-halo mass relation.

with increasing black hole scatter. Lastly, the BH–halo mass analytic function is the only one that reduces the stellar mass scatter significantly enough to match TNG predictions although it still fails to do so for the higher halo mass bins.

4.5.3 No AGN, turning off cooling, and removing cold gas resevoir for galaxies with black hole masses above $10^8\,M_\odot$

The last AGN quenching model we test is adapting the same model as in section 4.5.2 (i.e. turning off AGN feedback in DARK SAGE and cooling) while also removing all cold gas mass for galaxies with black hole masses above $10^8\,M_\odot$. Figure 4.11 shows the effect of this AGN quenching model for both of our black hole seeding runs. We see the sharpest quenching transition of all AGN quenching models, where everything right above black hole masses above $10^8\,M_\odot$ is quenched. This is true for the SMBH seeding model as well as all the sigma runs done using the BH–halo mass analytic function.

We explore how this AGN quenching model affects the stellar mass-to-halo mass relation. Figure 4.12 shows that galaxies at all masses are significantly affected by this aggressive quenching model. We see that the scatter in stellar mass is significantly reduced like in figure 4.9, but there are also fewer galaxies in transition from being active to passive. We also see a strong strip of star-forming galaxies, especially in the large scatter values of the BH–halo mass analytic function, as seen in figure 4.9. Like mentioned before,

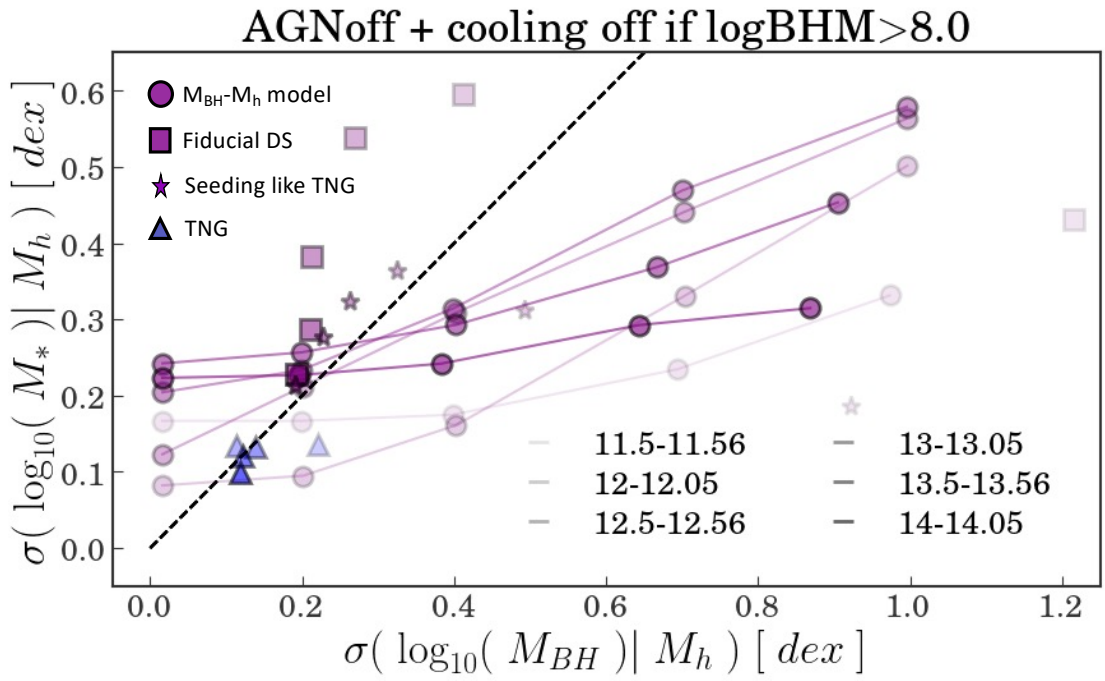

Figure 4.10: Same as Figure 4.7, except that in this model, we turn off AGN feedback and turn off cooling for galaxies with black hole masses above $10^8\,M_\odot$. When adapting different black hole seeding, we see a significant reduction in the scatter in stellar mass at all halo mass bins, except at the highest.

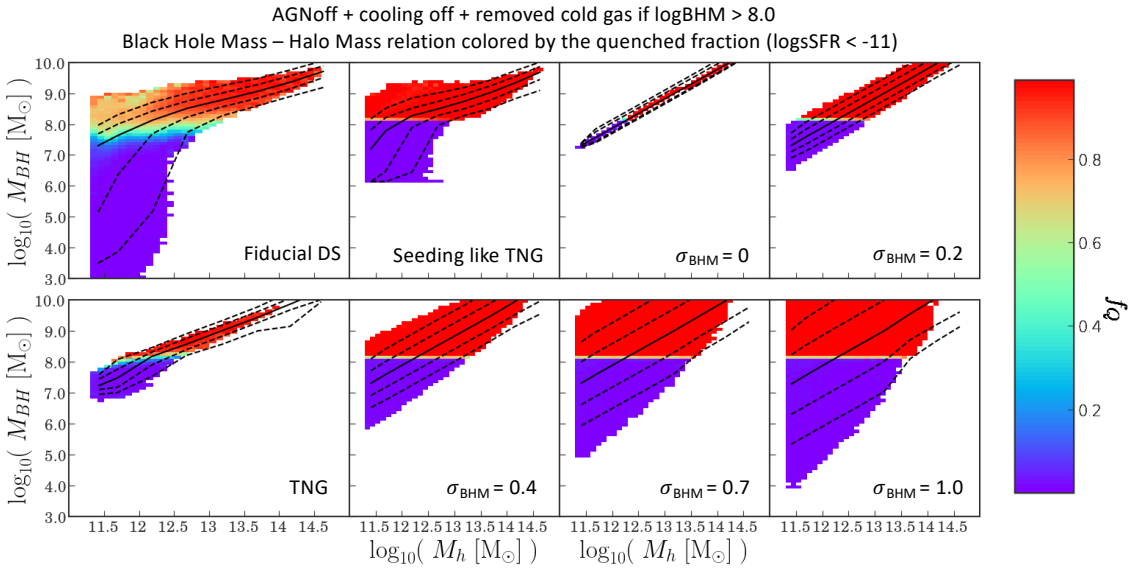

Figure 4.11: No AGN, turning off cooling, and removing cold gas resevoir for galaxies with black hole masses above $10^8\,M_\odot$: Black hole mass as a function of halo mass colored by the quenched fraction for the same black hole models as in Figure 4.5. We see the sharpest quenching transition of all AGN quenching models, where everything right above black hole masses above $10^8\,M_\odot$ is quenched.

these galaxies have low-mass black holes that have not grown significantly, which is a result of having turned off AGN feedback in the model given that *quasar mode* feedback contributes significantly to the growth of black holes in the model.

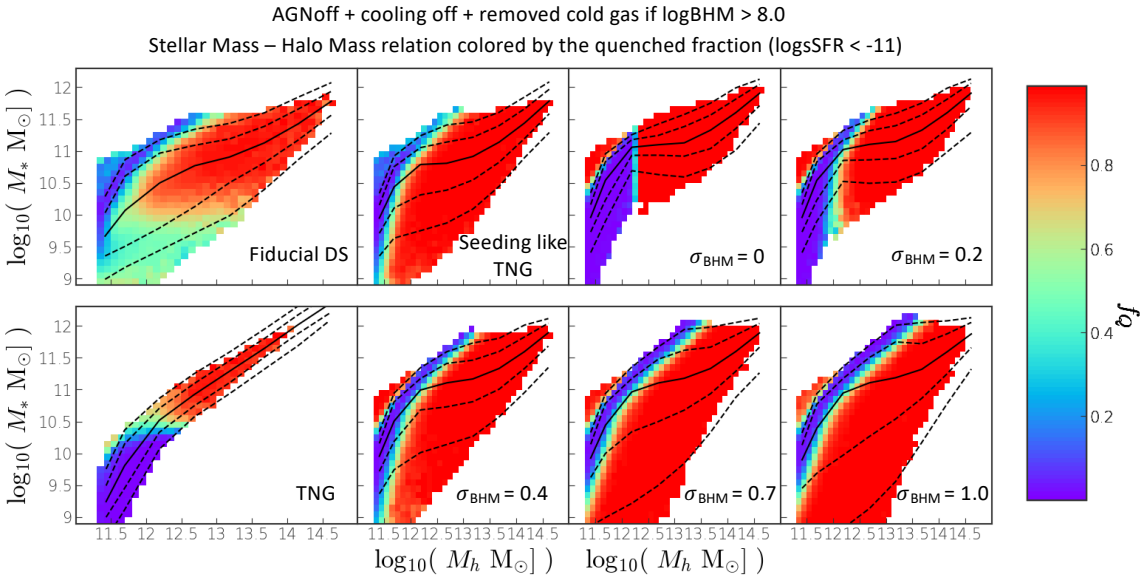

Figure 4.12: No AGN, turning off cooling, and removing cold gas resevoir for galaxies with black hole masses above $10^8\,M_\odot$: Stellar-to-halo mass relation colored by the quenched fraction for the same black hole models as in Figure 4.5. We see that the scatter in stellar mass is significantly reduced like in figure 4.9, but there is also less galaxies in transition from being active to passive.

Lastly, we take a look more closely at how this aggressive quenching affects the scatter in stellar mass when controlling for the scatter in black hole mass. Like in figure 4.10, we see a significant reduction in the scatter in stellar mass at all halo mass bins, except at the highest. For the BH–halo mass analytic function, around the halo quenching mass and below, the scatter in stellar mass is significantly reduced by controlling for the scatter in black hole mass. However, in this case, as we increase in black hole mass scatter, the scatter in stellar mass is slightly higher than in figure 4.10. It is in the case of this and all other quenching models that the stellar mass scatter in galaxies that are the highest halo mass bin was not able to be reduced.

In the case of SMBH seeding, like in figure 4.10, the lowest halo mass bins be have a reduced stellar mass scatter of 0.2 dex but at the expense of having a black hole mass scatter of close to 1 dex. This model still tracks DARK SAGE fiducial prediction although still predicting lower stellar mass scatters with the highest being of 0.4 dex at a black hole mass scatter of 0.2 dex, a lower black hole mass scatter than in figure 4.10.

4.5.4 The effect of quenching models in reducing the scatter in stellar mass

We compare the effects of sections 4.5.1, 4.5.2, and 4.5.3 for both SMBH seeding and the BHMh analytic function. Figure 4.14 shows the scatter in stellar mass at fixed halo mass for the SMBH seeding at different

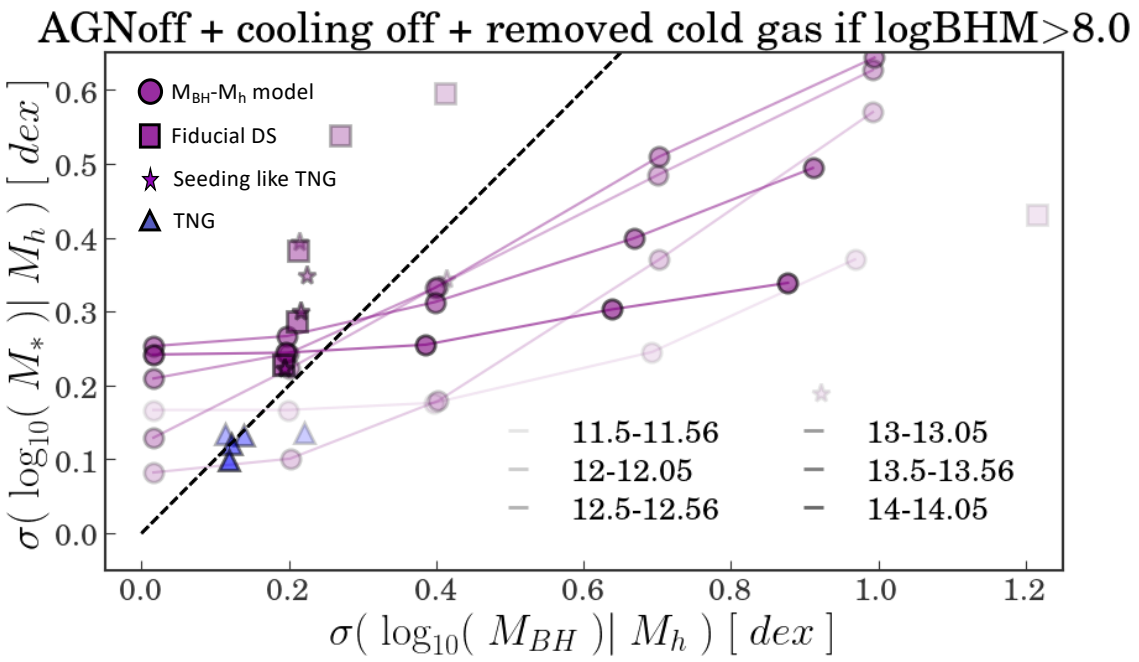

Figure 4.13: Same as Figure 4.10, except that in this model, we also remove all cold gas resevoir for galaxies with black hole masses above $10^8\,M_\odot$. Although the scatter in stellar mass is significantly reduced like in figure 4.10, the scatter in stellar mass is slightly higher as we increase black hole mass scatter.

halo mass bins for the three different AGN feedback models: DARK SAGE fiducial AGN feedback, turning off AGN feedback while also turning of cooling for galaxies with black hole masses above $10^8\,M_\odot$, and lastly, doing the former while also removing all the cold gas mass. We compare the stellar mass scatter results with DARK SAGE fiducial and TNG. Here, the bolder the color the higher the halo mass bins.

We find that a) adapting the SMBH seeding and using DARK SAGE fiducial AGN feedback does little to change the scatter in stellar mass, b) turning off AGN feedback while also turning of cooling for galaxies with black hole masses above $10^8\,M_\odot$ reduces the scatter in stellar mass the most for galaxies with halos around the quenching mass and below, and c) neither of the three AGN quenching models affects the scatter in stellar mass at the highest halo mass bins. Even though the scatter in stellar mass was able to be reduced in some cases for the lower halo mass bins, the scatter in stellar mass could not be reduced as low as TNG predicts.

In the case where we force galaxies in DARK SAGE to follow the black hole mass-halo mass median relation in TNG, we find that the scatter in stellar mass can be reduced even more than in the SMBH seeding model. Figure 4.15 shows the scatter in stellar mass at fixed halo mass for the BH–halo mass analytic function at different halo mass bins for the three quenching models described above. We compare the stellar mass scatter results with DARK SAGE fiducial and TNG. Here, the bolder the color the higher the halo mass bins. We see that the SMBH seeding model that uses DARK SAGE fiducial AGN feedback does not

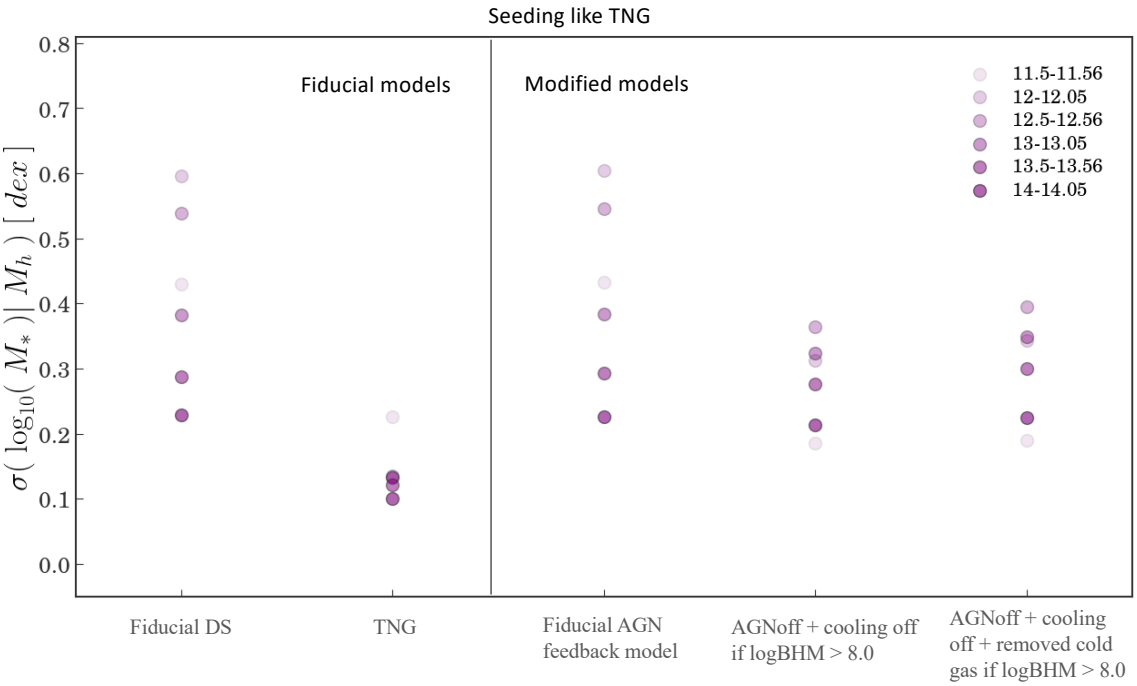

Figure 4.14: Black halo seeding like TNG: The stellar mass scatter at fixed halo mass ($\sigma(\log_{10}(M_*|M_h))$) at different halo mass bins for three different quenching models: DARK SAGE fiducial AGN feedback, turning off AGN feedback while also turning off cooling for galaxies with black hole masses above $10^8\,M_\odot$, and lastly, doing the former while also removing all the cold gas mass. We compare the stellar mass scatter results with DARK SAGE fiducial and TNG. Here, the bolder the color the higher the halo mass bins.

change significantly the scatter in stellar mass compared to DARK SAGE fiducial. On the other hand, in the MBHMh analytic case also using fiducial AGN feedback, the scatter increases significantly, reaching stellar mass scatters as high as 0.8 dex.

However, when turning off AGN feedback while also turning off cooling for galaxies with black hole masses above $10^8\,M_\odot$, the stellar mass scatter is strongly decreased, reaching values as low as 0.1 dex for the lowest halo mass bins. The flip in the highest to lowest stellar mass scatter for the lowest halo mass bins when comparing the former and the latter quenching models is due to the lack of the contribution of AGN feedback to the overall galaxy population. In the case of our quenching model, we are only quenching galaxies with black hole masses above $10^8\,M_\odot$ essentially not treating galaxies with black holes below that mass to have any form of quenching. We have seen that the contribution to the *radio mode* feedback is so significant that by turning it off, we can get scatters lower than 0.2 dex (see figure 4.3). The result of turning off AGN feedback results in galaxies around the quenching mass and below to have lower stellar mass scatter. When comparing this quenching model with the most aggressive form of quenching, which removes cold gas resevoir from galaxies, we see that the scatter in stellar mass is not significantly different. Yet again, an interesting finding is that like in the SMBH seeding model, neither of the three AGN quenching models affects the scatter in stellar mass at the highest halo mass bins. However, for halo masses lower than quenching mass, the scatter in stellar mass was able to be reduced as low as TNG predicts.

4.6 Discussion

One of the most fundamental questions in galaxy formation relates to quantifying scatter at a given halo mass. In this paper, we consider the scatter in the stellar mass at fixed halo mass for central galaxies. Here, we present some points of discussion regarding our results.

4.6.1 Models' effect on the stellar mass function

The shape of the stellar mass function (SMF) can affect the slope of the SMHMR. If the stellar mass scatter at a given halo mass is not constant, how steep the SMHMR is could also potentially affect the scatter in stellar mass. Overall, the stellar mass functions from DARK SAGE fiducial and TNG agree with observations. However, both simulations are calibrated using different SMFs, which we hypothesize make the difference in the SMHMR slope. DARK SAGE uses Baldry et al. (2008) stellar mass function, which cuts down just below $10^{12}\,M_\odot$, whereas TNG uses Bernardi et al. (2013), a sample with few more massive galaxies above $10^{12}\,M_\odot$ (Pillepich et al., 2018). This difference in SMFs is more apparent for stellar mass galaxies above $10^{11}\,M_\odot$. Besides both models disagreeing on the stellar mass scatter, TNG has a constant scatter with increasing halo mass, unlike DARK SAGE fiducial, which decreases sharply. At fixed halo mass of $10^{14.0}\,M_\odot$, the median

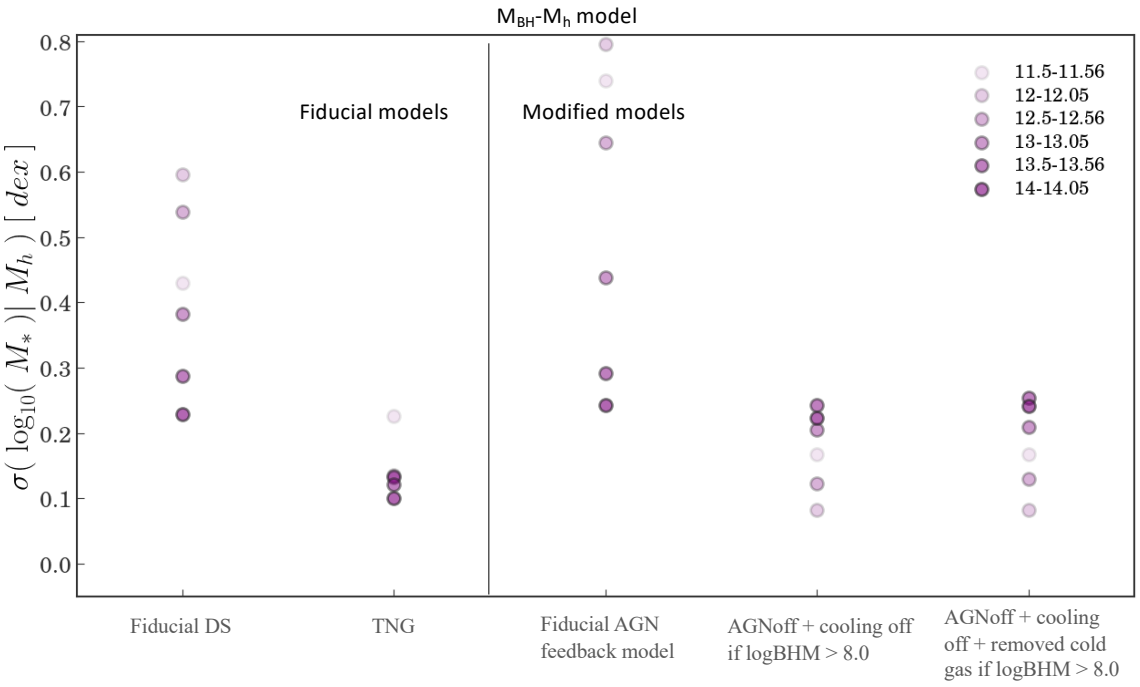

Figure 4.15: BH–halo mass analytic function assuming $\sigma(\log_{10}(M_{BH}|M_h)) = 0.0$: The stellar mass scatter at fixed halo mass at different halo mass bins for three different quenching models described above. We compare the stellar mass scatter results with DARK SAGE fiducial and TNG. Here, the bolder the color the higher the halo mass bins.

stellar mass in DARK SAGE fiducial is $\sim 10^{11.0}\,\mathrm{M}_{\odot}$, as opposed to in TNG, where at that same halo mass, we see the stellar mass median between $10^{11.5-12}\,\mathrm{M}_{\odot}$. After including the SMBH seeding model and the BH–halo mass analytic function in DARK SAGE, we find that the SMF changes depending on the different modes of black hole growth and AGN feedback we adapt. It's worth pointing out that these are therefore not fully viable models of galaxy formation.

One possible source of bias, when comparing simulations results with observations of the stellar mass scatter at fixed halo mass, is the binwidth used to measure the scatter in stellar mass in the observed data. In other words, the scatter in stellar mass might appear larger or smaller than the simulation results because of the way the observed data is binned. Therefore, we must take this into consideration when comparing the scatter in the simulation results with observations.

4.6.2 Exploring the parameter space to reduce the scatter

Using the black hole mass-halo mass analytic function, we create an idealized case where DARK SAGE galaxies follow a black hole mass-halo mass relation with zero black hole mass scatter. Even in such restrictive form, DARK SAGE produces a stellar mass scatter that is larger than in TNG, in some cases by a factor of 3

at the lowest halo masses (see Figure 4.7). As a result, even if we modify one of the primary potential sources of the stellar mass scatter in DARK SAGE, the model shows a stellar mass scatter that is physically produced in the simulation.

Another important point is that not all forms of feedback contribute to reducing the stellar mass scatter. When turning off *quasar mode* and stellar feedback, the scatter in stellar mass is not affected by much. This provides more information about the importance of *radio mode* feedback modifications to reduce the stellar mass scatter in SAMs.

One can argue that in a SAM, there are different ways to reduce the scatter without changing the AGN feedback prescription. One way is to modify the cooling time so that the transfer of gas from the CGM reservoir to the ISM could take longer. Delaying the entry of the cooling gas entering the ISM would allow more massive galaxies to quench based on its current AGN feecback prescription. Another way is to modify the stellar feedback in the SAM. First, supernova explosions can inject energy and momentum into the interstellar medium, causing the gas to heat up and expand. This can lead to the formation of large-scale outflows that can expel gas from the galaxy, reducing the amount of gas available for star formation. On the one hand, outflows can reduce the amount of gas available for star formation, leading to a lower stellar mass. On the other hand, outflows can also redistribute gas within the galaxy, allowing it to form stars in different locations or at different times. This can lead to a higher scatter in the stellar mass, as galaxies that experience strong outflows may have lower overall stellar masses, but a wider range of star formation histories and locations within the disk.

Varying the star formation efficiency may not reduce the scatter in stellar mass alone. This scatter is highest around the quenching mass, which indicates that AGN feedback is primarily responsible for the large scatter in stellar mass. After performing a simple experiment where we turn off *radio mode* feedback, we find how the scatter in stellar mass at fixed halo mass was significantly affected. This result alone points towards a common problem in how SAMs are regulating feedback and how its energy is being distributed to the CGM.

4.6.3 Future work

Figure 4.3 shows that for some models, the scatter in stellar mass reaches above 0.2 dex for halos below $10^{12}\,\mathrm{M}_{\odot}$. An interesting future analysis is to explore whether this increase is due to resolution effects from the simulation. Using zoom-in cosmological simulations, Munshi et al. (2021) find that, in general, for all galaxies below halo masses of $10^{11}\,\mathrm{M}_{\odot}$, their stellar mass scatter remains constant around 0.3 dex. Because these zoom-in cosmological simulations have well-resolved halos, the fact that some of this large box simulations showing an exponential increase of the stellar mass scatter at low-mass halos may indicate that resolution plays an important role (see TNG and TNG100 in figure 8 from Wechsler & Tinker (2018)).

Another interesting question revolves around the effect of our black hole mass and feedback models in the active and passive galaxy populations. Matthee & Schaye (2019) compare SDSS observations and EAGLE simulated data to show that the scatter in star formation rate at fixed stellar mass revolves between $0.3 - 0.5$ dex for star-forming galaxies at $z = 0$. Exploring how our model that agrees with the observed scatter in stellar mass does in terms of predicting the scatter in star formation rate for star-forming galaxies may contribute to understanding the effect of black hole mass and feedback in the star-forming population evolution.

4.7 Conclusion

We explore the contribution of black hole mass and AGN feedback to the stellar mass scatter within the stellar mass-to-halo mass relation using the semi-analytic model DARK SAGE. We use two black hole formation models that approximate TNG's black hole formation and feedback. For the first model, we seed a black hole mass of $10^6\,M_\odot$ for every halo that reaches $10.5\,M_\odot$(section 4.3.1). For the second model, we remove any form of black hole growth that fiducial DARK SAGE implements. Instead, we force all black hole masses to follow the median black hole mass - halo mass relation from TNG. DARK SAGE now assigns black hole mass using equation 4.7. Additionally, we include an input scatter parameter to control the black hole mass - halo mass scatter. We do this to test whether the scatter in stellar mass could change depending on the scatter in black hole mass - halo mass.

Our results are summarized as follows:

- We find that when we turn off radio mode feedback, the scatter in stellar mass at fixed halo mass reduces significantly at all halo masses.
- DARK SAGE fiducial AGN feedback mode: we find that the overall scatter in stellar mass is not reduced by the change in black hole seeding for this particular feedback model. For the BH–halo mass analytic function, we find that by controlling for the scatter in black hole mass, the scatter in stellar mass is not reduced. On the contrary, the effect strongly increases the scatter.
- No AGN, turning off cooling for galaxies with black hole masses above $10^8\,M_\odot$: when adapting different black hole seeding, we see a significant reduction in the scatter in stellar mass at all halo mass bins, except at the highest. For the BH–halo mass analytic function, around the halo quenching mass and below, we can reduce the scatter in stellar mass by controlling for the scatter in black hole mass.
- No AGN, turning off cooling, and removing cold gas resevoir for galaxies with black hole masses above $10^8\,M_\odot$: even by removing the cold gas reservoir, the scatter in stellar mass was not significantly reduced in comparison with the previous quenching model.

- In all three quenching models mentioned above, the stellar mass scatter in galaxies at the highest halo mass bin was not able to be reduced.

Future work involves looking at exploring the effects of resolution from simulations for predicting the scatter in stellar mass for $M_h < 10^{12} M_{\odot}$. In the case of DARK SAGE fiducial, it is important to understand whether the low-mass black holes that live in massive stellar mass galaxies should have any adjustment to their feedback mechanisms that would allow them to quench the star formation of their host galaxy.

CHAPTER 5

Towards a more diverse and inclusive astronomy field

In 2016, I started the Costa Rica - US Bridge program, mentoring 6 students from the Universidad de Costa Rica, because in Costa Rica, the opportunities to do astrophysics research are not many. As I learned about how other neighboring countries experienced similar or worse situations, I decided to switch the focus to Central American and the Caribbean to support and develop astronomy research opportunities in the region. The program took off with the co-leadership of Gloria Fonseca Alvarez and Valeria Hurtado Urrutia who joined as co-leaders, allowing the three of us to make important decisions about the future of Central America and Caribbean astronomy. On June 2022, we co-founded the Central American-Caribbean Bridge in Astrophysics (Cenca Bridge Inc.), an established nonprofit organization in the state of Tennessee with over 100 undergraduate students from Central America and the Caribbean. On December 2021, we were awarded 21,000 euros of funding for 3 years through the International Astronomical Union (IAU) Office for Astronomy Development (OAD). The funds are currently being used to pay undergraduate students who participate in the Cenca Bridge remote internship program. The students will participate in professional development, computational, and social justice workshops. Those components are essential to the foundation of early-career astronomers.

Co-leading the Cenca Bridge organization is so unique because prior to today, there has never been an entity that provides support to marginalized students across all intersectional identities who are interested in astrophysics from Central America and the Caribbean. We are upfront about bridging not only Central American and Caribbean undergraduate students to astrophysics, but also putting an emphasis on social justice issues within the region. Historically, this has not been easy, given the amount of work it takes to run such an organization. To my knowledge, there are only a handful of organizations worldwide that simultaneously center their focus on social activism, science, and mentoring.

5.1 Motivation: the need for this work

Caribbean and Central American countries have struggled to keep a continuous unified collaboration that propels astrophysics to move forward. Collaborations of Central American astronomers emerged in the 1990s up until the early 2000s when the Astronomical Observatory of Honduras was created with the purpose of fostering academic international relations between neighboring countries (de Pineda Carias, 2004). Writing this section, I will convince the reader of the alarming status of astronomy in Central America and the Caribbean by laying out three main points briefly discussed in Montero-Camacho & Castillo-Fallas (2021):

- **No PhD programs in Astrophysics:** Although out-of-date, Levato (2007) presents the statistics on

the number of PhD programs in Astrophysics in Latin America. Their focus is solely Mexico and South America because back in 2007, the number of PhD programs in Astrophysics in Central America and the Caribbean were null, just like in the present 2023. Based on my findings, a handful of countries in Central America and the Caribbean (Costa Rica, Jamaica, Trinidad and Tobago, Puerto Rico, Honduras) have one university that offers a Master's degree in physics with a concentration in Astrophysics.

- **No sustainable infrastructure for growth:** With the exception of Puerto Rico prior to the collapse of the Arecibo Observatory, there is little-to-no governmental financial support. Because of this, there are few opportunities to do research in astrophysics, and thus, no jobs to hire any level of astronomer from postdoctoral to staff scientist. Because of the lack of resources, there is little-to-no high computing facilities, observational telescopes, or access to data. Established astronomers from the Universidad de Costa Rica (UCR) created collaborations with institutions from Mexico like the Instituto Nacional de Astrofisica, Optica, y Electrónica (INAOE), Universidad Nacional Autonoma de Mexico (UNAM), which propelled to the development of the Radio Observatory of Santa Cruz (ROSAC) in Guanacaste, Costa Rica. Many established astronomers from UCR alongside, the Universidad Nacional Autonoma de Honduras (UNAH), and Universidad de San Carlos de Guatemala (USAC) come from Mexican astronomy institutions. Through this connection, the doors opened for undergraduates from these countries to participate in the astronomy summer school: Escuela de Astronomia Observacional para estudiantes Latinoamericanos (ESAOBELA). The lack of resources is not uniform, as there are some countries that have better opportunities than others in terms of Astrophysics research, but the challenge remains as there are many areas of astronomy not being represented.

- **Who gets to be an astronomer:** Even with the limited resources to become an astronomer, the ones that make it either start their undergraduate in their country and leave for graduate school or leave their country after high school. For example, Jarquin-Solis et al. (2022) shows a breakdown of the number of students that come to the U.S. to complete a PhD (49 PhD students) and a post doctoral study (25 scientists) across all sciences from Costa Rica. Historically, I will be the sixteenth person from Costa Rica to obtain a PhD in Astrophysics according to the Costa Rican National Academy of Sciences database. In Costa Rica, which is considered to have some advantages in the development of scientists due to infrastructure, the accessibility to the opportunities to be a scientist in general is low. Additionally, the pool of students that get the opportunity to do astrophysics is generally not representing a population of marginalized students within the country. In general, low-income, disabled, nonbinary, black, and indigenous students (with one or multiple of these identities) are either driven out of the

field, not understood within the academic spaces, a similar issue which marginalized students face in the US (although not the same as social issues within each country may be similar and different).

Cenca Bridge works on tackling some of these important issues. We emphasize social justice to reduce social inequalities, promote diversity and equality in gender, race, and all intersectional identities. Exposing students to astronomy research provides students professional development and programming skills that are transferable to increase employment options. My contribution to Cenca Bridge is extensive because of the impact it made this far within the community.

5.2 My contributions

My experience at Cenca Bridge has been co-founding the remote internship program, co-organizing the remote internship (applications, selection, advisor and mentor search, creating surveys, scheduling multiple meetings per month, final presentations), coordinating monthly webinars, organizing yearly computational and professional development workshops, maintaining the website, writing grants and reports, finding collaborations, and mentoring students. I have personally mentored 15 students: 8 of them whom are in masters and PhD programs in astrophysics and 4 of whom have started their own science mentoring programs: Society of Women in Space Exploration in Costa Rica and Honduras, Uranus Haiti, and the National Radio Astronomy Observatory National and International Non-Traditional Exchange (NRAO-NINE) hub Costa Rica.

I am also the co-founder of Alpha-Cen, a nongovernmental organization led by established Central American astronomers with the goal to connect students from Central America interested in astronomy to overseas opportunities. I was part of the executive committee for 4 years. My main accomplishment here was to establish a formal collaboration with the National Radio Astronomy Observatory (NRAO). This opened the opportunity for Alpha-Cen to send students to the U.S. to participate in the NRAO-NINE program. This program requires students to establish hubs within their countries. Currently, there are hubs in Honduras, Costa Rica, and Haiti.

Since 2015, I have been part of the National Astronomy Consortium (NAC) community at NRAO. I have mentored several NAC alums, participated in the program committee to develop webinar series highlighting astronomy research work, and co-organized three annual NAC conferences[1].

5.3 Mentoring philosophy

My mentoring philosophy involves three main components: establishing trust, advocating, and guiding. I establish trust by understanding the life of mentees within and outside of academia. I ask about their motivations, expectations, and life in general. I guided students to astronomy summer school and research

[1] 2020 NAC VIII conference, 2021 NAC IX, 2022 NAC X

internship opportunities outside of their countries. I read their application essays and stayed alongside the whole application process. For times in which opportunities did not help with visa related issues, we worked together providing pertinent information to the embassy. To advocate for the mentee, I introduced them to my networks, while highlighting their work during my conference travels.

The impact I measure is based on my own mentoring philosophy because every person I work with has their own way of mentoring. My mentor–mentee experience had a large impact on students' personal and academic lives. Mentees that I have closely mentored have exponentially grown scientifically and personally. Besides having entered a graduate program in astronomy, mentees have developed their own mentorship programs in space exploration and radio astronomy fields. These students are actively involved in Cenca Bridge, becoming mentors for new students as well as in their own programs. We collaborate within organizations, sharing resources, developing workshops, and exchanging students to mentor. These are some of the elements that make our mentorship relationship mutually beneficial.

I adopted my mentoring views from models used in the National Astronomy Consortium (NAC) program as part of the National Radio Astronomy Observatory (NRAO). The NAC program is designed to increase the number of underrepresented minorities in STEM, but what is unique about the NAC is its long-term mentoring. The NAC follows recommendations from the American Institute of Physics (AIP) TEAM-UP report addressing systemic changes to increase African Americans with Bachelor's degrees in physics and astronomy. This report states ways to foster sense of belonging, develop physics identity, show academic and personal support for mentees. Being a NAC student, I had mentors that treated me as equal. I felt a sense of belonging and self-efficacy. This experience motivated me to follow a similar mentoring style.

One of the challenges of my own mentoring involves the fact that there are several intersectional identities that I do not cover and thus could bias my mentoring relationships. For example, I am a Costa Rican who has more than ten years living in the US. I have done my academic work in the US, in spaces that are vastly different in comparison with academic spaces in Central America and the Caribbean. For this reason, I find having high emotional intelligence helpful when mentoring because acknowledging these facts can go a long way for students.

5.4 Personal limitations

The amount of work I have done to improve participation of marginalized students from Central America and Caribbean has not been remunerated. The National Radio Astronomy Observatory has done excelling work at providing a financial incentive for any work I have done related to the NAC. However, there are other institutions that take the opportunity of one's experience to exploit knowledge without remuneration. The amount of time it takes to run such organization, while also participating in other responsibilities as a

graduate student is overwhelming.

5.5 Takeaways

Contributing towards making research in astrophysics accessible to marginalized students is the most important part of being an astronomer. One cannot prioritize scientific discoveries while ignoring the humanity of the people we work with. Personally, astrophysics feeds my curiosities about how galaxies work, but just understanding the physics of galaxies does not help me fight social problems that marginalized colleagues face. My research contributions on understanding the galaxy formation, while contributing to develop access to astronomy research for the Central American-Caribbean community is what propels me to go forward. A balance of these two is how I am consciously contributing to the astronomy community.

CHAPTER 6

Conclusions

The field of galaxy formation and evolution seeks to understand how galaxies form and change over time, both in terms of their internal structures, their interactions with other galaxies, and the surrounding environment. This involves studying a range of physical processes, such as galactic angular momentum, star formation, gas accretion, mergers, and feedback from supernovae and active galactic nuclei. By observing galaxies across different wavelengths of light and modeling their properties with computer simulations, researchers aim to reconstruct the history of galaxies and trace the origins of their diverse population we observe today. The key questions we focus in this thesis are: how strong is the connection between galactic angular momentum, dark matter angular momentum, and morphology? What is the contribution of black holes to the physical origin of the scatter in stellar mass within the stellar mass-to-halo mass relation? We investigate these questions in the context of a semi-analytic model of galaxy formation.

The semi-analytic model DARK SAGE evolves galaxies in a one-dimensional disk structure. This is done by breaking down galaxy disks into 30 equally spaced logarithmic bins of specific angular momentum. Most SAMs treat galactic disks physical processes in global terms (i.e. calculating star formation rates, metallicities, feedback energy outputs within the whole disk as opposed to within local regions like an annuli), but DARK SAGE has the capabilities of looking at these properties locally within each annulus. We provide a general description of how SAMs work as well as detailed prescriptions used in DARK SAGE in chapter 2. Using DARK SAGE, we study the present-day connection between galaxy morphology and angular momentum (Chapter 3). Beyond merely extending the work of Stevens et al. (2016) to study stellar disks over the entire range of D/T, we seek to take advantage of the sophisticated treatment of angular momentum in DARK SAGE to dissect its connection to galaxy morphology in greater detail. Specifically, we explore how disk size and velocity are connected to morphology, and we investigate the connection between galaxy morphology and the angular momentum of dark matter and gas, as well. We find that not only do bulge-dominated galaxies tend to live in halos with higher dark matter specific angular momentum than disk-dominated galaxies, but intermediate galaxies (those with roughly equal fractions of bulge and disk mass) have the lowest dark matter specific angular momentum of all. Yet, when controlling for halo mass, rather than stellar mass, the relationship between dark matter specific angular momentum and morphology vanishes. To summarize, our findings suggest that in massive galaxies, the angular momentum of the disk and that of dark matter are not necessarily connected. While in DARK SAGE, the size of the disk and the halo spin appear to be linked, this is not always the case, as seen in galaxies with excess H,I (as explained in Lutz et al. 2018). Romanowsky

& Fall (2012) noted that various internal and external factors, such as mergers, outflows, galaxy stripping, and radial migration of stars, contribute to the diverse ways in which baryonic and dark matter components acquire angular momentum (as discussed in section 6.3 of their paper). Our study demonstrates that the angular momenta of the disk and dark matter vary between different types of galaxies. In DARK SAGE, the halo spin determines how gas is added to the disk during a single cooling episode, and the way in which matter is distributed in the disk is influenced by the galaxy's complete history. Based on these results, we find that halo mass—rather than angular momentum—is the main driver of the predicted morphology sequence. These results drove my interest in understanding the galaxy-halo connection.

When looking at the stellar mass-halo mass relation, DARK SAGE galaxies have significantly large scatter in stellar mass at fixed halo mass. Empirical models have not been able to fully constrain this scatter. In addition, semi-analytic models like DARK SAGE systematically predict higher stellar mass scatter at fixed halo mass than hydrodynamical simulations (Wechsler & Tinker, 2018). To further investigate the physical origin of this scatter, we explore modifications to the black hole physics in DARK SAGE (Chapter 4). Here, we investigate the physical origin of the scatter in the stellar mass–halo mass relation by exploring modifications to the physics in the SAM DARK SAGE. We find that much of the scatter arises from the treatment of AGN quenching, so our modifications focus on this area of the SAM. Within DARK SAGE, we isolate two potential contributions to the stellar mass scatter at fixed halo mass: 1) the black hole mass distribution, and 2) the treatment of AGN feedback. To explore the former, we force DARK SAGE to follow the black hole mass–halo mass median relation produced by the ILLUSTRISTNG300-1 hydrodynamical simulation using the highest-resolution box. We vary the scatter in black hole mass at a given halo mass to determine if this affects the scatter in stellar mass. To explore the latter, we run DARK SAGE with AGN quenching models that affect the various gas reservoirs in the SAM differently. Our experiments show that, turning off AGN feedback reduces the stellar mass scatter significantly. Changing the black hole seeding and AGN feedback prescription reduces the scatter in stellar mass at all halo mass bins, except at halo masses above $10^{14}\,M_{\odot}$. Taken together, these results suggest that the AGN feedback in SAMs acts in a qualitatively different way than AGN feedback implemented in cosmological simulations. This means that either or both may require substantial modification to match the empirically-determined scatter.

By using the black hole mass-halo mass analytic function, we create an imaginary situation in which DARK SAGE galaxies adhere to a black hole mass-halo mass relationship with no variation in black hole mass. However, even with this highly restrictive assumption, DARK SAGE still produces a greater scatter in stellar mass than TNG, up to three times larger in some cases, especially at the lowest halo masses (as shown in Figure 4.7). This suggests that the model's stellar mass scatter is a result of the simulation's physical processes and not solely due to the black hole mass-halo mass relation. Furthermore, not all types

of feedback have the same impact on reducing the scatter in stellar mass. When we deactivate *quasar mode* and stellar feedback, the scatter in stellar mass remains largely unaffected. This emphasizes the significance of modifying *radio mode* feedback to reduce the stellar mass scatter in SAMs. Some may argue that there are alternative methods for reducing scatter in stellar mass without modifying the AGN feedback prescription. For example, by increasing the cooling time, it may be possible to slow down the transfer of gas from the CGM reservoir to the ISM, allowing larger galaxies to quench based on current AGN feedback. Additionally, injecting angular momentum into the cold gas that is accreting can prevent it from losing sufficient angular momentum to form stars. However, simply varying the star formation efficiency may not be enough to decrease the scatter in stellar mass. The scatter is most significant around the quenching mass, indicating that AGN feedback is primarily responsible for the large scatter in stellar mass. Turning off *radio mode* feedback significantly affects the scatter in stellar mass at fixed halo mass, highlighting a general issue with how SAMs regulate feedback and distribute energy to the CGM.

Semi-analytic model predictions have shown to be a useful tool to the community when dealing with physics that is currently poorly understood. Although there is a lot of work to be done to improve SAMs, they play an important part in testing observational constraints for upcoming and future observations (Yung et al., 2022, 2023). When comparing different SAM models without calibrating to observations, we see disagreement in the predictions for the stellar mass functions, star formation rates, and stellar-to-halo mass ratios, where the scatter in those relations becomes much larger (Knebe et al., 2015). The suggestion here is that there should be a consensus as to the calibration method and what observations models should match to. Since the merger trees are essential inputs to the SAM, comparing different halo finder tools is also important. Knebe et al. (2013) found excellent agreement between a set of halo finder algorithms like SUBFIND, ROCKSTAR, and AHF when applied to a Local Group simulation. The discrepancies found were more in terms of the gas content and baryon fractions, especially in low-mass halos. Because in poorly resolved, low-mass halos, gas particles are more likely to be removed. Therefore, more resolution is required to increase the baryon fraction in these objects.

Most semi-analytic models are in reasonably good agreement with observational relations like the stellar mass function, the star formation density as a function of redshift, the black hole mass-bulge mass relation, and others. However, these relations are generally calibrated to observations which in some cases have significant variations, especially at high redshifts. Here, it becomes important to be transparent about the limitations observations used to calibrate SAMs have. Disentagling galaxy properties in a SAM is difficult given the amount of coupled prescriptions, but tracking key properties at each timestep of the simulation while would allow for a close analysis. Solving any galaxy formation problem becomes more challenging when not taking into account that there is a set of diverse SAMs and other galaxy formation models that use

different calibration methods, resolutions, and physical prescriptions.

Future work involves including modifications to seeding, accretion and feedback from supermassive black holes (SMBHs) to understand in more detail their contribution to the scatter in stellar mass at fixed halo mass within the stellar-to-halo mass relation. I will use DARK SAGE to include the impact of continual formation of intermediate mass range black holes (IMBHs) over cosmic time, their role in SMBH formation and galaxy co-evolution.

References

Abadi, M. G., Moore, B., & Bower, R. G. 1999, Monthly Notices of the Royal Astronomical Society, 308, 947

Applebaum, E., Brooks, A. M., Christensen, C. R., et al. 2021, The Astrophysical Journal, 906, 96

Avila-Reese, V., & Firmani, C. 1999, ASP Conference Series, 163

Bagla, J. S. 2005, Current Science, 88, 1088

Bahcall, N. A., & Soneira, R. M. 1983, The Astrophysical Journal, 270, 20

Baldry, I. K., Glazebrook, K., & Driver, S. P. 2008, Monthly Notices of the Royal Astronomical Society, 959, 945

Baldry, I. K., Driver, S. P., Loveday, J., et al. 2012, Monthly Notices of the Royal Astronomical Society, 421, 621

Barnes, J., & Efstathiou, G. 1987, The Astrophysical Journal, 319, 575

Barnes, J. E., & Hernquist, L. 1996, The Astrophysical Journal, 471, 115

Bastian, N., Covey, K. R., & Meyer, M. R. 2010, Annual Review of Astronomy and Astrophysics, 48, 339

Baugh, C. 2006, Reports on Progress in Physcis, 69, doi:10.1088/0034-4885/69/12/R02

Becker, M. R. 2015, arXiv e-prints, arXiv:1507.03605

Behroozi, P., Wechsler, R. H., Hearin, A. P., & Conroy, C. 2019, Monthly Notices of the Royal Astronomical Society, 488, 3143

Behroozi, P., Knebe, A., Pearce, F. R., et al. 2015, Monthly Notices of the Royal Astronomical Society, 454, 3020

Behroozi, P. S., Conroy, C., & Wechsler, R. H. 2010, The Astrophysical Journal, 717, 379

Behroozi, P. S., Wechsler, R. H., & Conroy, C. 2013a, The Astrophysical Journal, Letters, 762, L31

Behroozi, P. S., Wechsler, R. H., & Wu, H.-Y. 2013b, The Astrophysical Journal, 762, 109

Bekki, K. 1998, The Astrophysical Journal, 502, L133

Bell, E. F., Wolf, C., Meisenheimer, K., et al. 2004, The Astrophysical Journal, 608, 752

Benson, A. 2010, New Astronomy, 17, doi:10.1016/j.newast.2011.07.004

Benson, A. J. 2010, Physics Reports, 495, 33

—. 2012, , 17, 175

Bernardi, G. 2016, The Unforgotten sisters female astronomers and scientists before Caroline Herschel (Springer International Publishing)

Bernardi, M., Meert, A., Sheth, R. K., et al. 2013, Monthly Notices of the Royal Astronomical Society, 436, 697

Bernyk, M., Croton, D. J., Tonini, C., et al. 2016, The Astrophysical Journal, 223, 15

Bertschinger, E. 1989, The Astrophysical Journal, 340, 666

Bertschinger, E. 1998, Annual Review of Astronomy and Astrophysics, 36, 599

Binney, J., & Tremaine, S. 2008, Galactic Dynamics: Second Edition

Blanton, M. R., & Moustakas, J. 2009, Annual Review of Astronomy and Astrophysics, 47, 159

Blanton, M. R., Hogg, D. W., Bahcall, N. A., et al. 2003, The Astrophysical Journal, 592, 819

Bluck, A. F., Trevor Mendel, J., Ellison, S. L., et al. 2014, Monthly Notices of the Royal Astronomical Society, 441, 599

Blumenthal, G. R., Faber, S. M., Primack, J. R., & Rees, M. J. 1984, Nature, 311, 517

Bonato, M., Liuzzo, E., Herranz, D., et al. 2019, Monthly Notices of the Royal Astronomical Society, 485, 1188

Bond, P. 2001, Astronomy and Geophysics, 42, 4.24

Bondi, H. 1952, Monthly Notices of the Royal Astronomical Society, 112, 195

Bondi, H., & Gold, T. 1948, Monthly Notices of the Royal Astronomical Society, 108, 252

Bose, S., Eisenstein, D. J., Hernquist, L., et al. 2019, Monthly Notices of the Royal Astronomical Society, 490, 5693

Bower, R. G., Benson, A. J., Malbon, R., et al. 2006, Monthly Notices of the Royal Astronomical Society, 370, 645

Bower, R. G., Vernon, I., Goldstein, M., et al. 2010, Monthly Notices of the Royal Astronomical Society, 407, 2017

Boylan-Kolchin, M., Ma, C.-P., & Quataert, E. 2008, Monthly Notices of the Royal Astronomical Society, 383, 93

Brown, T., Catinella, B., Cortese, L., et al. 2015, Monthly Notices of the Royal Astronomical Society, 452, 2479

Bruzual, G., & Charlot, S. 2003, Monthly Notices of the Royal Astronomical Society, 344, 1000

Bullock, J. S., & Boylan-Kolchin, M. 2017, Annual Review of Astronomy and Astrophysics, 55, 343

Bullock, J. S., Dekel, A., Kolatt, T. S., et al. 2001, The Astrophysical Journal, 555, 240

Bullock, J. S., Kravtsov, A. V., & Weinberg, D. H. 2000, The Astrophysical Journal, 539, 517

Butler, K. M., Obreschkow, D., & Oh, S.-H. 2017, The Astrophysical Journal, 834, L4

Calzetti, D. 2001, The Publications of the Astronomical Society of the Pacific, 113, 1449

Catinella, B., Schiminovich, D., Kauffmann, G., et al. 2010, Monthly Notices of the Royal Astronomical Society, 403, 683

Cen, R., & Ostriker, J. P. 1994, The Astrophysical Journal, 429, 4

—. 1999a, The Astrophysical Journal, 517, 31

—. 1999b, The Astrophysical Journal, 519, 109

Chabrier, G. 2003, The Publications of the Astronomical Society of the Pacific, 115, 763

Choi, S. K., Hasselfield, M., Ho, S.-P. P., et al. 2020, Journal of Cosmology and Astroparticle Physics, 2020, 045

Clowe, D., Bradač, M., Gonzalez, A. H., et al. 2006, The Astrophysical Journal, Letters, 648, L109

Cole, S., Aragón-Salamanca, A., Frenk, C. S., & Zepf, S. E. 1994, Monthly Notices of the Royal Astronomical Society, 271, 781

Cole, S., & Lacey, C. 1996, Monthly Notices of the Royal Astronomical Society, 281, 716

Cole, S., Lacey, C. G., Baugh, C. M., & Frenk, C. S. 2000, Monthly Notices of the Royal Astronomical Society, 319, 168

Colín, P., Klypin, A. A., Kravtsov, A. V., & Khokhlov, A. M. 1999, The Astrophysical Journal, 523, 32

Conroy, C. 2013, Annual Review of Astronomy and Astrophysics, 51, 393

Conroy, C., & Gunn, J. E. 2010, The Astrophysical Journal, 712, 833

Conroy, C., Gunn, J. E., & White, M. 2009, The Astrophysical Journal, 699, 486

Conroy, C., & van Dokkum, P. G. 2012, The Astrophysical Journal, 760, 71

Conroy, C., Prada, F., Newman, J. A., et al. 2007, The Astrophysical Journal, 654, 153

Cook, R. H., Cortese, L., Catinella, B., & Robotham, A. 2019, Monthly Notices of the Royal Astronomical Society, 490, 4060

Coupon, J., Arnouts, S., van Waerbeke, L., et al. 2015, Monthly Notices of the Royal Astronomical Society, 449, 1352

Cox, T. J., Dutta, S. N., Di Matteo, T., et al. 2006, The Astrophysical Journal, 650, 791

Croton, D. J., Springel, V., White, S. D., et al. 2006, Monthly Notices of the Royal Astronomical Society, 365, 11

Croton, D. J., Stevens, A. R. H., Tonini, C., et al. 2016, The Astrophysical Journal Supplement Series, 222, 22

Davis, A. J. 2011, PhD thesis, Yale University

Davis, M., Efstathiou, G., Frenk, C. S., & White, S. D. M. 1985, The Astrophysical Journal, 292, 371

De Lucia, G., Fontanot, F., Wilman, D., & Monaco, P. 2011, Monthly Notices of the Royal Astronomical Society, 414, 1439

de Pineda Carias, M. C. 2004, The Astronomical Observatory of Honduras: A Project of International Cooperation, ed. W. Wamsteker, R. Albrecht, & H. J. Haubold (Dordrecht: Springer Netherlands), 101–111

de Vaucouleurs, G. 1953, Monthly Notices of the Royal Astronomical Society, 113, 134

Dekel, A., & Burkert, A. 2014, Monthly Notices of the Royal Astronomical Society, 438, 1870

Dey, A., Soifer, B. T., Desai, V., et al. 2008, The Astrophysical Journal, 677, 943

Di Matteo, T., Springel, V., & Hernquist, L. 2005, Nature, 433, 604

Donovan, J. L., Serra, P., Van Gorkom, J. H., et al. 2009, The Astronomical Journal, 137, 5037

Driver, S. P., Allen, P. D., Graham, A. W., et al. 2006, Monthly Notices of the Royal Astronomical Society, 368, 414

D'Souza, R., Vegetti, S., & Kauffmann, G. 2015, Monthly Notices of the Royal Astronomical Society, 454, 4027

Edgar, R. 2004, New Astronomy Reviews, 48, 843

Efstathiou, G., Davis, M., White, S. D. M., & Frenk, C. S. 1985, The Astrophysical Journal Supplement Series, 57, 241

Efstathiou, G., Lake, G., & Negroponte, J. 1982, Monthly Notices of the Royal Astronomical Society, 199, 1069

El-Badry, K., Quataert, E., Wetzel, A., et al. 2018, Monthly Notices of the Royal Astronomical Society, 473, 1930

El Eid, M. F., Fricke, K. J., & Ober, W. W. 1983, Astronomy and Astrophysics, 119, 54

Faber, S. M., Willmer, C. N. A., Wolf, C., et al. 2007, The Astrophysical Journal, 665, 265

Fabian, A. C., Sanders, J. S., Allen, S. W., et al. 2003, Monthly Notices of the Royal Astronomical Society, 344, L43

Fall, S. M. 1983, International Astronomical Union, 391

Fall, S. M., & Efstathiou, G. 1980, Monthly Notices of the Royal Astronomical Society, 193, 189

Fall, S. M., & Romanowsky, A. J. 2013, The Astrophysical Journal, Letters, 769, 26

—. 2018, The Astrophysical Journal, 868, 133

Ferland, G. J., Porter, R. L., van Hoof, P. A. M., et al. 2013, Revista Mexicana de Astronomia y Astrofisica, 49, 137

Field, G. B., & Shepley, L. C. 1968, Astrophysics and Space Science, 1, 309

Fontanot, F., Somerville, R. S., Silva, L., Monaco, P., & Skibba, R. 2009, Monthly Notices of the Royal Astronomical Society, 392, 553

Forbes, J. C., Krumholz, M. R., & Speagle, J. S. 2019, Monthly Notices of the Royal Astronomical Society, 487, 3581

Fu, J., Guo, Q., Kauffmann, G., & Krumholz, M. R. 2010, Monthly Notices of the Royal Astronomical Society, 409, 515

Fu, J., Kauffmann, G., Huang, M.-L., et al. 2013, Monthly Notices of the Royal Astronomical Society, 434, 1531

Garrison-Kimmel, S., Bullock, J. S., Boylan-Kolchin, M., & Bardwell, E. 2017, Monthly Notices of the Royal Astronomical Society, 464, 3108

Genel, S., Fall, S. M., Hernquist, L., et al. 2015, The Astrophysical Journal, Letters, 804, 1

Genel, S., Genzel, R., Bouché, N., Naab, T., & Sternberg, A. 2009, The Astrophysical Journal, 701, 2002

Genel, S., Vogelsberger, M., Springel, V., et al. 2014, Monthly Notices of the Royal Astronomical Society, 445, 175

Gilmore, R., Somerville, R., Primack, J., & Domínguez, A. 2012, Monthly Notices of the Royal Astronomical Society, 422, 3189

Giovanelli, R., Haynes, M. P., Kent, B. R., et al. 2005, The Astronomical Journal, 130, 2598

Granato, G. L., De Zotti, G., Silva, L., Bressan, A., & Danese, L. 2004, The Astrophysical Journal, 600, 580

Grande, J., Solà, J., & Štefani, H. 2008, Journal of Cosmology and Astroparticle Physics, 1475

Grogin, N. A., Kocevski, D. D., Faber, S. M., et al. 2011, The Astrophysical Journal Supplement Series, 197, doi:10.1088/0067-0049/197/2/35

Guo, Q., White, S., Boylan-Kolchin, M., et al. 2011, Monthly Notices of the Royal Astronomical Society, 413, 101

Hagen, L. M. Z., Seibert, M., Hagen, A., et al. 2016, The Astrophysical Journal, 826, 210

Harrison, E. R. 1971, Monthly Notices of the Royal Astronomical Society, 154, 167

Hatton, S., Devriendt, J. E., Ninin, S., et al. 2003, Monthly Notices of the Royal Astronomical Society, 343, 75

Hearin, A. P., & Watson, D. F. 2013, Monthly Notices of the Royal Astronomical Society, 435, 1313

Henriques, B. M., White, S. D., Thomas, P. A., et al. 2013, Monthly Notices of the Royal Astronomical Society, 431, 3373

Henriques, B. M. B., White, S. D. M., Thomas, P. A., et al. 2015, Monthly Notices of the Royal Astronomical Society, 451, 2663

Henriques, B. M. B., Yates, R. M., Fu, J., et al. 2020, Monthly Notices of the Royal Astronomical Society, 491, 5795

Heyl, J. S., Hernquist, L., & Spergel, D. N. 1994, The Astrophysical Journal, 427, 165

Hopkins, P. F., Hernquist, L., Cox, T. J., et al. 2006, The Astrophysical Journal Supplement Series, 163, 1

Hopkins, P. F., Hernquist, L., Cox, T. J., Keres, D., & Wuyts, S. 2009a, The Astrophysical Journal, 691, 1424

Hopkins, P. F., Quataert, E., & Murray, N. 2012, Monthly Notices of the Royal Astronomical Society, 421, 3522

Hopkins, P. F., Somerville, R. S., Cox, T. J., et al. 2009b, Monthly Notices of the Royal Astronomical Society, 397, 802

Hoyle, F. 1949, Monthly Notices of the Royal Astronomical Society, 109, 365

Hudson, M. J., Gillis, B. R., Coupon, J., et al. 2015, Monthly Notices of the Royal Astronomical Society, 447, 298

Hunter, J. D. 2007, Computing In Science and Engineering, 9

Irodotou, D., Thomas, P. A., Henriques, B. M., Sargent, M. T., & Hislop, J. M. 2019, Monthly Notices of the Royal Astronomical Society, 489, 3609

Jarquin-Solis, M. E., Lin-Shiao, E., Guerra, M., et al. 2022, Frontiers in Research Metrics and Analytics, 7, 904029

Jones, E., Oliphant, T., Peterson, P., & Others. 2001, SciPy: Open source scientific tools for Python, Tech. rep.

Joshi, G. D., Pillepich, A., Nelson, D., et al. 2020, Monthly Notices of the Royal Astronomical Society, 496, 2673

Kauffmann, G., Colberg, J. M., Diaferio, A., & White, S. D. 1999, Monthly Notices of the Royal Astronomical Society, 303, 188

Kauffmann, G., & Haehnelt, M. 2000, Monthly Notices of the Royal Astronomical Society, 311, 576

Kauffmann, G., White, S. D. M., & Guiderdoni, B. 1993, Monthly Notices of the Royal Astronomical Society, 264, 201

Kauffmann, G., Heckman, T. M., White, S. D. M., et al. 2003, Monthly Notices of the Royal Astronomical Society, 341, 33

Kennicutt, Robert C., J. 1998, Annual Review of Astronomy and Astrophysics, 36, 189

Keres, D., Yun, M. S., & Young, J. S. 2003, The Astrophysical Journal, 582, 659

Khandai, N., Di Matteo, T., Croft, R., et al. 2015, Monthly Notices of the Royal Astronomical Society, 450, 1349

Kharb, P., O'Dea, C. P., Baum, S. A., et al. 2014, Monthly Notices of the Royal Astronomical Society, 440, 2976

Kim, C., Woo, J.-H., Jadhav, Y., et al. 2022, The Astrophysical Journal, 928, 73

Kimm, T., Devriendt, J., Slyz, A., et al. 2011, Monthly Notices of the Royal Astronomical Society

Kimura, S. S., Murase, K., & Mészáros, P. 2021, Nature Communications, 12, 5615

Klapp, J. 1983, Astrophysics and Space Science, 93, 313

Klypin, A., Gottlöber, S., Kravtsov, A. V., & Khokhlov, A. M. 1999, The Astrophysical Journal, 516, 530

Klypin, A. A., & Kopylov, A. I. 1983, Soviet Astronomy Letters, 9, 41

Knebe, A., & Power, C. 2008, The Astrophysical Journal, 678, 621

Knebe, A., Knollmann, S. R., Muldrew, S. I., et al. 2011, Monthly Notices of the Royal Astronomical Society, 415, 2293

Knebe, A., Libeskind, N. I., Pearce, F., et al. 2013, Monthly Notices of the Royal Astronomical Society, 428, 2039

Knebe, A., Pearce, F. R., Thomas, P. A., et al. 2015, Monthly Notices of the Royal Astronomical Society, 451, 4029

Knollmann, S. R., & Knebe, A. 2009, The Astrophysical Journal Supplement Series, 182, 608

Kormendy, J. 1993, in International Astronomical Union, 209

Kravtsov, A. V., Berlind, A. A., Wechsler, R. H., et al. 2004, The Astrophysical Journal, 609, 35

Kravtsov, A. V., Klypin, A. A., & Khokhlov, A. M. 1997, The Astrophysical Journal Supplement Series, 111, 73

Kravtsov, A. V., Vikhlinin, A. A., & Meshcheryakov, A. V. 2018, The Astronomical Journal, 44, 8

Kroupa, P. 2001, Monthly Notices of the Royal Astronomical Society, 322, 231

Lagos, C. d. P., Theuns, T., Stevens, A. R. H., et al. 2017, Monthly Notices of the Royal Astronomical Society, 464, 3850

Lagos, C. d. P., Tobar, R. J., Robotham, A. S. G., et al. 2018, Monthly Notices of the Royal Astronomical Society, 481, 3573

Lagos, C. d. P., Stevens, A. R. H., Bower, R. G., et al. 2018, Monthly Notices of the Royal Astronomical Society, 473, 4956

Leauthaud, A., Tinker, J., Bundy, K., et al. 2012, The Astrophysical Journal, 744, 159

Levato, H. 2007, IAU Special Session, 5, 27

Lilly, S. J., Le Fevre, O., Hammer, F., & Crampton, D. 1996, The Astrophysical Journal, Letters, 460, L1

Lotz, J. M., Jonsson, P., Cox, T. J., & Primack, J. R. 2010, Monthly Notices of the Royal Astronomical Society, 404, 590

Lower, S., Narayanan, D., Leja, J., et al. 2020, The Astrophysical Journal, 904, 33

Lu, Y., Wechsler, R. H., Somerville, R. S., et al. 2014, The Astrophysical Journal, 795, 123

Lutz, K. A., Kilborn, V. A., Koribalski, B. S., et al. 2018, Monthly Notices of the Royal Astronomical Society, 476, 3744

Macciò, A. V., Dutton, A. A., Van Den Bosch, F. C., et al. 2007, Monthly Notices of the Royal Astronomical Society, 378, 55

Madau, P., & Dickinson, M. 2014, Annual Review of Astronomy and Astrophysics, 52, 415

Maity, D., & Saha, P. 2018, Physical Review D: Particles, Fields, Gravitation and Cosmology, 98, 103525

Man, Z.-Y., Peng, Y.-J., Shi, J.-J., et al. 2019, The Astrophysical Journal, 881, 74

Mandelbaum, R., Seljak, U., Kauffmann, G., Hirata, C. M., & Brinkmann, J. 2006, Monthly Notices of the Royal Astronomical Society, 368, 715

Maraston, C. 2005, Monthly Notices of the Royal Astronomical Society, 362, 799

Marinacci, F., Vogelsberger, M., Pakmor, R., et al. 2018, Monthly Notices of the Royal Astronomical Society, 480, 5113

Marshall, M. A., Mutch, S. J., Qin, Y., Poole, G. B., & Wyithe, J. S. B. 2019, Monthly Notices of the Royal Astronomical Society, 488, 1941

Martin, C. L. 1999, The Astrophysical Journal, 513, 156

Martin, D. C., Fanson, J., Schiminovich, D., et al. 2005, The Astrophysical Journal, Letters, 619, L1

Martizzi, D., Vogelsberger, M., Torrey, P., et al. 2020, Monthly Notices of the Royal Astronomical Society, 491, 5747

Matteucci, F., & Brocato, E. 1990, The Astrophysical Journal, 365, 539

Matthee, J., & Schaye, J. 2019, Monthly Notices of the Royal Astronomical Society, 484, 915

McAlpine, S., Helly, J. C., Schaller, M., et al. 2016, Astronomy and Computing, 15, 72

Mitchell, P. D., Lacey, C. G., Lagos, C. D., et al. 2018, Monthly Notices of the Royal Astronomical Society, 474, 492

Mo, H. J., Mao, S., & White, S. D. M. 1998, Monthly Notices of the Royal Astronomical Society, 295, 319

Mo, H. J., & White, S. D. M. 1996, Monthly Notices of the Royal Astronomical Society, 282, 347

Moffett, A. J., Kannappan, S. J., Berlind, A. A., et al. 2015, The Astrophysical Journal, 812, 89

Moffett, A. J., Ingarfield, S. A., Driver, S. P., et al. 2016, Monthly Notices of the Royal Astronomical Society, 457, 1308

Montero-Camacho, P., & Castillo-Fallas, J. C. 2021, The Status of Astronomy in Central America and the Caribbean

Moore, B. 1994, Nature, 370, 629

Moore, B., Governato, F., Quinn, T., Stadel, J., & Lake, G. 1998, The Astrophysical Journal, 499, 5

Moore, B., Katz, N., & Lake, G. 1996a, The Astrophysical Journal, 457, 455

Moore, B., Katz, N., Lake, G., Dressler, A., & Oemler, A. 1996b, Nature, 379, 613

More, S., Kravtsov, A. V., Dalal, N., & Gottlöber, S. 2011a, The Astrophysical Journal Supplement Series, 195, 4

More, S., van den Bosch, F. C., Cacciato, M., et al. 2011b, Monthly Notices of the Royal Astronomical Society, 410, 210

Moreno, J., Torrey, P., Ellison, S. L., et al. 2015, Monthly Notices of the Royal Astronomical Society, 448, 1107

Moster, B. P., Naab, T., & White, S. D. M. 2013, Monthly Notices of the Royal Astronomical Society, 428, 3121

Munshi, F., Brooks, A. M., Applebaum, E., et al. 2021, The Astrophysical Journal, 923, 35

Munshi, F., Brooks, A. M., Christensen, C., et al. 2019, The Astrophysical Journal, 874, 40

Naiman, J. P., Pillepich, A., Springel, V., et al. 2018, Monthly Notices of the Royal Astronomical Society, 477, 1206

Navarro, J. F., & Benz, W. 1991, The Astrophysical Journal, 380, 320

Navarro, J. F., Frenk, C. S., & White, S. D. 1997, The Astrophysical Journal, 490, 493

Navarro, J. F., Frenk, C. S., & White, S. D. M. 1996, The Astrophysical Journal, 462, 563

Nelson, D., Pillepich, A., Genel, S., et al. 2015, Astronomy and Computing, 13, 12

Nelson, D., Pillepich, A., Springel, V., et al. 2018, Monthly Notices of the Royal Astronomical Society, 475, 624

Nelson, D., Pillepich, A., Springel, V., et al. 2019a, Monthly Notices of the Royal Astronomical Society, 490, 3234

Nelson, D., Springel, V., Pillepich, A., et al. 2019b, Computational Astrophysics and Cosmology, 6, 2

Noguchi, M. 1999, The Astrophysical Journal, 514, 77

Ntampaka, M., ZuHone, J., Eisenstein, D., et al. 2019, The Astrophysical Journal, 876, 82

Obreja, A., Dutton, A. A., Macciò, A. V., et al. 2019, Monthly Notices of the Royal Astronomical Society, 487, 4424

Obreschkow, D., & Glazebrook, K. 2014, The Astrophysical Journal, 784, 26

Oosterloo, T. A., Morganti, R., Sadler, E. M., Van Der Hulst, T., & Serra, P. 2007, Astronomy and Astrophysics, 465, 787

Orienti, M., Migliori, G., Brunetti, G., et al. 2020, Monthly Notices of the Royal Astronomical Society, 494, 2244

Padovani, P. 2017, Frontiers in Astronomy and Space Sciences, 4, doi:10.3389/fspas.2017.00035

Pandya, V., Somerville, R. S., Anglés-Alcázar, D., et al. 2020, The Astrophysical Journal, 905, 4

Parry, O. H., Eke, V. R., & Frenk, C. S. 2009, Monthly Notices of the Royal Astronomical Society, 396, 1972

Pascucci, I., Apai, D., Luhman, K., et al. 2009, The Astrophysical Journal, 696, 143

Peebles, P. J. E. 1969, The Astrophysical Journal, 155, 393

Peebles, P. J. E. 1980, The large-scale structure of the universe

Peebles, P. J. E., Schramm, D. N., Turner, E. L., & Kron, R. G. 1991, Nature, 352, 769

Penner, K., Dickinson, M., Pope, A., et al. 2012, The Astrophysical Journal, 759, 28

Penzias, A. A., & Wilson, R. W. 1965, The Astrophysical Journal, 142, 419

Pérez, F., & Granger, B. E. 2007, IEEE Journals & Magazines, 9, 21

Perez, L. A., Genel, S., Villaescusa-Navarro, F., et al. 2022, arXiv e-prints, arXiv:2204.02408

Pichon, C., Pogosyan, D., Kimm, T., et al. 2011, Monthly Notices of the Royal Astronomical Society, 418, 2493

Pillepich, A., Nelson, D., Hernquist, L., et al. 2018, Monthly Notices of the Royal Astronomical Society, 475, 648

Pillepich, A., Springel, V., Nelson, D., et al. 2018, Monthly Notices of the Royal Astronomical Society, 473, 4077

Pope, A., Bussmann, R. S., Dey, A., et al. 2008, The Astrophysical Journal, 689, 127

Porras-Valverde, A. J., Holley-Bockelmann, K., Berlind, A. A., & Stevens, A. R. H. 2021, The Astrophysical Journal, 923, 273

Posti, L., Fraternali, F., DI Teodoro, E. M., & Pezzulli, G. 2018, Astronomy and Astrophysics, 612, 6

Read, J. I., Wilkinson, M. I., Evans, N. W., Gilmore, G., & Kleyna, J. T. 2006, Monthly Notices of the Royal Astronomical Society, 366, 429

Reddy, N., Dickinson, M., Elbaz, D., et al. 2012, The Astrophysical Journal, 744, 154

Ricciardelli, E., & Franceschini, A. 2010, Astronomy and Astrophysics, 518, A14

Rich, R. M. 1996, in International Astronomical Union, 402

Roberts, Morton S., M. P. H. 1994, Annual Review of Astronomy and Astrophysics, 32, 115

Robitaille, T. P., Tollerud, E. J., Greenfield, P., et al. 2013, Astronomy and Astrophysics, 558, 33

Robotham, A. S. G., Bellstedt, S., Lagos, C. d. P., et al. 2020, Monthly Notices of the Royal Astronomical Society, 495, 905

Rodriguez-Gomez, V., Sales, L. V., Genel, S., et al. 2017, Monthly Notices of the Royal Astronomical Society, 467, 3083

Romanowsky, A. J., & Fall, S. M. 2012, The Astrophysical Journal Supplement Series, 203, 17

Rubin, V. C., Ford, W. K., J., & Thonnard, N. 1978, The Astrophysical Journal, Letters, 225, L107

Rubin, V. C., & Ford, W. Kent, J. 1970, The Astrophysical Journal, 159, 379

Ruiz, A. N., Cora, S. A., Padilla, N. D., et al. 2015, The Astrophysical Journal, 801, 139

Safarzadeh, M., Lu, Y., & Hayward, C. C. 2017, Monthly Notices of the Royal Astronomical Society, 472, 2462

Sales, L. V., Navarro, J. F., Peñafiel, L., et al. 2020, Monthly Notices of the Royal Astronomical Society, 494, 1848

Sales, L. V., Navarro, J. F., Schaye, J., et al. 2010, Monthly Notices of the Royal Astronomical Society, 409, 1541

Sales, L. V., Navarro, J. F., Theuns, T., et al. 2012, Monthly Notices of the Royal Astronomical Society, 423, 1544

Salim, S., Rich, R. M., Charlot, S., et al. 2007, The Astrophysical Journal Supplement Series, 173, 267

Salpeter, E. E. 1955, The Astrophysical Journal, 121, 161

Savage, B. D., & Sembach, K. R. 1996, Annual Review of Astronomy and Astrophysics, 34, 279

Schawinski, K., Urry, C. M., Simmons, B. D., et al. 2014, Monthly Notices of the Royal Astronomical Society, 440, 889

Schmidt, M. 1959, The Astrophysical Journal, 129, 243

Schombert, J., McGaugh, S., & Lelli, F. 2020, The Astronomical Journal, 160, 71

Scott, N., Graham, A. W., & Schombert, J. 2013, The Astrophysical Journal, 768, 76

Searle, L., Sargent, W. L. W., & Bagnuolo, W. G. 1973, The Astrophysical Journal, 179, 427

Serna, A., Domínguez-Tenreiro, R., & Sáiz, A. 2003, The Astrophysical Journal, 597, 878

Sharma, S., & Steinmetz, M. 2005, The Astrophysical Journal, 628, 21

Sijacki, D., Springel, V., Di Matteo, T., & Hernquist, L. 2007, Monthly Notices of the Royal Astronomical Society, 380, 877

Sijacki, D., Vogelsberger, M., Genel, S., et al. 2015, Monthly Notices of the Royal Astronomical Society, 452, 575

Sokołowska, A., Capelo, P. R., Fall, S. M., et al. 2017, The Astrophysical Journal, 835, 289

Somerville, R. S., & Davé, R. 2015, Annual Review of Astronomy and Astrophysics, 53, 51

Somerville, R. S., Gilmore, R. C., Primack, J. R., & Domínguez, A. 2012, Monthly Notices of the Royal Astronomical Society, 423, 1992

Somerville, R. S., Hopkins, P. F., Cox, T. J., Robertson, B. E., & Hernquist, L. 2008, Monthly Notices of the Royal Astronomical Society, 391, 481

Somerville, R. S., Primack, J. R., & Faber, S. M. 2001, Monthly Notices of the Royal Astronomical Society, 320, 504

Sparre, M., & Springel, V. 2016, Monthly Notices of the Royal Astronomical Society, 462, 2418

Spergel, D. N., Verde, L., Peiris, H. V., et al. 2003, The Astrophysical Journal Supplement Series, 148, 175

Springel, V. 2005, Monthly Notices of the Royal Astronomical Society, 364, 1105

Springel, V., & Hernquist, L. 2003, Monthly Notices of the Royal Astronomical Society, 339, 289

Springel, V., White, S. D., Tormen, G., & Kauffmann, G. 2001, Monthly Notices of the Royal Astronomical Society, 328, 726

Springel, V., White, S. D., Jenkins, A., et al. 2005, Nature, 435, 629

Springel, V., Pakmor, R., Pillepich, A., et al. 2018, Monthly Notices of the Royal Astronomical Society, 475, 676

Stark, D. V., Mcgaugh, S. S., & Swaters, R. A. 2009, The Astronomical Journal, 138, 392

Starkenburg, E., Helmi, A., De Lucia, G., et al. 2013, Monthly Notices of the Royal Astronomical Society, 429, 725

Steinmetz, M., & Navarro, J. F. 1999, The Astrophysical Journal, 513, 555

Stevens, A. R. H. 2016, PhD thesis, Swinburne University of Technology

Stevens, A. R. H., & Brown, T. 2017, Monthly Notices of the Royal Astronomical Society, 471, 447

Stevens, A. R. H., Croton, D. J., & Mutch, S. J. 2016, Monthly Notices of the Royal Astronomical Society, 461, 859

Stevens, A. R. H., Diemer, B., Del Lagos, C. P., et al. 2019, Monthly Notices of the Royal Astronomical Society, 490, 96

Stevens, A. R. H., Lagos, C. D. P., Contreras, S., et al. 2017, Monthly Notices of the Royal Astronomical Society, 467, 2066

Stevens, A. R. H., Lagos, C. D. P., Obreschkow, D., & Sinha, M. 2018, Monthly Notices of the Royal Astronomical Society, 481, 5543

Stewart, K. R., Kaufmann, T., Bullock, J. S., et al. 2011, The Astrophysical Journal, Letters, 735, 1

Stoehr, F., White, S. D. M., Tormen, G., & Springel, V. 2002, Monthly Notices of the Royal Astronomical Society, 335, L84

Struve, C., Oosterloo, T., Sancisi, R., Morganti, R., & Emonts, B. H. 2010, Astronomy and Astrophysics, 523, 75

Sweet, S. M., Fisher, D., Glazebrook, K., et al. 2018, The Astrophysical Journal, 860, 37

Teklu, A. F., Remus, R. S., Dolag, K., et al. 2015, The Astrophysical Journal, 812, 29

Terrazas, B. A., Bell, E. F., Pillepich, A., et al. 2020, Monthly Notices of the Royal Astronomical Society, 493, 1888

Tinker, J. L., Brownstein, J. R., Guo, H., et al. 2017, The Astrophysical Journal, 839, 121

Tonini, C., Mutch, S. J., Croton, D. J., & Wyithe, J. S. 2016, Monthly Notices of the Royal Astronomical Society, 459, 4109

Toomre, A. 1963, The Astrophysical Journal, 139, 1217

Toomre, A. 1977, in Evolution of Galaxies and Stellar Populations, ed. B. M. Tinsley & D. C. Larson, Richard B. Gehret, 401

Tremonti, C. A., Heckman, T. M., Kauffmann, G., et al. 2004a, The Astrophysical Journal, 613, 898

—. 2004b, The Astrophysical Journal, 613, 898

Van Der Walt, S., Colbert, S. C., & Varoquaux, G. 2011, Computing in Science and Engineering, 13, 22

Vogelsberger, M., Genel, S., Springel, V., et al. 2014a, Monthly Notices of the Royal Astronomical Society, 444, 1518

—. 2014b, Nature, 509, 177

Vollmer, B., Cayatte, V., Balkowski, C., & Duschl, W. J. 2001, The Astrophysical Journal, 561, 708

Wang, L., Obreschkow, D., Lagos, C. D. P., et al. 2019, Monthly Notices of the Royal Astronomical Society, 482, 5477

Wechsler, R. H., & Tinker, J. L. 2018, Annual Review of Astronomy and Astrophysics, 56, 435

Weinberger, R., Springel, V., Hernquist, L., et al. 2017, Monthly Notices of the Royal Astronomical Society, 465, 3291

Weinberger, R., Springel, V., Pakmor, R., et al. 2018, Monthly Notices of the Royal Astronomical Society, 479, 4056

Weinzirl, T., Jogee, S., Khochfar, S., Burkert, A., & Kormendy, J. 2009, The Astrophysical Journal, 696, 411

White, S. D. M., & Frenk, C. S. 1991, The Astrophysical Journal, 379, 52

White, S. D. M., & Rees, M. J. 1978, Monthly Notices of the Royal Astronomical Society, 183, 341

Wild, V., Almaini, O., Dunlop, J., et al. 2016, Monthly Notices of the Royal Astronomical Society, 463, 832

Woosley, S. E., & Weaver, T. A. 1995, The Astrophysical Journal Supplement Series, 101, 181

Yang, X., Mo, H. J., & van den Bosch, F. C. 2003, Monthly Notices of the Royal Astronomical Society, 339, 1057

Yıldız, U. A. 2013, PhD thesis, Leiden Observatory

York, D. G., Adelman, J., Anderson, John E., J., et al. 2000, The Astronomical Journal, 120, 1579

Yung, L. Y. A., Somerville, R. S., Ferguson, H. C., et al. 2022, Monthly Notices of the Royal Astronomical Society, 515, 5416

Yung, L. Y. A., Somerville, R. S., Finkelstein, S. L., et al. 2023, Monthly Notices of the Royal Astronomical Society, 519, 1578

Zanisi, L., Shankar, F., Lapi, A., et al. 2020, Monthly Notices of the Royal Astronomical Society, 492, 1671

Zavala, J., Trayford, J. W., Furlong, M., et al. 2016, Monthly Notices of the Royal Astronomical Society, 460, 4466

Zentner, A. R., & Bullock, J. S. 2003, The Astrophysical Journal, 598, 49

Zjupa, J., & Springel, V. 2017, Monthly Notices of the Royal Astronomical Society, 466, 1625

Zoldan, A., De Lucia, G., Xie, L., Fontanot, F., & Hirschmann, M. 2018, Monthly Notices of the Royal Astronomical Society, 481, 1376

—. 2019, Monthly Notices of the Royal Astronomical Society, 487, 5649

Zu, Y., & Mandelbaum, R. 2015, Monthly Notices of the Royal Astronomical Society, 454, 1161

Zucker, D. B., Kniazev, A. Y., Bell, E. F., et al. 2004, The Astrophysical Journal, 2002

Zwaan, M. A., Meyer, M. J., Staveley-Smith, L., & Webster, R. L. 2005, Monthly Notices of the Royal Astronomical Society, 359, L30